2013-3

Development of Novel Fiber Optic Humidity Sensors and Their Derived Applications

Jinesh Mathew
Technological University Dublin, mathew.jinesh@tudublin.ie

Development of Novel Fiber Optic Humidity Sensors and Their Derived Applications

A Thesis presented for the Degree of

Doctor of Philosophy

by

JINESH MATHEW, *MSc, MPhil.*

Supervisors: Prof. Gerald Farrell and Dr. Yuliya Semenova

School of Electronic and Communications Engineering

College of Engineering & Built Environment

Dublin Institute of Technology

Dublin, Ireland

March 2013

To my beloved parents and siblings,

teachers and friends

ABSTRACT

The main focus of this thesis is on the design and development of novel fiber optic devices for relative humidity (RH) sensing with emphasis on high sensitivity, a wide humidity range, low temperature dependence, fast response time and good stability.

Novel RH sensors based on fiber bends are fabricated by coating the surface of the buffer stripped bent fiber with selected hygroscopic materials such as Polyethylene oxide or Agarose. It is shown that the Polyethylene oxide coated device has a high sensitivity in a narrow RH range while the Agarose coated fiber bend shows a linear RH sensitivity in a wide RH range. Both of these sensors demonstrate a fast response (in the order of milliseconds) to RH variations. The limitations of fiber bend based humidity sensors are also discussed in the thesis.

A novel RH sensor based on a reflection type photonic crystal fiber interferometer (PCFI) is presented which does not rely on the use of any hygroscopic material. The operating principle of a PCFI sensor based on the adsorption and desorption of water vapour at the silica-air interface within the PCF capillaries is discussed. The demonstrated sensor shows a good RH sensitivity in the higher RH range. Furthermore this RH sensor is almost temperature independent and can also be used in a high temperature and high pressure environment for humidity sensing.

In order to improve the sensitivity of a reflection type PCFI over a wider RH range an alternative sensor is developed by infiltrating the microholes of the PCF with the hygroscopic material Agarose. The demonstrated novel sensor has a good sensitivity, a fast response time and a compact size. The temperature dependence of the device is also investigated. A novel hybrid device based on Agarose infiltrated PCFI interacting with a

fiber Bragg grating is also presented which can simultaneously measure RH and temperature.

A novel RH sensor based on a transmission type photonic crystal fiber interferometer coated with Agarose is also presented and discussed. This structure is used to study the effect of Agarose coating thickness in such a sensor on the RH sensitivity. It is demonstrated that the RH sensitivity of the sensor has a significant dependence on the thickness of the coating. An experimental method is also demonstrated to select an optimum coating thickness to achieve the highest sensitivity for a given RH sensing range. The sensor with the highest demonstrated sensitivity shows a linear response in the RH ranges of 40-80 % and 80-95 % with a sensitivity of 0.57 nm/%RH and 1.43 nm/%RH respectively.

Finally, a comparison of the four RH sensing devices is presented, based on their size, operating range, RH sensitivity, temperature dependence and response time, in the context of selecting suitable devices for end-user applications. Two examples of applications are presented: dew sensing and breathing monitoring. The reflection type PCFI which does not use any hygroscopic material is selected for dew sensing and the dew response of the device is presented and discussed. Finally a novel breathing sensor based on the Agarose infiltrated PCFI is developed, which due to its immunity to interference from electric and magnetic fields, is suitable for breath monitoring of patients during medical procedures such as a magnetic resonance imaging scan.

DECLARATION

I certify that this thesis which I now submit for examination for the award of Doctor of Philosophy, is entirely my own work and has not been taken from the work of others, save and to the extent that such work has been cited and acknowledged within the text of my work.

This thesis was prepared according to the regulations for postgraduate study by research of the Dublin Institute of Technology and has not been submitted in whole or in part for another award in any other third level institution.

The work reported on in this thesis conforms to the principles and requirements of the DIT's guidelines for ethics in research.

DIT has permission to keep, lend or copy this thesis in whole or in part, on condition that any such use of the material of the thesis be duly acknowledged.

Jinesh Mathew Date: 07 March 2013

ACKNOWLEDGMENT

The work presented in this thesis is the results of the research work carried out for the last four years at DIT Photonics Research Centre (PRC) in School of Electronic and Communications Engineering, Dublin Institute of Technology. At this stage, looking back, I am very delighted to acknowledge the people around me who had supported and shaped my mind so that I could complete the given work and proudly write these lines of my thesis.

First and foremost, I would like to thank my supervisor Prof. Gerald Farrell for giving me an opportunity to work with him and become a part of an excellent research group. I reserve my gratitude for his constant support and guidance given to me throughout my PhD research. His positive approach, lively nature, advices, and encouragements helped me a lot to stay in the right track of my work and to finish my thesis. I would also like to thank him for his patience in reviewing and giving feedback on my thesis.

I am highly thankful to my co-supervisor Dr. Yuliya Semenova for the encouragements, valuable suggestions and support on my research. Her positive attitude and advices gave me the confidence on approaching many problems both in research and life. I sincerely thank her for the careful reading, comments and perspectives given to my thesis.

I am very thankful to people at the PRC: Ginu Rajan, Pengfei Wang, Qiang Wu, Sunish Mathews, Manjusha R, Lin Bo, Youqiao Ma, Mingwei Yang, Abulaiti Hairisha, and Sha Li for accommodating me and for their support and friendship. I am also grateful to the staff of the School of Electronic and Communications Engineering and Graduate Research School office for their kindness and helps. I would also like to thank Marcin Lukas Gradziel of NUI Maynooth for helping me to learn LabVIEW software.

I am highly grateful to my previous supervisor Dr. P Radhakrishnan for giving me the motivation and encouragement during my research at International School of Photonics (ISP) which helped me immensely to prepare for my PhD work here. I would like to thank Mr Thomas K. J. for teaching me the basics of experimental research in fiber optics. I extend my thanks to all my friends in India especially Jijo P. Ulahannan, Lyjo K. Joseph, Linesh J., Deepak T., Asha Prasad, Sony George, Suresh N. L. and Sithara S. P. for their support and friendship. My gratitude also goes to my teachers who moulded my mind and life especially Prof. V.P.N Nampoori, Dr. Devadas K. V. and Mr. Benny Joseph.

Many thanks to my friends in Ireland Joy & Sini, Maneesh & Jitha, Sabu & Shybi, Boban & Jimma, Jinto & Pearl, Ninu, Sobins, Mohesh, Viswanath, Binujith, Prasanth and Sujith, especially for the occasional dinner parties and interactions which made my life in Ireland more enjoyable. My sincere gratitude also goes to Janet Jose who was special to me for some time during my PhD life. I also thank all my friends whom are too many to be listed here for being part of my life and for their helps.

Many thanks to my brother Jains and sisters Jessy, Mini and Jainy, for their support and prayers. I also would like to thank my entire extended family, my sister in law, brother in laws, cousins, uncles, and aunties for all their support and prayers.

I am indebted forever to my beloved parents for their love and raising me up. Thanks to my father, without his, support, blessings and prayers I wouldn't be able to reach in this point of my life. Finally I would like to thank my mother for everything. Without her constant prayers, sacrifice and never ending support, I wouldn't be writing this thesis.

Jinesh Mathew

LIST OF FIRST AUTHOR PUBLICATIONS

Journal Papers

1. **Jinesh Mathew**, Yuliya Semenova and Gerald Farrell, Effect of coating thickness on the sensitivity of a humidity sensor based on an Agarose coated photonic crystal fiber interferometer, Opt. Express, in press.
2. **Jinesh Mathew**, Yuliya Semenova and Gerald Farrell, Fiber optic hybrid device for simultaneous measurement of humidity and temperature, IEEE Sensors, in press.
3. **Jinesh Mathew**, Yuliya Semenova and Gerald Farrell, A miniature optical breathing sensor, Biomed. Opt. Express, 3(12), pp.3325-3331, (2012).
4. **Jinesh Mathew**, Yuliya Semenova and Gerald Farrell, Relative humidity sensor based on an Agarose infiltrated photonic crystal fiber interferometer, IEEE Journal of Selected Topics in Quantum Electronics, 18, pp.1553-1559, (2012).
5. **Jinesh Mathew**, Yuliya Semenova and Gerald Farrell, Photonic crystal fiber interferometer for dew detection, Journal of Lightwave Technology, 30(8), pp.1150-1155, (2012).
6. **Jinesh Mathew**, Yuliya Semenova and Gerald Farrell, A fiber bend based humidity sensor with a wide linear range and fast measurement speed, Sensors and Actuators A: Physical, 174, pp.47-51, (2012).
7. **Jinesh Mathew**, Yuliya Semenova, Ginu Rajan, Pengfei Wang, Gerald Farrell, Improving the sensitivity of a humidity sensor based on fiber bend coated with a hygroscopic coating, Optics & Laser Technology, 43(7), pp.1301-1305, (2011).

8. **Jinesh Mathew**, Yuliya Semenova, Ginu Rajan and Gerald Farrell, Humidity sensor based on a photonic crystal fiber interferometer, Electronics Letters, 46 (19), pp.1341-1343, (2010).

Journal Papers under Review

9. **Jinesh Mathew**, Yuliya Semenova and Gerald Farrell, A high sensitivity humidity sensor based on an Agarose coated photonic crystal fiber interferometer, Applied Optics, under review.

Book Chapter

10. **Jinesh Mathew**, Yuliya Semenova and Gerald Farrell (2012). Photonic crystal fiber interferometer for humidity sensing, Photonic Crystals - Introduction, Applications and Theory, Dr. Alessandro Massaro (Ed.), ISBN: 978-953-51-0431-5, InTech, Chapter 8.

Conference Proceedings

11. **Jinesh Mathew**, Yuliya Semenova and Gerald Farrell, A high sensitivity humidity sensor based on an Agarose coated photonic crystal fiber interferometer, Proc. SPIE 8421, 842177, (2012).
12. **Jinesh Mathew**, Yuliya Semenova and Gerald Farrell, Polymer coated photonics crystal fiber interferometer for relative humidity sensing, Proceedings of IconTop 2011, Kolkatta, India.
13. **Jinesh Mathew**, Yuliya Semenova and Gerald Farrell, A miniature optical humidity sensor, In IEEE Sensors, pp. 2030-2033, (2011).
14. **Jinesh Mathew**, Yuliya Semenova, Ginu Rajan and Gerald Farrell, Photonic crystal fiber interferometer for dew detection, Proc. SPIE 7753, 77531P, (2011).

15. **Jinesh Mathew**, Yuliya Semenova, Ginu Rajan and Gerald Farrell, Agarose coated single mode fiber bend for monitoring humidity, Proc. SPIE 8073, 807317, (2011).
16. **Jinesh Mathew**, Yuliya Semenova, Ginu Rajan, Pengfei Wang and Gerald Farrell, Polyethylene oxide coated single mode fiber bend for monitoring humidity change, in proceedings of International Conference on Sensors and Related Networks (SENNET'09), pp.225-228, (2009).
17. **Jinesh Mathew**, Yuliya Semenova, Ginu Rajan, Pengfei Wang, and Gerald Farrell, A humidity sensor based on a bend singlemode fiber, in Proceedings of photonics Ireland, pp. A66, (2009).
18. **Jinesh Mathew**, Ginu Rajan, Yuliya Semenova and Gerald Farrell, All Fiber tunable loss filter, Proceedings of SPIE Vol. 7503, 75037G, (2009).

LIST OF ABBREVIATIONS

ACFB	Agarose Coated Fiber Bend
AC-PCFI	Agarose Coated Photonic Crystal Fiber Interferometer
AI-PCFI	Agarose Infiltrated Photonic Crystal Fiber Interferometer
BAAP	Breath Analysis Application Programme
BC	Breath Count
BET	Brunauer- Emmett- Teller
BR	Breath Rate
DMSO	Dimethyl Sulfoxide
ESA	Electrostatic Self-Assembly
ET	Elapsed Time
EW	Evanescent Wave
FBG	Fiber Bragg Grating
FOC	Fiber Optic Circulator
LMA	Large Mode Area
LPG	Long Period Grating
MRI	Magnetic Resonance Imaging
OSA	Optical Spectrum Analyzer
OTDR	Optical Time Domain Reflectometer
PBG	Photonic Band Gap
PCF	Photonic Crystal Fiber
PCFI	Photonic Crystal Fiber Interferometer
PD	Photo Detector
PDDA	Poly (diallyldimethylammonium Chloride)
PEO	Polyethylene Oxide

PSS	Poly (Sodium 4-Styrene-Sulfonate)
PVA	Polyvinyl Alcohol
PXI	PCI Extensions for Instrumentation
RH	Relative Humidity
RI	Refractive Index
SLD/ SLED	Super Luminescent Diode
SMF	Single Mode Fiber
TEC	Thermoelectric Cooler

CONTENTS

ABSTRACT.....ii

DECLARATION.....iv

ACKNOWLEDGMENT.....v

LIST OF FIRST AUTHOR PUBLICATIONS.....vii

LIST OF ABBREVIATIONS.....x

CONTENTS.....xii

LIST OF FIGURES.....xvi

LIST OF TABLES.....xxii

1. INTRODUCTION.....1

1.1 Background to the research.....1

1.1.1 Humidity sensing.....1

1.1.2 Fiber optic humidity sensor.....3

1.2 Motivation and aims of the research.....7

1.3 Overview of fiber structures used for RH sensing.....8

1.3.1 A macro-bend single mode fiber.....8

1.3.2 A photonic crystal fiber interferometer.....9

1.4 The objectives of the research.....12

1.5 Research methodology.....13

1.6 Layout of the Thesis.....17

1.7 References.....18

2. RELATIVE HUMIDITY SENSOR BASED ON A FIBER BEND.....33

2.1. Introduction.....33

2.2. Operating principle of the sensor.....34

2.3. Experimental RI characterisation of the fiber bend.....36

2.4. Relative humidity sensor based on Polyethylene oxide coated fiber bend.....38

2.4.1. Experimental results and discussion.....38

2.5. Relative humidity sensor based on an Agarose coated fiber bend.....46

2.5.1. Selection of a suitable coating.....46

2.5.2. Experimental results and discussion.....48

2.6. Limitations of the fiber bend based humidity sensor.....56

2.7. Summary.....57

2.8. References.....58

3. RELATIVE HUMIDITY SENSOR BASED ON A PHOTONIC CRYSTAL FIBER INTERFEROMETER.....61

3.1. Introduction.....61

3.2. Photonic crystal fiber interferometer.....61

3.2.1 PCFI Working Principle.....62

3.2.2 PCFI Fabrication.....64

3.2.3 PCFI Fringe Spacing Vs Length of PCF.....66

3.3. Relative humidity sensor based on PCFI.....67

3.3.1 Experimental characterization of the sensor.....68

3.3.2 Operating principle of the sensor.....70

3.3.3 Performance analysis of the RH sensor.....72

3.3.4 Temperature dependence of the device.....74

3.4. Summary.....75

3.5. References.....76

4. RELATIVE HUMIDITY SENSOR BASED ON AN AGAROSE INFILTRATED PHOTONIC CRYSTAL FIBER INTERFEROMETER.....79

4.1. Introduction.....79

4.2 RH sensor based on Agarose infiltrated PCFI.....80

4.2.1 Operating principle of the sensor.....80

4.2.2. Experimental investigation of the sensor & discussion.....81

4.2.3 Temperature dependence of the sensor.....87

4.2.4 Time response of the sensor.....88

4.2.5 Fabrication repeatability of the sensor.....90

4.3. Simultaneous measurement of humidity and temperature using an Agarose infiltrated PCFI and FBG.....91

4.3.1. Operating principle of the hybrid sensor.....92

4.3.2. Experimental investigation of the hybrid sensor and discussion.....93

4.4. Summary.....99

4.5. References.....100

5. RELATIVE HUMIDITY SENSOR BASED ON AN AGAROSE COATED PHOTONIC CRYSTAL FIBER INTERFEROMETER.....103

5.1. Introduction.....103

5.2. Fabrication and operating principle of transmission type PCFI for RH sensing.....104

5.3. PCF length vs fringe spacing of a transmission type PCFI.....105

5.4. Effect of coating thickness on the sensitivity of a RH sensor based on an Agarose coated photonic crystal fiber interferometer.....107

5.5. A high sensitivity humidity sensor based on an Agarose coated photonic crystal fiber interferometer.....117

5.6. Summary.....125

5.7 References.....127

6. PERFORMANCE COMPARISON OF RH SENSORS FOR DEW SENSING AND BREATHING MONITORING.....130

6.1 Introduction.....130

6.2. Performance comparison of the RH sensors.....130

6.3. Dew sensor based on a PCFI.....135

6.3.1. Introduction.....135

6.3.2. Operating principle of the Dew sensor.....136

6.3.3. Experimental characterization of the sensor……137

6.4. A miniature breathing sensor based on PCFI.....141

6.4.1. Introduction.....141

6.4.2. Experimental demonstration and discussion.....145

6.5. Summary.....151

6.6. References.....152

7. CONCLUSIONS AND FUTURE RESEARCH.....156

7.1 Conclusions from the research.....156

7.2 Over all conclusions from the research.....163

7.3 Future research.....164

7.4 References.....168

APPENDIX A. FIBER-OPTIC SENSING TECHNIQUES FOR HUMIDITY DETECTION.....169

APPENDIX B. EQUIPMENT AND ACCESSORIES.....175

List of Figures

1.1. Examples of applications of humidity sensors in different areas.....2

1.2. A drawing of the reflection type PCF interferometer and a diagram of the cross section of the PCF employed.....11

1.3. A drawing of the transmission type PCF interferometer.....11

1.4. Block diagram of the experimental set-up to study the RH response of the transmission type sensor.....16

1.5. Block diagram of the experimental set-up to study the RH response of the reflection type sensor.....16

2.1. Schematic diagram of a fiber macro-bend.....35

2.2. Transmission response of the bent fiber for different ambient refractive indices.....37

2.3. Resonance wavelength shift as a function of the ambient refractive index.....37

2.4. Poly(ethylene oxide) coated fiber bend.....39

2.5. Experimental setup for studying the humidity response of the PEO coated fiber bend.....40

2.6. Humidity response of the PEO coated fiber bend for RH below 85%.....42

2.7. Appearance of loss dips in the transmission spectrum in a PEO coated fiber bend at RH above 85% due to resonant mode coupling at particular RI values of the coating.....42

2.8. Resonant wavelength shifts to higher wavelengths with the increase of humidity.....42

2.9. Humidity response of the PEO coated fiber bend.....44

2.10. Time response of the fiber-bend based humidity sensor.....44

2.11. Continuous human breath response of the PEO coated fiber bend based sensor.....45
2.12. Experimental arrangement to study the humidity response of the Agarose coated fiber bend.....50
2.13. Transmission response of the ACFB with bend radii 13.25 mm and 16.75 mm and at an ambient humidity 40% RH.....51
2.14. Transmission response of the ACFB at different ambient humidity values.....51
2.15. The insertion loss variation with respect to humidity in the ACFB at different wavelengths.....52
2.16. The humidity sensitivity of the ACFB with respect to wavelength.....53
2.17. Transmission response of the ACFB at humidity values above and below 90% RH, shows a loss dip at 95% RH……...54
2.18. Humidity cycling (60-80% RH) response to show the repeatability and stability of the ACFB.....54
2.19. Temperature dependence of the ACFB at an ambient humidity of 60% RH.....56
2.20. Time response of the ACFB obtained by applying a step change of humidity....56
3.1. Microscope image of the PCFI (upper) & a schematic of the excitation/recombination of modes in the hole collapsed region (lower).....63
3.2. Microscope image of the splice point showing the increase in the microhole collapsed region with respect to number of arcs.....65
3.3. Microhole collapsed region length with respect to the applied number of arcs.....65
3.4. The reflection spectra of interferometers with L = 92 mm, 10.5 mm and 3.5 mm in the wavelength range of 1500-1600 nm.....67
3.5. The fringe spacing as a function of length of PCF observed for a reflection type interferometer.....67

3.6. Experimental arrangement for the characterisation of the PCFI with respect to relative humidity.....69
3.7. Reflection spectrum of a 40.5 mm long PCFI at different humidity values.....69
3.8. Interference peak shift of photonics crystal fiber interferometers with L= 40.5 mm and 17 mm with respect to relative humidity.....70
3.9. Schematic representation of water vapor adsorption mechanisms on an SiO_2 surface.....71
3.10. Interference peak shift with respect to temperature for interferometers with PCF lengths L= 40.5 mm and 17 mm.....75
4.1. A drawing of the sensor head for an Agarose infiltrated photonic crystal fiber interferometer.....82
4.2. The change in the reflection spectrum of a compact PCFI with length ~1 mm with respect to different ambient relative humidity values.....83
4.3. Spectral response of Agarose infiltrated PCFI at different relative humidity values (% RH).....85
4.4. Relative humidity response of the sensor.....87
4.5. Relative humidity response of the sensor taken with a time interval of 60 days showing the long term stability of the sensor.....87
4.6. Temperature dependence of the sensor.....88
4.7. Response time of the sensor.....89
4.8. Relative humidity response of the Agarose infiltrated PCFI with a length of 900 µm.....91
4.9. Schematic diagram of the hybrid fiber optic sensor system for simultaneous measurement of RH and temperature.....94

4.10. Spectral response of the hybrid sensor at constant temperature and different RH.....95
4.11. Power variation of the hybrid sensor response in the region 3 of Fig. 4.10 at a constant temperature and different RH.....95
4.12. The spectral response of the hybrid sensor at constant RH and different temperatures.....96
4.13. Bragg wavelength shift of the hybrid sensor in the region 2 of the Fig. 4.12 at constant RH and different temperatures.....96
4.14. Cross sensitivity of the hybrid sensor in terms of Bragg wavelength (λ_B) at different temperature and RH.....98
4.15. Cross sensitivity of the hybrid sensor in terms of the sensor power variation at 1550 nm for different temperature and RH.....98
5.1. A drawing of the transmission type PCF interferometer and a diagram of the cross section of the PCF employed.....105
5.2. The transmission spectra of interferometers with L = 100 mm, 40 mm, 20 mm and 10 mm in the wavelength range of 1500-1600 nm.....106
5.3. The fringe spacing as a function of length of PCF observed for a transmission type interferometer.....107
5.4. Transmission spectra of different PCFIs with lengths of 40±0.015 mm.....108
5.5. Response to the ambient refractive index changes for different PCFI samples...108
5.6. Schematic diagram of the experimental setup for Agarose coating.....109
5.7. Spectral shift of different devices obtained (a) after single pass of the fiber through the solution (b) after double pass the device through the solution.....110
5.8. Schematic diagram of the experimental setup to study the sensor's response to humidity changes. Inset: a diagram of the Agarose coated interferometer.....112

5.9. The estimated thickness of the four different AC-PCFI devices at room RH of ~60 % and at a higher RH of >90%.....113
5.10. (a) The average spectral peak shift for AC-PCFI samples A and B with respect to relative humidity. (b) The average spectral peak shift for AC-PCFI samples C and D with respect to relative humidity.....116
5.11. Ambient refractive index response of the interferometer with a length of 10 mm.....118
5.12. Evolution of the Agarose coating layer is confirmed by the increase in spectral shift as the number of times the fiber passes through the solution increases.....120
5.13. The spectral responses of the sensor at different relative humidity values.....121
5.14. Spectral peak shift versus ambient relative humidity (error bars shown are calculated from the data obtained from six experimental measurements).....122
5.15. Relative humidity response of the sensor: measurements are taken with an interval of 20 days and show the long term stability of the sensor.....123
5.16. Temperature dependence of the sensor.....124
5.17. Response time of the sensor.....125
6.1. Experimental arrangement for the calibration of PCFI based dew sensor.....138
6.2. Interference spectra for a device with a length of 40.5 mm at room temperature and at dew point temperature.....139
6.3. Interference spectra for a device with a length of 3.5 mm at room temperature and at dew point temperature.....140
6.4. Interference peak shift of the PCFI with respect to temperature at three ambient humidity values of 40, 60 and 80 %RH.....141
6.5. Schematic diagram of a fiber optic breath sensor system, (upper) microscope image of an AI-PCFI and (lower) a photograph of the mask placed on the

volunteer's face showing the position of the sensor inside the mask (dotted line).....145

6.6. Screen shot of the user interface of the breath analysis application program showing the continuous breathing response. Upper plot shows the breathing pattern (inhalation → peaks and exhalation → valleys) and the lower plot indicates the derived breathing state (inhalation → low and exhalation → high).....148

6.7. Screen shot of the user interface of the breath analysis application program showing a breath-hold. Upper plot shows the breathing pattern (inhalation → peaks and exhalation → valleys) and the lower plot indicates the derived breathing state (inhalation → low and exhalation → high).....150

B.1 Block diagram of the LabVIEW software based breathing analysis application programme.....178

List of Tables

5.1. Parameters of the different AC-PCFI devices at ~60 % RH.....111

5.2. RH sensitivity of AC-PCFI devices in different RH regions.....116

5.3. Parameters of the AC-PCFI device at two RH values.....120

6.1. Comparison of different sensors with respect to their measurement range and sensitivity.....131

6.2. Comparison of different sensors with respect to its their size, response time and temperature dependence.....132

6.3. Key advantages and the limitations of the sensors.....133

A.1 Overview of the various fiber-optic sensing techniques for humidity detection.....169

CHAPTER 1. INTRODUCTION

This chapter introduces the background, motivation and objectives of the research, along with the research methodology employed and an overview of the layout of the thesis.

1.1 Background to the research

1.1.1 Humidity sensing

Humidity refers to the water vapor content in air or other gases. It is one of the most frequently measured physical quantities. Humidity measurements can be stated in a variety of terms and units. The three commonly used terms are absolute humidity, dew/frost point and relative humidity (RH). Absolute humidity is the ratio of the mass of water vapor to the volume of air or gas in which the water vapor resides. It is commonly expressed in grams per cubic meter. Dew point is the temperature (above 0 ^{O}C) at which the water vapor in a gas condenses to form liquid water. Frost point is the temperature (below 0 ^{O}C) at which the vapor condenses to ice. Dew/Frost point is expressed in °C or °F and is a function of the pressure of the gas but is independent of temperature, therefore it provides a better absolute measurement of water vapor content. The ratio of the percentage of water vapor present in air at a particular temperature and pressure to the maximum amount of water vapor the air can hold at that temperature and pressure is called relative humidity (*RH*). It is often expressed as a percentage using the following expression,

$$RH = \frac{p_w}{p_{ws}} * 100\% \tag{1.1}$$

where P_w is the partial pressure of the water vapor and P_{ws} is the saturation water vapor pressure. RH is a function of temperature, and thus it is a relative measurement. Most of the humidity sensors available on the market are RH sensors.

Measurement of humidity is required in a range of areas, as illustrated in Fig. 1.1, including meteorological services, the chemical, textile and food processing industry, civil engineering, air-conditioning, horticulture, automotive industry and electronic processing. For example in manufacturing highly sophisticated integrated circuits in the semiconductor industry, humidity or moisture levels are constantly monitored in wafer processing. There are also many domestic applications, such as intelligent control of the living environment in buildings, cooking control for microwave ovens, and intelligent control of laundry drying etc. In the automobile industry, humidity sensors are used in rear window defoggers and motor assembly lines. In the medical field, humidity sensors are used in respiratory equipment, sterilizers, incubators, pharmaceutical processing, and biological products. In general industry, humidity sensors are used for humidity control in chemical gas purification, fuel cells, dryers, ovens, film desiccation, paper and textile production, and food processing. In agriculture, humidity sensors are used for green-house air-conditioning, plantation protection (dew prevention), soil moisture monitoring, and cereal storage.

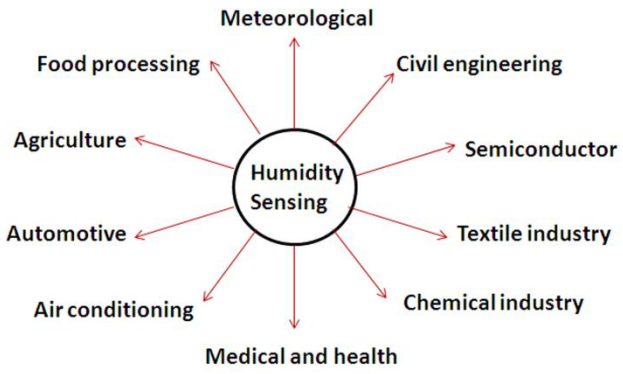

Fig. 1.1. Examples of applications of humidity sensors in different areas.

A review of conventional techniques for humidity sensing is given in [1-7]. They can be classified with respect to the sensing material used into ceramic, electrolyte, semiconductor, and polymer humidity sensors [1-4]. In terms of the transduction techniques they can be classified into mechanical, resistive, capacitive, optical, gravimetric, piezoresistive, and magnetoelastic sensors [5-6]. Optical humidity sensors can be based on a colour changing hologram [8-9], grating/prism coupler [10-12], chilled mirror hygrometer [13] and optical fibers [7, 14-85]. The most important parameters of a humidity sensor are its accuracy, repeatability, long-term stability, ability to recover from condensation, resistance to chemical and physical contaminants, size, cost effectiveness, operating RH range, temperature dependence and response time. Given the wide range of industrial humidity measurement sensors available it is clear that no single measurement technique is suitable for all applications.

1.1.2 Fiber optic humidity sensor

Optical fiber humidity sensors offer specific advantages by comparison to their conventional electronic counterparts. They are:

- Immune to radio frequency interference and electro-magnetic interference
- No explosion risk in volatile atmospheres
- Remote operation possible
- Multiplexing of different sensors is possible
- Excellent corrosion resistance
- Compact size and weight
- High accuracy possible
- Fast response time
- Ease of interfacing to interconnecting optical fibers

- Potentially resistant to ionizing radiation
- Non-metallic and MRI compatible

A wide range of optical fiber humidity sensors have been reported in the literature [7] and a summary overview of their main features and specifications is shown in tabular form in appendix A, classified by the technique used for sensing under the headings: direct spectroscopic, evanescent wave, in-fiber grating and interferometric types.

a. Direct spectroscopic based sensors

Direct spectroscopic method based humidity sensors started to appear in the literature from 1988 onwards. Typically such sensors detect the optical signal obtained from the sensor head and relate the absorption [14-19] or fluorescence [20-22] or luminescence [23] resulting from the presence of water vapor to the concentration of this water vapor, thus allowing for the measurement of RH. Most of the sensors are based on moisture sensitive reagents attached to the sensing fiber, usually with the aid of a polymeric material to form a supporting matrix. Some examples of the reagent materials used for absorption based sensors are $CoCl_2$ [14,15], Crystal violet [16], Rhodamine B [17], etc. Examples of the reagent materials used for the fluorescence based sensors are perylene dyes [20], an aluminium/morin metal ion–organic complex [21], Lithium-treated Nafion membrane [22], etc. Different fiber configurations have been used by various authors and include sensing material attached to the tip of the fiber [20], an air gap between an input and output fiber [17], air-guided photonic crystal fiber [18,19], etc. The typical operating RH ranges of these sensors vary from a narrow range of 8% RH change to wide range of 100% RH. The response time of these sensors is relatively slow and varies from ~118 seconds to a few minutes.

b. Evanescent wave based sensors

Since 1985 onwards several evanescent wave (EW) based humidity sensors have been reported. This sensing method allows the optical fiber to be used as an intrinsic sensor where the EW field generated at the fiber interface interacts with the humidity sensing material surrounding the fiber which in turn allows for the detection of the attenuation/insertion loss [24-48] or the resonant wavelength shift [49-53] of the fiber structure due to the change in refractive index, optical absorption, or scattering of the sensing material with respect to the ambient RH. Again a number of fiber structures have been proposed by various authors, for example a U-bent fiber [24,30-31,33-34], side polished fiber [28,38,49], tapered fiber [32,39,42], etched fiber [50], plastic optic fiber [35,41,43], cladding removed plastic cladded silica fiber [40,48], fiber hetero structure [44,45], etc. A wide variety of sensing materials have also been used and include gelatine [24,27,29,31,42,], polyethylene oxide (PEO) [28,29], polyvinyl alcohol (PVA) [34,37,47], agarose [32,36,40,50,], TiO_2 [49,48], sol-gel silica [38,46,48], chitosan [40], polyaniline [43], nanocoating formed by electro static self assembly or a layer-by-layer technique using different materials [39,44,51,52,53], etc. The RH changes that can be measured by these sensors vary from a range as low as 20% to as high as 90% over the full RH range of 0-100% RH. The response time of these sensors typically varies from a few milliseconds to several minutes.

c. In-fiber grating based sensors

The first RH sensor based on an in-fiber grating was reported by Giaccari et. al. in 2001 [54]. The in-fiber gtratings are created by inducing periodic refractive index modulation of the fiber core. Depending on the grating period they can be classified as fiber Bragg grating (FBG) or long period grating (LPG) sensors. An FBG based RH sensor

commonly uses a sensing material that will expand and induce strain on the FBG with respect to RH [54-61]. LPG based RH sensors are realised by coating the fiber with hygroscopic materials whose refractive index change with respect to RH [62-70]. Examples of sensing materials used with FBGs for RH sensing are polyimide [54-59] and pyralin [61]. Popular materials used along with LPG for RH sensing are carboxy methyl cellulose [62], gelatine [63], PEO [64], PVA [65,66], silica nano spheres [67-69], etc. The typical response time of an FBG based RH sensors vary from a few seconds to several minutes. The reported response time of an LPG based RH sensor is between 30 ms and 80 s. The RH changes that can be measured by these sensors vary from a range as low as 9% to as high as 95% over the RH range of 0-99% RH.

d. Interferometric sensors

The sensing mechanism of an interferometric type fiber optic RH sensor relies on the perturbation of the phase properties of the light signal travelling in an optical fiber introduced by the humidity change. The detection of the phase change is realised by mixing the signal of interest with a reference signal, consequently converting the phase difference between the two signals into an optical intensity change or wavelength shift. The different type of fiber interferometers used for RH sensing are Fabry-Perot (F-P) interferometer [71-78], Michelson interferometer [79-80], modal interferometer [81-82], micro-ring interferometer [83-84], and Sagnac interferometer [85] configurations. Examples of materials used to induce phase change are: SiO_2–TiO_2–SiO_2 [71], SiO_2–(Au:PDDA+ /poly (sodium 4-styrene-sulfonate) (PSS)-) [72], Polyurethane urea - PEO/poly(propylene oxide) [79], SiO_2–(PDDA+ /Poly S119-) [73], Poly R-478- PDDA [74], SiO_2 Nanoparticles [75], PEO [81], chitosan [77,85], PVA [80], etc. The RH changes that can be measured by these sensors vary from a range as low as 38% to as

high as 97% over the full RH range of 0-100% RH and the response times are in the range 120 milliseconds to 1 minute.

In summary the available fiber optic humidity sensors require complex processing of the fiber to allow the light to interact with the water vapor, such as fabrication of gratings, cladding removal, side polishing, tapering, chemical etching or formation of a fiber Fabry-Perot cavity, etc. Also these sensors work on the basis of a hygroscopic material deposited on the optical fiber to modulate the light propagating through the fiber. The chemical process required for the preparation and deposition of these hygroscopic materials on the fiber structures also requires a complex process. Finally in terms of sensor specifications such as operating range, response time, temperature dependence and mechanical stability the performance of these sensors are in many cases limited. The research presented in this thesis set out to address these issues. The fiber structures investigated in this thesis are chosen for their fabrication simplicity and by the use of a hygroscopic material for the sensors that can be easily prepared and coated on the fiber. A fiber optic RH sensor that does not utilise any hygroscopic material is also proposed in this thesis.

1.2 Motivation and aims of the research

The motivation for this research is to investigate a number of approaches to humidity sensing using optical fiber which both overcome the disadvantages of existing fiber optics sensors and which also allow fiber humidity sensors to be applied in new application areas. This study aims to achieve humidity sensors with simple fabrication procedure, wide operating range, good stability and repeatability, fast response time, and high sensitivity. Another goal of this study is to develop a dew sensor and a breathing sensor utilising a suitable potential RH sensor developed in this research. The

novel fiber structures under investigation are an optical fiber bend and different configurations of a photonic crystal fiber interferometer. Since the fabrication of the RH sensors based on these structures is simple and low cost, disposable humidity sensors can be developed using them which is useful to overcome the contamination effects by simply replacing the sensor. Sensor contamination over time is a serious problem that needs to be addressed in the case of any fiber optic humidity sensor.

1.3 Overview of fiber structures used for RH sensing

The following subsections introduce the fiber structures used for RH sensing in this thesis

1.3.1 A macro-bend single mode fiber

Since the advent of optical waveguides the phenomenon of bend-induced losses has been recognized [86-87]. Macro-bend loss is the radiative loss that occurs when the bend radius is relatively small. Bend loss in single mode fiber is usually regarded as an adverse effect in the context of optical transmission, but utilizing the bending loss in fiber has led to the development of many fiber devices with a variety of applications [88-94]. Theoretically, bend loss in optical fibers has been shown to be a monotonic function of wavelength, assuming a cladding of infinite extent [95]. A finite cladding thickness leads to an oscillatory bend loss as a function of the bend radius (R) and wavelength. This oscillation in bent optical fibers has been attributed to so-called Whispering Gallery mode resonance and been studied by several authors experimentally and theoretically [96-98]. A strong resonant dip was demonstrated with a jacket-removed cladding-thinned optical fiber in [99] for high temperature sensing. An alternate approach to the physical description and quantification of bend loss in a bent single mode fiber, based on the coupling of the fundamental mode to cladding modes

caused by curvature change, was demonstrated in [100-105]. A variety of sensing applications of a macro bent optical fiber have been demonstrated, which include wavelength measurement based on macrobending singlemode fiber [88-90], temperature sensor [91], refractive index sensor [92], displacement sensor [93], and a voltage sensor [94].

For the purpose of humidity sensing, since a buffer stripped fiber bend is sensitive to ambient refractive index, a humidity sensor is possible using a fiber bend structure by coating its surface with a hygroscopic material whose refractive index changes with respect to the ambient humidity. Unlike other fiber optic humidity sensors with a hygroscopic coating a bent SMF does not require any complex processing of the fiber itself.

1.3.2 A photonic crystal fiber interferometer

Photonic crystal fibers (PCFs), which are also called microstructured optical fibers or holey fibers, have been extensively investigated and since they appeared in the mid 1990s [106-108] have considerably increased the range of applications possible compared to traditional optical fiber. PCFs have a periodic array of microholes that run along the entire fiber length. They typically have two kinds of cross sections: an air-silica cladding surrounding a solid silica core or an air-silica cladding surrounding a hollow core. The light-guiding mechanism of the former is provided by means of a modified total internal reflection (index guiding), while the light-guiding mechanism of the latter is based on the photonic band gap effect (PBG guiding). The number, size, shape, and the separation between the air-holes as well as the air-hole arrangement are parameters which define the guiding mechanism and modal properties of PCF [109]. The structure is what gives PCF many of its unique properties such as single mode

operation over a wide wavelength range [110], very large mode area [111], and ultraflattened chromatic dispersion with low losses [112]. Because of the very many design variations developed with novel wave-guiding properties, PCFs have been used for a number of novel fiber-optic devices and fiber-sensing applications that are difficult to realize using conventional fibers.

While traditional optical interferometers offer high resolution in metrology applications, the use of fiber optic technology additionally offers some advantages such as mechanical stability, compactness and absence of moving parts for the construction of interferometers. The two common approaches to building of a fiber optic interferometer are: two-arm interferometer and modal interferometer. A two-arm interferometer involves splitting and recombining two monochromatic optical beams that propagate in different fibers which requires several meters of optical fiber and one or two couplers. A modal interferometer on the other hand exploits the relative phase displacement between two modes of the same fiber. In modal interferometers by comparison to their two-arm counterparts, the susceptibility to environmental fluctuations is reduced because the modes propagate in the same path or fiber. The unique properties of the photonic crystal fibers offer many interesting possibilities for the design of fiber interferometers and as a result have attracted much interest from the optical fiber sensor community. The design of PCF based interferometers in particular is interesting owing to their proven high sensitivity and wide range of applications. Some photonic crystal fiber based modal interferometers reported to date include PCFs in a fiber loop mirror [113], interferometer built with long period gratings [114], interferometers built with tapered PCFs [115], and interferometers fabricated via micro-hole collapse [116-118]. The latter technique is really simple since it only involves cleaving and splicing. The different configurations reported so far are a PCF with two collapsed regions separated

by a few centimetres [116,117], a short section of a PCF longitudinally sandwiched between standard single mode fibers by fusion splicing (transmission type) [118] and a stub of PCF with cleaved end fusion spliced at the distal end of a single mode fiber (reflection type) [119]. The advantage of the last two configurations is that the modal properties of the PCF are exploited but the interrogation is carried out with conventional optical fibers, thus leading to more cost-effective interferometers. Therefore the latter two configurations (see Fig. 1.2 and 1.3) are investigated in this thesis for humidity sensing. The different structures investigated for humidity sensing are a reflection type PCF interferometer without using any hygroscopic material, an Agarose infiltrated reflection type PCFI and an Agarose coated transmission type PCFI. Several aspects of PCFI based sensors are investigated in this thesis; including the relation between lengths of PCF and the fringe spacing, temperature dependence, response time, and effect of Agarose coating thickness on the sensitivity of the sensor.

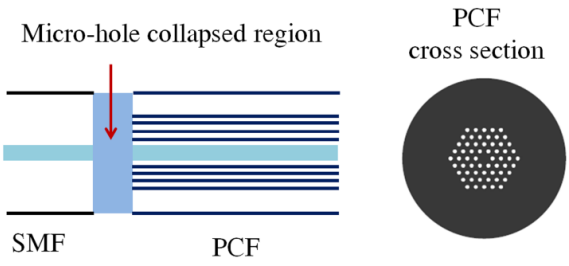

Fig. 1.2. A drawing of a reflection type PCF interferometer and a diagram of the cross section of the PCF employed. (SMF- single mode fiber, PCF- photonic crystal fiber).

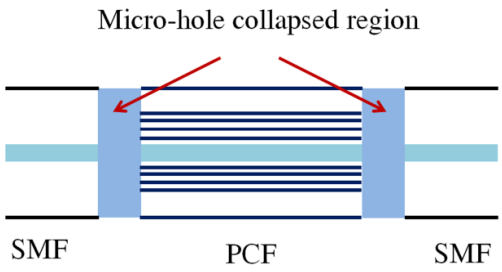

Fig. 1.3. A drawing of a transmission type PCF interferometer (SMF- single mode fiber, PCF- photonic crystal fiber).

All these structures can provide humidity information by either spectral measurements or measurements of intensity/power variations of the transmitted/reflected light. The sensors demonstrated also have a fast response compared to other mechanical/electronic humidity sensors and can, for example, be used as a breath monitor in medical applications and potentially in many other chemical, biological and industrial applications.

1.4 The objectives of the research

In line with the motivations and aims of the research outlined previously, the specific objectives of the research are as follows:

A. Develop and characterise RH sensors based on a fiber bend

This will involve the investigation of the RH response of a PEO and an Agarose coated fiber bend along with the investigation of the temperature dependence and the response time of an Agarose coated fiber bend.

B. Develop and characterise an RH sensor based on an open ended PCFI

This will involve the investigation of the effect of length of PCF on the fringe spacing of a reflection type PCFI, investigation of the RH response of an reflection type PCFI and the investigation of the temperature dependence of the reflection type PCFI.

C. Develop and characterise an RH sensor based on an Agarose infiltrated reflection type PCFI

This will involve the investigation of the RH response of an Agarose infiltrated reflection type PCFI, investigation of the response time of an Agarose infiltrated reflection type PCFI, investigation of the temperature dependence of an Agarose

infiltrated reflection type PCFI, and investigation of a new method for the simultaneous measurement of RH and temperature using an Agarose infiltrated reflection type PCFI and an in-line fiber Bragg grating.

D. Develop and characterise an RH sensor based on an Agarose coated transmission type PCFI

This will involve the investigation of the effect of coating thickness on the sensitivity of a humidity sensor based on transmission type PCFI, the investigation of the RH response of an Agarose coated transmission type PCFI, investigation of the temperature dependence of an Agarose coated transmission type PCFI, and the investigation of the response time of an Agarose coated transmission type PCFI.

C. Carry out a performance comparison of the RH sensors developed and use this comparison to select suitable devices for dew sensing and breathing monitoring

This will involve the investigation of the dew response of a reflection type PCFI and investigation of breathing response of an Agarose infiltrated reflection type PCFI.

1.5 Research methodology

For the various research strands pursued in this thesis, the typical research methodology employed consists of a sequence of steps as follows:

I. Carry out an analysis of light propagation in the sensor.

Analysis of light propagation in the fiber structure to underpin the development of an explanation and understanding of the operation of the sensor.

II. Develop techniques to fabricate the sensor head.

In this research, all the fiber structures were fabricated using a Fujikura CT-30 cleaver and a Sumitomo type-36 fusion splicer. The specific methodologies involved for the different sensors are:

a. Fabrication of a fiber bend:

First, the input SMF and the input end of a high bend loss fiber (1060XP) were cleaved and spliced together. The cleaver was then used again to cleave the other end of the high bend loss fiber to the required length. The output end of high bend loss fiber section was spliced to the cleaved end of the output SMF. Finally, a fiber bend with a desired bend radius is achieved by fixing the fiber on to a semicircular rod of desired outer diameter or by attaching the bend fiber between a fixed and a translating support.

b. Fabrication of a PCFI:

A required length of PCF with its protection coating removed and both ends cleaved is taken. The cleaved end of the input SMF and the input end of the PCF are fusion spliced together to form a reflection type PCFI. The transmission type PCFI can be formed by again fusion splicing the output end of the PCF section to the cleaved end of the output SMF.

III. Develop techniques to allow coating or infiltration

Chemical processes:

It involves the preparation of a hygroscopic material solution and coating the fiber with the solution. The PEO/Agarose solution is prepared by dissolving a suitable quantity of PEO or Agarose in distilled water. The PEO coated fiber bend is fabricated by coating

the buffer-striped portion of the fiber with a PEO solution. The Agarose coated fiber bend is fabricated by passing the buffer-striped portion of the fiber through a hot Agarose solution. The Agarose infiltrated PCFI is fabricated by infiltrating the microholes of the reflection type PCFI with hot Agarose solution via capillary action. The Agarose coated PCFI is fabricated by passing the transmission type PCFI through a hot Agarose solution.

IV. Develop an experimental set-up to study the RH response of the sensors

a. Controlling the humidity environment:

The humidity response of the sensors is studied by placing the sensor in a controlled environment chamber (Electro Tech Systems inc., Model 5503-00 with Package F). The operating system of the environment chamber consists of a closed loop desiccant/pump dehumidification system, ultrasonic humidification system, solid state thermo electric cooling system and an electric strip heating system. The control system consists of a microprocessor based control unit and the feedback sensors for RH and temperature. Using this system both the temperature (range = 10-55 ^{O}C, accuracy $\geq \pm 1$ ^{O}C) and relative humidity (range = 0-100% RH, accuracy = ±2% RH) inside the chamber can be varied and controlled. Saturated salt solutions are used as an RH standard to verify the readings of the electronic hygrometer.

b. Optical characterisation of the sensors:

To characterise sensors the generic experimental setup takes one of two forms, depending on the sensor type. The generic setup for transmission type sensors is composed of a light source, sensor head and a light detector as shown in Fig. 1.4. For an end type sensor head such as open ended PCFI, a fiber optic coupler/circulator is used

to couple the light between source, sensor head and the detector as shown in Fig. 1.5. The light sources used are either a broadband light source, SLED (COVEGA Corporation, SLD6593) or a single wavelength light source, Tunable laser (Anritsu, Tunics plus CL/WB). The light detector used to monitor the response of the sensor is an optical power meter (PX Instrument Technology, PX2000-306) or an optical spectrum analyser (Advantest, Q8384).

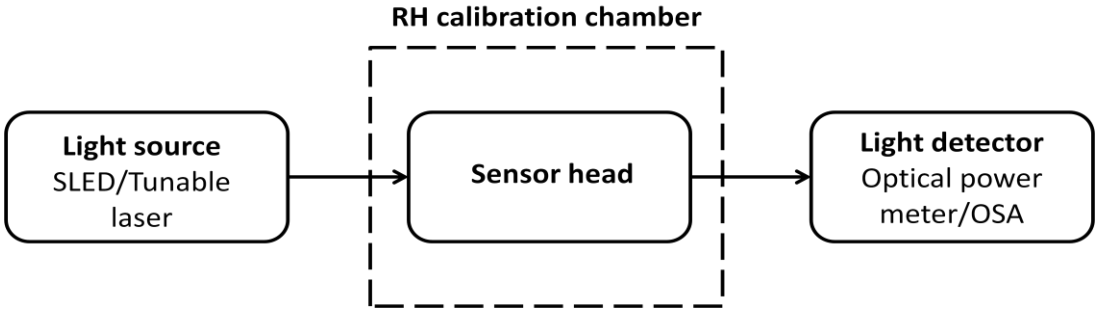

Fig. 1.4 Block diagram of the generic experimental set-up to study the RH response of the transmission type sensor

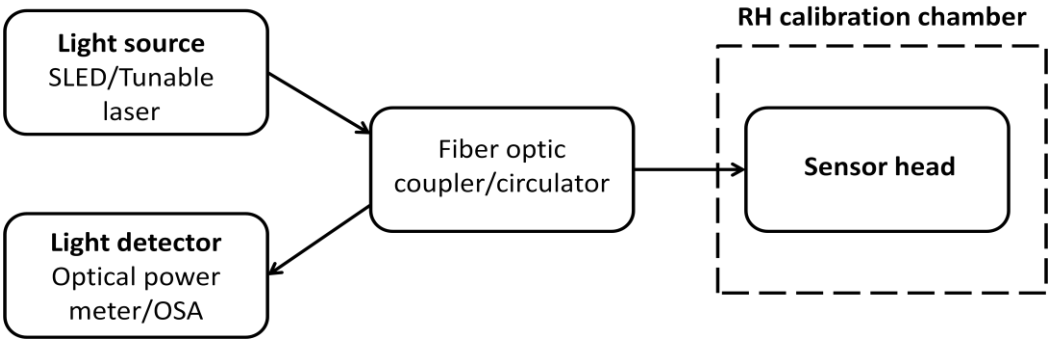

Fig. 1.5 Block diagram of the generic experimental set-up to study the RH response of the reflection type sensor

V. Carry out a performance comparison of the developed RH sensors

A performance comparison of the relative humidity sensors developed is carried out based on parameters such as RH range, RH sensitivity, response time, sensor size, temperature dependence, advantages and limitations of the sensor. As an outcome of

this determine the best sensor configuration for two candidate applications: Dew point sensing and human breath monitoring.

1.6 Layout of the Thesis

This dissertation is focussed on the design and experimental demonstration of humidity sensors with an emphasis on high sensitivity, fast response time and wide range.

Chapter 1 is this introduction chapter which introduces the background, motivation and objectives of the research. The research methodology and an overview of the layout of the thesis are also included.

Chapter 2 presents the studies of fiber bend based RH sensor with a focus on achieving high sensitivity in a wide operating range. A PEO coated fiber bend and an Agarose coated fiber bend are studied in this chapter. The operating principle of the sensor, the RH response of the sensor, temperature dependence and the response time of the sensor are discussed in this chapter.

Chapter 3 presents the studies of a RH sensor based on open ended reflection type PCFI with the key advantage that no hygroscopic materials are needed. The fabrication, operating principle of the sensor, RH response and temperature dependence of the sensor are discussed in this chapter.

Chapter 4 presents the studies of an RH sensor based on an Agarose infiltrated reflection type PCFI. The novel concept for achieving an improved sensitivity with a miniature size of the sensor is demonstrated in detail. The operating principle, RH response, repeatability, long term stability, temperature dependence and response time of the sensor are explained in this chapter. This chapter also demonstrates a fiber optic

hybrid device using an Agarose infiltrated PCFI and an in-line fiber Bragg grating for simultaneous measurement of humidity and temperature.

Chapter 5 presents the studies of an RH sensor based on an Agarose coated transmission type PCFI. This chapter experimentally demonstrates the effect of coating thickness on the RH sensitivity of the sensor. The fabrication, operating principle, RH response, repeatability, long term stability, temperature dependence and response time of the sensor are discussed in this chapter.

In Chapter 6 a performance comparison of the relative humidity sensors developed is provided in terms of RH range, RH sensitivity, response time, sensor size, temperature dependence, advantages and limitations of the sensor. Based on the advantages such as wide RH range of operation, high sensitivity, fast response time, dispensing with the need for a hygroscopic material/silica only sensor head, type of the probe (end-type or in-line), disposability of the sensor head, small sensor head size, low temperature dependence, the sensors for suitable derived application are identified in this chapter. The chapter also presents the dew response of an open ended PCFI and the breathing response of an Agarose infiltrated PCFI.

Finally the conclusions arising from the research and future research plans are presented in Chapter 7.

Two appendices are also provided detailing other information such as overview of the various fiber-optic sensing techniques for humidity detection, the LabVIEW program for the breathing analysis application and details of the equipment and accessories used.

1.7 References

1. H. Arai, and T. Seiyama, Humidity sensors, *Sensors Set*, pp. 981-1012, (2008).

2. B. M. Kulwicki, Humidity sensors, *Journal of the American Ceramic Society*, *74*(4), pp. 697-708, (1991).
3. N. Yamazoe, Y. Shimizu, Humidity sensors: principles and applications, *Sensors and Actuators*, *10*(3), pp. 379-398, (1986).
4. Z. Chen, and C. Lu, Humidity sensors: a review of materials and mechanisms. *Sensor Letters*, *3*(4), pp. 274-295, (2005).
5. Z. M. Rittersma, Recent achievements in miniaturised humidity sensors-a review of transduction techniques, *Sensors and Actuators A: Physical*, *96*(2), pp. 196-210, (2002).
6. C. Y. Lee, and G. B. Lee, Humidity sensors: a review, *Sensor Letters*, 3, 1(4), 1-15, (2005).
7. T.L. Yeo , T. Sun, K.T.V. Grattan, Fiber-optic sensor technologies for humidity and moisture measurement, *Sens Actuators A Phys*, 144, pp. 280–295, (2008).
8. I. Naydenova, R. Jallapuram, V. Toal, and S. Martin, A visual indication of environmental humidity using a color changing hologram recorded in a self-developing photopolymer, *Applied Physics Letters*, 92(3), pp. 031109-031109, (2008).
9. I. Naydenova, R. Jallapuram, V. Toal, and S. Martin, Characterisation of the humidity and temperature responses of a reflection hologram recorded in acrylamide-based photopolymer, *Sensors and Actuators B: Chemical*, 139(1), pp. 35-38, (2009).
10. K.J. Lee, D. Wawro, P.S. Priambodo, R. Magnusson, Agarose-gel based guided-mode resonance humidity sensor, *IEEE Sens J*, 7(3), pp. 409-414, (2007).
11. M. V. Fuke, A. Vijayan, P. Kanitkar, M. Kulkarni, B. B. Kale, and R. C. Aiyer, Ag-polyaniline nanocomposite cladded planar optical waveguide based humidity

sensor, *Journal of Materials Science: Materials in Electronics*, *20*(8), pp. 695-703, (2009).

12. B. C. Yadav, N. K. Pandey, A. K. Srivastava, and P. Sharma, Optical humidity sensors based on titania films fabricated by sol-gel and thermal evaporation methods, *Measurement Science and Technology*, *18*(1), pp. 260, (2006).
13. D. J. Beaubien, The chilled mirror Hygrometer: how it works, where it works-and where it doesn't, *Sensors*, 22(5), pp. 30-34, (2005).
14. Q. Zhou, M.R. Shahriari, D. Kritz, and G.H. Sigel Jr., Porous fiber-optic sensor for high-sensitivity humidity measurements, *Anal. Chem.*, 60, pp. 2317-2320, (1988).
15. S. Tao, C.B. Winstead, R. Jindal, and J.P. Singh, Optical-fiber sensor using tailored porous sol-gel fiber core, *IEEE Sens. J.*, 4, pp.322-328, (2004).
16. T.E. Brook, M.N. Taib, and R. Narayanaswamy, Extending the range of a fiber-optic relative humidity sensor, *Sens. Actuators B*, 38-39, pp. 272-276, (1997).
17. S. Otsuki, K. Adachi, T. Taguchi, A novel fiber-optic gas sensing arrangement based on an air gap design and an application to optical detection of humidity, *Anal. Sci.*, 14, pp. 633-635, (1998).
18. M. M. Noor, N. Khalili, I. Skinner, and G. D. Peng, Optical relative humidity sensor based on a hollow core-photonic bandgap fiber. *Measurement Science and Technology*, *23*(8), pp. 085103, (2012).
19. M. M. Noor, N. Khalili, I. Skinner, and G. D. Peng, Optical humidity sensor based on air guided photonic crystal fiber. *Photonic Sensors*, *2*(3), pp. 277-282, (2012).
20. H.E. Posch, and O.S. Wolfbeis, Fiber-optic humidity sensor based on fluorescence quenching, *Sens. Actuators*. 15, pp. 77-83, (1988).

21. A. Raichur, H. Pedersen, Fiber optic moisture sensor for baking and drying process control, *proc. food processing automation iV, Am. Soc. Agric. Eng*., pp. 180-189, (1995).
22. S.J. Glenn, B.M. Cullum, R.B. Nair, D.A. Nivens, C.J. Murphy, S.M. Angel, Lifetime-based fiber-optic water sensor using a luminescent complex in a lithium-treated Nafion membrane, *Anal. Chim. Acta*, 448, pp.1-8, (2001).
23. M. Bedoya, M.T. Diez, M.C. Moreno-Bondi, G. Orellana, Humidity sensing with a luminescent Ru(II) complex and phase-sensitive detection, *Sens. Actuators B*, 113, pp.573-581, (2006).
24. A.P. Russell, K.S. Fletcher, Optical sensor for the determination of moisture, *Anal. Chim. Acta*, 170, pp.209-216, (1985).
25. K. Ogawa, S. Tsuchiya, H. Kawakami, Humidity sensing effects of optical fibers with microporous SiO_2 cladding, *Electron. Lett*. 24 (1), pp.42-43, (1988).
26. W. C. Michie, B. Culshaw, M. Konstantaki, I. McKenzie, S. Kelly, N. B. Graham, and C. Moran, Distributed pH and water detection using fiber-optic sensors and hydrogels, *Lightwave Technology, Journal of*, 13(7), pp.1415-1420, (1995).
27. A. Kharaz, B. Jones, A distributed fiber optic sensing system for humidity measurement, *Meas. Contr*. 28, pp.101–103, (1995).
28. D. C. Bownass, J. S. Barton, and J. D. Jones, Serially multiplexed point sensor for the detection of high humidity in passive optical networks, *Optics letters*, 22(5), pp.346-348, (1997).
29. D. C. Bownass, J. S. Barton, and J. D. C. Jones, Detection of high humidity by optical fiber sensing at telecommunications wavelengths, *Optics communications*, 146(1-6), pp.90-94, (1998).

30. S. Otsuki, K. Adachi, T. Taguchi, A novel fiber optic gas sensing configuration using extremely crived optical fibers and an attempt for optical humidity detection, *Sens. Actuators B* 53, pp.91-96, (1998).
31. A. Kharaz, B.E. Jones, K.F. Hale, L. Roche, and K. Bromley, Optical fiber relative humidity sensor using a spectrally absorptive material, in: SPIE Proceedings of International Conference on Optical Fiber Sensors, vol. 4185, Venice, Italy, pp. 370–373, (2000).
32. C. Bariain, I.R. Matias, F.J. Arregui, and M. Lopez-Amo, Optical fiber humidity sensor based on a tapered fiber coated with agarose gel, *Sens. Actuators B*, 69, pp.127–131, (2000).
33. B.D. Gupta, and Ratnanjali, A novel probe for a fiber optic humidity sensor, *Sens. Actuators B*, 80, pp.132–135, (2001).
34. R. Jindal, S. Tao, J.P. Singh, and P.S. Gaikwad, High dynamic range fiber optic relative humidity, *Opt. Eng.*, 41 (5), pp.1093–11093, (2002).
35. S. Muto, O. Suzuki, T. Amano, and M. Morisawa, A plastic optical fiber sensor for real-time humidity monitoring, *Meas. Sci. Technol.*, 14, pp.746–750, (2003).
36. F.J. Arregui, Z. Ciaurriz, M. Oneca, and I.R. Matias, An experimental study about hydrogels for the fabrication of optical fiber humidity sensors, *Sens. Actuators B*, 96(1), pp.165-172, (2003).
37. A. Gaston, F. Perez, and J. Sevilla, Optical fiber relative humidity sensor with polyvinyl alcohol film, *Appl. Opt*. 43 (21), pp.4127–4132, (2004).
38. L. Xu, J. C. Fanguy, K. Soni, and S. Tao, Optical fiber humidity sensor based on evaenscent wave scattering, *Opt. Lett*. 29 (11), pp.1191–1193, (2004).

39. J.M. Corres, J. Bravo, I.R. Matias, Nonadiabatic tapered single-mode fiber coated with humidity sensitive nanofilms, *IEEE Photonics Technol. Lett*. 18 (8), pp.935–937, (2006).
40. J. Mathew, K. J. Thomas, V. P. N. Nampoori, and P. Radhakrishnan, A comparative study of fiber optic humidity sensors based on chitosan and agarose, *Sens. Transducers J*, 84(10), pp.1633-1640, (2007).
41. S. Acikgoz, B. Bilen, M. M. Demir, Y. Z. Menceloglu, Y. Skarlatos, G. Aktas, and M. N. Inci, Use of polyethylene glycol coatings for optical fiber humidity sensing, *Optical review*, 15(2), pp.84-90, (2008).
42. L. Zhang, F. Gu, J. Lou, X. Yin, and L.Tong, Fast detection of humidity with a subwavelength-diameter fiber taper coated with gelatin film, *Optics Express*, 16(17), pp.13349-13353, (2008).
43. A.Vijayan, M. Fuke, R. Hawaldar, M. Kulkarni, D. Amalnerkar, and R. C. Aiyer, Optical fiber based humidity sensor using Co-polyaniline clad, *Sensors and Actuators B: Chemical*, 129(1), pp.106-112, (2008).
44. S. Akita, H. Sasaki, K. Watanabe, and A. Seki, A humidity sensor based on a hetero-core optical fiber, *Sensors and Actuators B: Chemical*, 147(2), pp.385-391, (2010).
45. J. M. Corres, Y. R. Garcia, F. J. Arregui, and I. R. Matias, Optical fiber humidity sensors using PVdF electrospun nanowebs, *Sensors Journal, IEEE*, 11(10), pp.2383-2387, (2011).
46. Z. Zhao, and Y. Duan, A low cost fiber-optic humidity sensor based on silica sol-gel film, *Sensors and Actuators B: Chemical*, 160, pp.1340-1345, (2011).

47. T. Li, X. Dong, C. C. Chan, C. L. Zhao, and P. Zu, Humidity Sensor Based on a Multimode-Fiber Taper Coated With Polyvinyl Alcohol Interacting With a Fiber Bragg Grating, *Sensors Journal, IEEE*, 12(6), pp.2205-2208, (2012).
48. R. Aneesh, and S. K. Khijwania, Titanium dioxide nanoparticle based optical fiber humidity sensor with linear response and enhanced sensitivity, *Applied Optics*, 51(12), pp.2164-2171, (2012).
49. A. Alvarez-Herrero, H. Guerrero, D. Levy, High-sensitivity sensor of a low relative humidity based on overlay on side-polished fibers, *IEEE Sens. J.*, 4 (1), pp.52–56, (2004).
50. M. Hernaez, C. R. Zamarreño, C. Fernandez-Valdivielso, I. Del Villar, F. J. Arregui, and I. R. Matias, Agarose optical fiber humidity sensor based on electromagnetic resonance in the infra-red region, *physica status solidi (c)*, 7(11-12), pp.2767-2769, (2010).
51. C. R. Zamarreño, M. Hernaez, I. Del Villar, I. R. Matias, and F. J. Arregui, Tunable humidity sensor based on ITO-coated optical fiber, *Sensors and Actuators B: Chemical*, *146*(1), pp.414-417, (2010).
52. P. Sanchez, C. R. Zamarreño, M. Hernaez, I. Del Villar, C. Fernandez-Valdivielso, I. R. Matias, and F. J. Arregui, Lossy mode resonances toward the fabrication of optical fiber humidity sensors, *Measurement Science and Technology*, 23(1), 014002, (2011).
53. P. J. Rivero, A. Urrutia, J. Goicoechea, and F. J. Arregui, Optical fiber humidity sensors based on Localized Surface Plasmon Resonance (LSPR) and Lossy-mode-resonance (LMR) in overlays loaded with silver nanoparticles, *Sensors and Actuators B: Chemical*. 173, pp. 244–249, (2012).

54. P. Giaccari, H. G. Limberger, and P. Kronenberg, Influence of humidity and temperature on polyimide-coated fiber Bragg gratings, in Proc. Trends in Optics and Photonics Series: Bragg Gratings, Photosensitivity, and Poling in Glass Waveguides, Washington DC, 2001, vol 61, pp. BFB2.
55. P. Kronenberg, P.K. Rastogi, P. Giaccari, H.G. Limberger, Relative humidity sensor with optical fiber Bragg grating, *Opt. Lett*. 27, pp.1385-1387, (2002).
56. T. L. Yeo, T. Sun, K. T. Grattan, D. Parry, R. Lade, and B. D. Powell, Polymer-coated fiber Bragg grating for relative humidity sensing, *Sensors Journal, IEEE*, 5(5), pp.1082-1089, (2005).
57. T. L. Yeo, T. Sun, K. T. V. Grattan, D. Parry, R. Lade, and B. D. Powell, Characterisation of a polymer-coated fiber Bragg grating sensor for relative humidity sensing, *Sensors and Actuators B: Chemical*, 110(1), pp.148-156, (2005).
58. X. F. Huang, D. R. Sheng, K. F. Cen, and H. Zhou, Low-cost relative humidity sensor based on thermoplastic polyimide-coated fiber Bragg grating, *Sensors and Actuators B: Chemical*, 127(2), pp.518-524, (2007).
59. C. Zhang, W. Zhang, D. J. Webb, and G. D. Peng, Optical fiber temperature and humidity sensor, *Electronics letters*, 46(9), pp.643-644, (2010).
60. S. F. Correia, P. Antunes, E. Pecoraro, P. P. Lima, et al. Optical fiber relative humidity sensor based on a FBG with a Di-Ureasil coating, *Sensors*, 12(7), pp.8847-8860, (2012).
61. N. A. David, P. M. Wild, and N. Djilali, Parametric study of a polymer-coated fiber-optic humidity sensor, *Measurement Science and Technology*, 23(3), 035103, (2012).

62. S. Luo, Y. Liu, A. Sucheta, M. Evans, and R. van Tassell, Applications of LPG fiber optical sensors for relative humidity and chemical warfare agents monitoring, in: Proceedings Advanced Sensor Systems and Applications, vol. 4920, 2002, pp. 193–204.
63. K.M. Tan, C.M. Tay, S.C. Tjin, C.C. Chan, and H. Rahardjo, High relative humidity measurements using gelatin coated long-period grating sensors, *Sens. Actuators B* 110, pp.335–341, (2005).
64. M. Konstantaki, S. Pissadaki, S. Pispas, N. Madamopoulous, N.A. Vainos, Optical fiber long period grating humidity sensor with PEO/$CoCl_2$ coating, *Appl. Opt*. 45, pp.4567–4571, (2006).
65. T. Venugopalan, T. L. Yeo, T. Sun, and K. T. V. Grattan, LPG-based PVA coated sensor for relative humidity measurement, *Sensors Journal, IEEE*, 8(7), pp.1093-1098, (2008).
66. T. Venugopalan, T. Sun, and K. T. V. Grattan, Long period grating-based humidity sensor for potential structural health monitoring, *Sensors and Actuators A: Physical*, 148(1), pp.57-62, (2008).
67. D. Viegas, J. Goicoechea, J. L. Santos, F. M. Araújo, L. A. Ferreira, F. J. Arregui, and I. R. Matias, Sensitivity improvement of a humidity sensor based on silica nanospheres on a long-period fiber grating, *Sensors*, 9(1), pp.519-527, (2009).
68. D. Viegas, J. Goicoechea, J. M. Corres, J. L. Santos, L. A. Ferreira, F. M. Araújo, and I. R. Matias, A fiber optic humidity sensor based on a long-period fiber grating coated with a thin film of SiO_2 nanospheres, *Measurement Science and Technology*, 20(3), 034002, (2009).

69. D. Viegas, M. Hernaez, J. Goicoechea, J. L. Santos, F. M. Araújo, F. J. Arregui, and I. R. Matias, Simultaneous Measurement of Humidity and Temperature Based on an SiO_2 Nanospheres Film Deposited on a Long-Period Grating In-Line With a Fiber Bragg Grating, *Sensors Journal, IEEE*, 11(1), pp.162-166, (2011).
70. M. Y. Fu, G. R. Lin, W. F. Liu, and C. Wu, Fiber-optic humidity sensor based on an air-gap long period fiber grating, *Optical review*, 18(1), pp.93-95, (2011).
71. F. Mitschke, Fiber optic sensor for humidity, *Opt. Lett*. 14 (7), pp.967–969, (1989).
72. F.J. Arregui, Y. Liu, I.R. Matias, R.O. Claus, Optical fiber humidity sensor using a nano Fabry–Perot cavity formed by the ionic self-assembly method, *Sens. Actuators B*, 59, pp.54–59, (1999).
73. H. H. Yu, L. Yao, L. X. Wang, W. B. Hu, and D. S. Jiang, Fiber optic humidity sensor based on self-assembled polyelectrolyte multilayers. *Journal Wuhan University of Technology, Materials Science Edition*, *16*(3), pp.65-69, (2001).
74. F. J. Arregui, I. R. Matias, K. L. Cooper, and R. O. Claus, Simultaneous measurement of humidity and temperature by combining a reflective intensity-based optical fiber sensor and a fiber Bragg grating, *Sensors Journal, IEEE*, 2(5), pp.482-487, (2002).
75. J. M. Corres, I. R. Matías, M. Hernáez, J. Bravo, and F. J. Arregui, Optical fiber humidity sensors using nanostructured coatings of SiO_2 nanoparticles, *Sensors Journal, IEEE*, 8(3), pp.281-285, (2008).
76. M. Consales, A. Buosciolo, A. Cutolo, G. Breglio, A. Irace, et al., Fiber optic humidity sensors for high-energy physics applications at CERN, *Sensors and Actuators B: Chemical*, 159(1), pp.66-74, (2011).

77. L. H. Chen, T. Li, C. C. Chan, R. Menon, P. Balamurali, et al., Chitosan based fiber-optic Fabry-Perot humidity sensor, *Sensors and Actuators B: Chemical*. 169, pp. 167-172, (2012).
78. J. Yao, T. Zhu, D. W. Duan, and M. Deng, Nanocomposite polyacrylamide based open cavity fiber Fabry–Perot humidity sensor, *Applied Optics*, *51*(31), pp.7643-7647, (2012).
79. P. Kronenberg, B. Culshaw, G. Pierce, Development of a novel fiber optic sensor for humidity monitoring, in: *Proceedings SPIE Conference on Sensory Phenomena and Measurement Instrumentation for Smart Structures and Materials*, 1999, pp. 480–485.
80. W. C. Wong, C. C. Chan, L. H. Chen, T. Li, K. X. Lee, and K. C. Leong, Polyvinyl Alcohol Coated Photonic Crystal Optical Fiber Sensor for Humidity measurement, *Sensors and Actuators B: Chemical*. 174, pp. 563–569, (2012).
81. Q. Wu, Y. Semenova, J. Mathew, P. Wang, and G. Farrell, Humidity sensor based on a single-mode hetero-core fiber structure, *Optics letters*, *36*(10), pp.1752-1754, (2011).
82. B. Gu, M. Yin, A. P. Zhang, J. Qian, and S. He, Optical fiber relative humidity sensor based on FBG incorporated thin-core fiber modal interferometer, *Optics express*, *19*(5), pp.4140-4146, (2011).
83. P. Wang, F. Gu, L. Zhang, and L. Tong, Polymer microfiber rings for high-sensitivity optical humidity sensing, *Applied Optics*, 50(31), pp.G7-G10, (2011).
84. Y. Wu, T. Zhang, Y. Rao, and Y. Gong, Miniature interferometric humidity sensors based on silica/polymer microfiber knot resonators, *Sensors and Actuators B: Chemical*, 155(1), pp.258-263, (2011).

85. L. H. Chen, C. C. Chan, T. Li, M. Shaillender, B. Neu, Balamurali, et al., Chitosan-coated polarization maintaining fiber-based Sagnac interferometer for relative humidity measurement, *Selected Topics in Quantum Electronics, IEEE Journal of*, 18(5), pp.1597-1604, (2012).
86. W. A. Gambling, D. N. Payne and H. Matsumura, Radiation from curved single mode fibers, *Electron. Lett*., 12, pp.567–569, (1976).
87. L. Lewis, D.C. Chang and E.F. Kuester, Electromagnetic waves and curved structures, *IEE Electromagnetic waves series*; 2, (1977).
88. Q. Wang, G. Farrell, T. Freir, G. Rajan, P. Wang, Low cost wavelength measurement based on macrobending singlemode fiber, *Opt. Lett*., 31, pp.1785-1787, (2006).
89. Q. Wang, G. Rajan, P. Wang,G. Farrell, Macrobending fiber loss filter, ratiometric wavelength measurement and application, *Meas. Sci. and Technol*., 18, pp.3082-3088, (2007).
90. P. Wang, G. Farrell, Q. Wang and G. Rajan, An Optimized Macrobending-Fiber-Based Edge Filter, *IEEE Photonics Technology Letters*, 19(15), pp. 1136-1138, (2007).
91. G. Rajan,Y. Semenova, G. Farrell, All-fiber temperature sensor based on macro-bend singlemode fiber loop, *Electron. Lett*., 44, pp.1123-1124, (2008).
92. P. Wang, Y. Semenova, Y. Li, Q. Wu, G. Farrell, A macrobending singlemode fiber refractive index sensor for low refractive index liquids, *Photonics Letters of Poland*, 2(2), pp. 67-69, (2010).
93. P. Wang, G. Brambilla, Y. Semenova, Q. Wu, G. Farrell, A simple ultrasensitive displacement sensor based on a high bend loss singlemode fiber and a ratiometric measurement system, *Journal of Optics*, 13, pp. 075402, (2011).

94. P. Wang, Y. Semenova, Q. Wu, G. Farrell, A fiber-optic voltage sensor based on a macrobending structure, *Optics & Laser Technology*, 43(5), pp. 922-925, (2011).

95. D. Marcuse, Curvature loss formula for optical fibers, *J. Opt. Soc. Amer*., 66, pp. 216-220, (1976).

96. A. J. Harris, and P. F. Castle, Bend Loss Measurements on High Numerical Aperture Single-Mode Fibers as a Function of Wavelength and Bend Radius, *J. Lightw. Technol.*, LT-4 (1), pp. 34–40, (1986).

97. F.M. Haran, K. Ono, J.S. Barton, and J.D.C Jones, Bend loss oscillations in single mode optical fiber: higher order re coupling, *Opt. Commun*., 108, pp. 55-59, (1994).

98. L. Faustini, and G. Martini, Bend loss in single-mode fibers, *J. Lightw. Technol*., 15(4), pp. 671–679, (1997).

99. S. H. Nam, and S. Yin, High-Temperature Sensing Using Whispering Gallery Mode Resonance in Bent Optical Fibers, *IEEE Photon. Technol. Lett*., 17 (11), pp. 2391-2393, (2005).

100. J. D. Love, and C. Durniak, Bend Loss, Tapering, and Cladding-Mode Coupling in Single-Mode Fibers, *IEEE Photonics Technol. Lett*., 19(16), pp. 1257-1259, (2007).

101. L. Yao, A. Birks, and J. C. Knight, Low bend loss in tightly-bend fibers through adiabatic bend transitions, *Optics Express*, 17(4), pp. 2962-2967, (2009).

102. H. F. Taylor, Bending Effects in Optical Fibers, *Journal of lightwave technology*, LT-2 (5), pp. 617-628, (1984).

103. J. D. Love, and C. Durniak, Bend Loss, Tapering, and Cladding-Mode Coupling in Single-Mode Fibers, *IEEE Photonics Technol Lett*, 19, (16), pp. 1257–1259, (2007).

104. L. Yao, A. Birks, and J. C. Knight, Low bend loss in tightly-bend fibers through adiabatic bend transitions, *Opt Express*, 17 (4), pp. 2962-2967, (2009).

105. J. Mathew, G. Rajan, Y. Semenova, and G. Farrell, All fiber tunable loss filter, *Proc. SPIE* 7503, pp.75037G-75037G-4, (2009).

106. J. C. Knight, T. A. Birks, P. S. J. Russell, D. M. Atkin, All-silica single-mode optical fiber with photonic crystal cladding, *Optics Letters*, 21(19), pp. 1547–1549, (1996).

107. J. C. Knight, Photonic crystal fibers, *Nature*, 424(6950), pp. 847–851, (2003).

108. P. Russell, Photonic crystal fibers, *Science*, 299(5605), pp. 358– 362, (2003).

109. P. Russell, Photonic-crystal fibers, *Journal of Lightwave Technology*, 24(12), pp. 4729–4749, (2006).

110. T. A. Birks, J. C. Knight, and P. St. J. Russell, Endlessly single-mode photonic crystal fiber, *Optics Letters*, 22(13), pp. 961-963, (1997).

111. J. C. Knight, T. A. Birks, R. F. Cregan, P. St. J. Russell, and J. P. De Sandro, Large mode area photonic crystal fiber, *Electronics Letters*, 34(13), pp. 1347-1348, (1998).

112. G. Renversez, B. Kuhlmey, and R. McPhedran, Dispersion management with microstructured optical fibers: ultraflattened chromatic dispersion with low losses, *Optics Letters*, 28(12), pp. 989-991, (2003).

113. C. L. Zhao, X. Yang, C. Lu, W. Jin, and M. S. Demokan, Temperature-insensitive interferometer using a highly birefringent photonic crystal fiber loop mirror, *IEEE Photonics Technology Letters*, 16(11), pp. 2535–2357, (2004).

114. J. H. Lim, H. S. Jang, K. S. Lee, J. C. Kim, and B. H. Lee, Mach–Zehnder interferometer formed in a photonic crystal fiber based on a pair of long-period fiber gratings, *Optics Letters*, 29(4), pp. 346–348, (2004).

115. D. Monzón-Hernández, V. P. Minkovich, J. Villatoro, M. P. Kreuzer, and G. Badenes, Photonic crystal fiber microtaper supporting two selective higher-order modes with high sensitivity to gas molecules, *Applied Physics Letters*, 93(8), pp. 081106, (2008).

116. H.Y. Choi, M. J. Kim, and B. H. Lee, All-fiber Mach-Zehnder type interferometers formed in photonic crystal fiber, *Optics Express*, 15(9), pp. 5711–5720, (2007).

117. J. Villatoro, V. P. Minkovich, V. Pruneri, and G. Badenes, Simple all-microstructured-optical-fiber interferometer built via fusion splicing, *Optics Express*, 15(4), pp. 1491–1496, (2007).

118. J. Villatoro, V. Finazzi, V. P. Minkovich, V. Pruneri, and G. Badenes, Temperature-insensitive photonic crystal fiber interferometer for absolute strain sensing, *Applied Physics Letters*, 91(9), pp. 091109, (2007).

119. R. Jha, J. Villatoro, and G. Badenes, Ultrastable in reflection photonic crystal fiber modal interferometer for accurate refractive index sensing, *Applied Physics Letters*, 93(19), pp. 191106, (2008).

CHAPTER 2. RELATIVE HUMIDITY SENSOR BASED ON A FIBER BEND

2.1. Introduction

Most fiber optic humidity sensors work on the basis of a hygroscopic material coated over the optical fiber to modulate the light propagating through the fiber [1]. The available fiber optic humidity sensors require complex processing of the fiber to allow the light to interact with the water vapor, such as fabrication of gratings [2,3], cladding removal [4-6], side polishing [7,8], tapering [9, 10], formation of a fiber Fabry-Perot cavity [11], or a hetero structure [12]. The use of a simple bent optical fiber has been previously demonstrated by D. C. Bownass et al [13] for the detection of the gross humidity state (dry or humid) in telecommunications networks using a bent standard single mode fiber coated with a hygroscopic material. A bend loss based humidity sensor is attractive because the fabrication of the sensor head does not require special treatment of the fiber itself. In the paper by D.C. Bownass et al, conventional low bend loss SMF fiber is used which results in low sensitivity, also the selection of a suitable coating to maximise the sensitivity and range of operation was also not considered.

In this chapter we present a detailed study of such a bend loss based sensor with a focus on significantly improving the sensitivity and operating range. In our study we observe that in a buffer-stripped bent single mode fiber, due to the coupling of the fundamental mode to cladding modes, resonant peaks will occur in the transmission response. This response is oscillatory with respect to the bend radius and wavelength and also varies with ambient refractive index. If the surrounding refractive index of the bend fiber is changed, it will lead to a change in the coupling conditions and results in a shift in the wavelength of the resonant peaks. In order to achieve improved sensitivity for the

humidity sensor we used a high bend loss fiber (1060XP). We characterised the spectral response of this bent fiber as a function of surrounding refractive index (RI) to establish the effect of wavelength on the sensitivity of the sensor. An additional advantage of using a high bend loss fiber is that the sensor bend radius can be much larger than the 6 mm used by Bownass et al [13] with standard SMF, resulting in a much lower probability of stress-induced breakage of the fiber.

2.2. Operating principle of the sensor

When an uncoated fiber is bent the effective refractive index profile is changed [15-17]. Light propagating on the outside of the bend has further to travel and this effect can be modelled as a tilt applied to the refractive index profile of the fiber [17], given as:

$$n(x) = n_0(x)[1+(1+\gamma)x/R] \tag{2.1}$$

where $n_0(x)$ is the refractive index profile when the fiber is straight, R is the bend radius, x is a transverse coordinate along a line joining the centre of curvature and the centre of the fiber, with the origin in the centre of the fiber and with x increasing in a positive fashion toward the fiber outer surface (Fig. 2.1). The factor $\gamma = -0.22$ for silica fiber [17] accounts for the strain-optic effect. According to coupled mode theory the fundamental core-guided mode can couple with a cladding mode with a peak intensity at the outer rim of the fiber bend [15, 16], which propagates along the fiber bend as a Whispering Gallery mode. With increasing bend curvature the refractive index profile of the bend fiber becomes more tilted and the effective index for the cladding modes increases, reaching a maximum at the outer edge. At some critical bend radius, the effective index of the cladding modes equals the effective index for the core-guided mode. If there is sufficient overlap between the core mode and a cladding mode at this point, the core mode and a cladding mode will be coupled together. At tighter bends the core mode will

couple to other cladding modes. In the straight portion of the fiber following the bend region, the conventional fiber buffer coating suppresses the cladding modes so that the power coupled to the cladding mode is absorbed and is not re-coupled to the core mode. Therefore at certain bend radii and wavelengths, there are dips in the transmission spectrum of the macro bend fiber that are a function of the degree of coupling of the fundamental mode to the cladding modes [14]. The phase matching condition for mode coupling also depends on the ambient refractive index at the bend. If the surrounding refractive index of the bent fiber is changed, this will lead to a change in the coupling conditions and will result in a shift in the resonant wavelength. To utilise such a bent fiber as a humidity sensor the buffer-stripped fiber bend can be coated with a hygroscopic material, whose refractive index changes with respect to the ambient humidity.

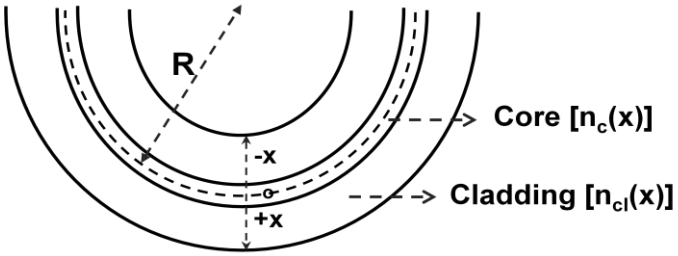

Fig. 2.1. Schematic diagram of a fiber macro-bend

In practice the simplest mechanical configuration for such a sensor is a simple fiber bend where the number of turns is less than one. Because of the low bend sensitivity of standard fiber such as SMF28, a sensor fabricated from such a fiber will need to utilise very low values of bend radius ~6 mm [13] to achieve a reasonable sensitivity, increasing the risk of stress-induced fiber breakage. To improve sensitivity and increase the bend radius so as to reduce the risk of fiber breakage, a high bend loss fiber such as 1060XP is much more suitable.

2.3. Experimental RI characterisation of the fiber bend

Initially an experimental characterisation of the fiber bend was carried out to enable the selection of a suitable polymer coating for humidity sensing. The fiber used in the experiment was a 1060XP singlemode fiber, a high bend loss fiber that allows for the fabrication of a compact sensor head. Since it is known that suitable humidity sensitive coating materials usually have RI values that range from below the fiber cladding RI (1.456) to above the cladding RI, it was important in this experimental study to characterize the spectral response of a bent fiber surrounded by materials with RI values in the range around 1.456. For this purpose a 35 mm length of the buffer coating was stripped from the middle section of a longer length of the fiber and the fiber was fixed on to a semi circular rod of outer diameter of 30 mm forming a bend angle (θ) of about 133^0. We selected this bend radius and bend angle experimentally as it was found that this is the highest bend radius and smallest bend angle that results in strong resonant dips in the measurable wavelength range of our experiment. A high bend radius is desirable in order to minimise the risk of fiber breakage. Light from a Super Luminescent Diode was launched in to the fiber from the input side of the bend and the output from the bend was connected to an Optical Spectrum Analyser. The transmission response of this bent fiber was studied by immersing it in different RI solutions prepared by precisely mixing Dimethyl sulfoxide (DMSO) and water with different volume concentrations. The RI of the prepared solutions is obtained from an Abbe refractometer.

The transmission responses of the bent fiber for different ambient RIs are shown in Fig. 2.2 for the measurable wavelength range in our experiment. For ambient RIs below the value of the refractive index of the fiber cladding, resonant dips are observed in the

transmission response. As shown in Fig. 2.3, when the RI increases the resonant wavelength shifts to a shorter wavelength.

When the surrounding RI matches or exceeds the RI of the fiber cladding the loss dips disappear from the transmission spectrum; the surrounding liquid acts as an infinite cladding, effectively absorbing the leaky modes. In this range of ambient RIs, resonant peaks are suppressed and the transmission loss increases monotonically with wavelength and the ambient RI as expected.

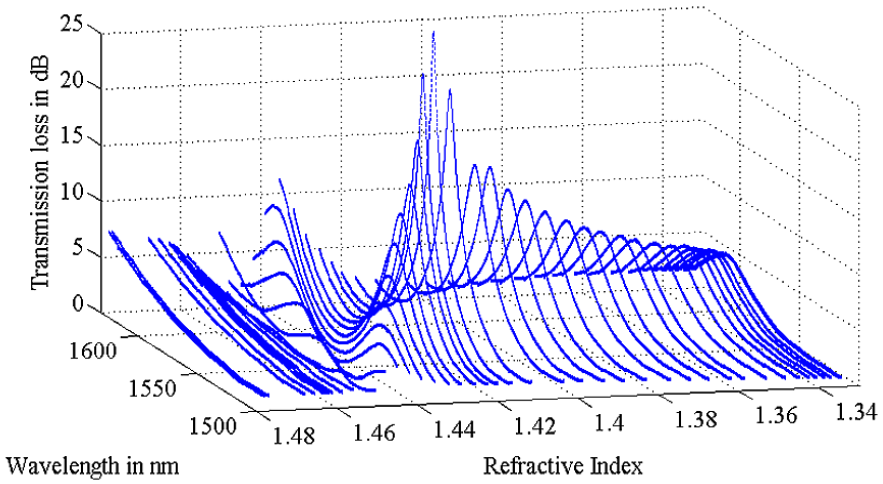

Fig. 2.2. Transmission response of the bent fiber for different ambient refractive indices.

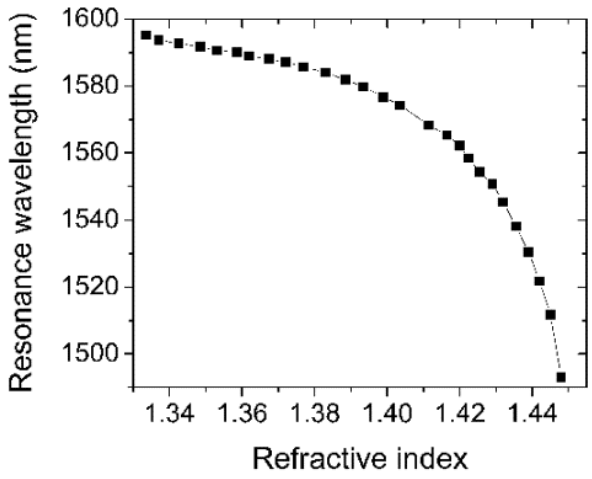

Fig. 2.3. Resonance wavelength shift as a function of the ambient refractive index.

The study of the ambient refractive index of a fiber bend suggests that it is sentive to RI values in the range 1.33 – 1.48. Therefore it is possible to use this structure for humidity sensing by coating its surface with a hygroscopic material whose RI changes with respect to RH and where the RI of this hygroscopic material is in the range 1.33-1.48. Since Polyethylene oxide has a reported RI value in this range [13], initially it is selected for RH sensing using a fiber bend.

2.4. Relative humidity sensor based on Polyethylene oxide coated fiber bend.

As a confirmation of the suitability of using a high bend loss fiber bend as a sensitive humidity sensor, a sensor using a 1060XP fiber bend coated with polyethylene oxide (PEO) is implemented and studied. The utilisation of a simple ratiometric power measurement scheme for interrogation is demonstrated and also the optimum operating wavelength to maximise sensitivity using such a scheme is determined. The sensor offers a competitive humidity sensitivity utilising a cost effective ratiometric power measurement system. The response of the humidity sensor is found to be reversible and repeatable. Finally, we also study for the first time the time response of such a sensor and we show that the response to a humidity change is very fast by comparison with existing electronic sensors.

2.4.1. Experimental results and discussion

To utilise this structure as a humidity sensor the buffer-stripped fiber bend was coated with a hygroscopic material, whose refractive index depends on the ambient humidity. A humidity sensitive polymer, polyethylene oxide (PEO), was chosen as a polymer coating with a refractive index in the range 1.4-1.5 with respect to humidity [13]. Such a range of RIs makes it a potential choice for a coating for a single mode fiber bend sensor, given the refractive index of silica. The refractive index of the PEO decreases

with increasing humidity and this change is reversible. PEO also has the advantage that it can be easily coated on to the fiber due to its high adhesion with silica [2].

The sensor head is fabricated by dip coating the buffer-striped portion of the 1060XP fiber in a PEO solution prepared by dissolving 6 wt% PEO (Sigma-Aldrich) in distilled water. No thickness control is used, since the function of the coating is simply to act as a variable refractive index layer. The coated fiber is kept for one day at room temperature until it is partially dehydrated and reaches equilibrium with the ambient room humidity. To make it mechanically stable the probe is then fixed on to a semi-circular rod of outer diameter 30 cm forming a bend of about 133^0. Since the fiber is bent after the coating was applied there is a chance of inducing a small strain in the bulk of the coating. While this is not investigated here it is suggested that taking an SEM image of the coated fiber before and after bending is likely to provide a more comprehensive insight in to the uniformity of the coating or its micro-structure and the changes that occur as a result of bending. A schematic diagram of a PEO coated fiber bend is shown in Fig. 2.4.

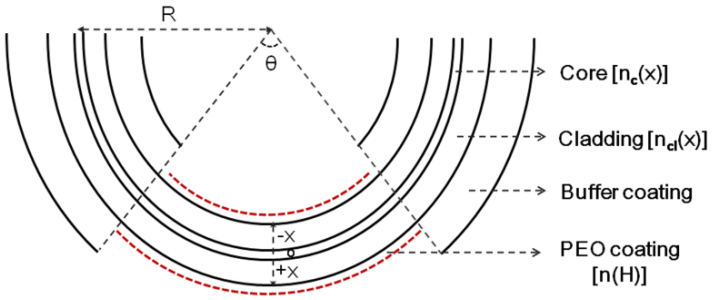

Fig. 2.4. Poly(ethylene oxide) coated fiber bend.

The humidity response of the fabricated sensor head is studied at room temperature and normal atmospheric pressure by placing the sensing element in a customised climate chamber shown in the Fig. 2.5. It consists of a sealed acrylic chamber with a dry/wet

air flow system that can vary the internal humidity in the chamber. A calibrated electronic humidity sensor (model: 11-661-21, make: Control company) is used for monitoring the temperature and humidity inside the chamber.

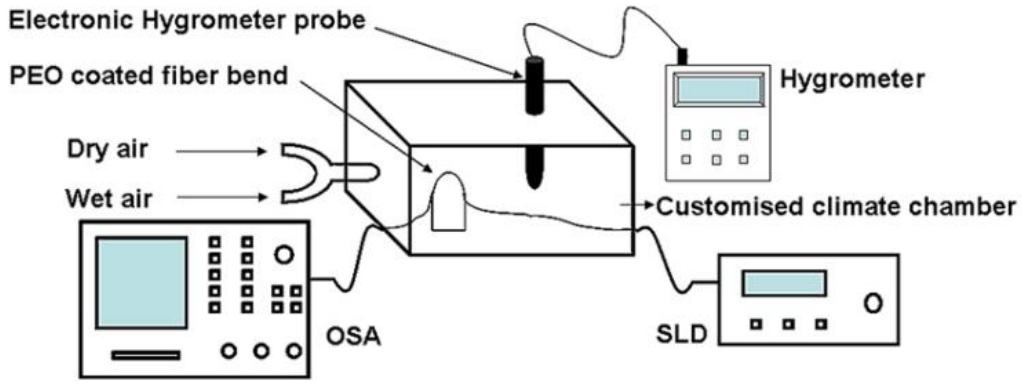

Fig. 2.5. Experimental setup for studying the humidity response of the PEO coated fiber bend.

We have observed the transmission response of the PEO coated fiber bend for a range of humidity values from 30% RH to 95% RH. No resonant dips were observed in the transmission spectrum for ambient humidity values below 85% RH, which is shown in Fig. 2.6. As concluded from the results in Fig. 2.2 and their discussion, this is due to the fact that the RI of the coated PEO film is above the RI of the fiber cladding and therefore the PEO coating is acting as an absorption coating. As surrounding humidity value increases above 85% RH resonant dips appear in the transmission spectrum. The appearance of these loss dips in the transmission spectrum in a PEO coated fiber bend is due to resonant mode coupling at particular RI values as shown in Fig. 2.7. (It should be noted that the blue shift of the curves shown in Fig. 2.7 is probably an anomaly because the total RH range shown in the figure is < 2.5% RH and the accuracy of the climate chamber is ±2% RH). The reason for these resonant dips is that around this humidity value PEO undergoes a physical phase change from a semi-crystalline structure to a gel

with a large decrease in its index of refraction to a value below the RI of the fiber cladding and as we have shown in Fig. 2.2 this will result in resonant dips in the transmission spectrum as the surrounding RI of the fiber bend is below the cladding RI. At higher humidity values, the RI of PEO is below the refractive index of the fiber cladding (1.456) and the resonant wavelength shifts to a higher wavelength with respect to humidity as shown in Fig. 2.8 and as predicted by our experimental RI characterisation of the fiber bend in Fig. 2.2.

The variation in the RI of the PEO layer modulates the intensity of the light propagating through a fiber bend with respect to ambient humidity. From Fig 2.7 it is observed that at 85% relative humidity the refractive index of the PEO layer is just above the cladding refractive index of the fiber and the loss will be higher at higher wavelengths. At 87% RH the PEO layer RI value is below the cladding RI and mode coupling takes place and hence resonant dips appear in the transmission spectrum at around 1550 nm. Furthermore it is observed that between RH values from 85% to 87.35% a large power variation occurs in the transmission loss over the wavelength range from 1590 to 1630 nm. While it is possible to utilise an OSA to determine the shift in the resonant dip wavelength in this RH range in order to monitor RH, the large power variation in the 1590-1630 nm range suggests a much simpler, more economic, approach to interrogating the sensor based on power measurement. To demonstrate the feasibility of this an experimental setup was developed based on a ratiometric power measurement scheme, with a tunable laser at fixed wavelength as a source. A ratiometric scheme is used to avoid errors induced by fluctuations in the optical source power, resulting in more stable and accurate results. Experimentally it is found that the optimum wavelength that offers the highest RH sensitivity using this interrogation scheme is 1620 nm. The tunable source was therefore set to 1620 nm for this experiment.

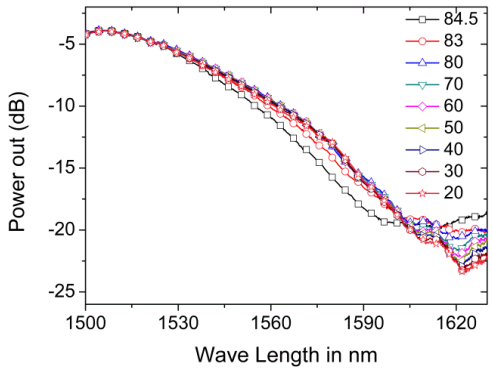

Fig. 2.6. Humidity response of the PEO coated fiber bend for RH below 85%.

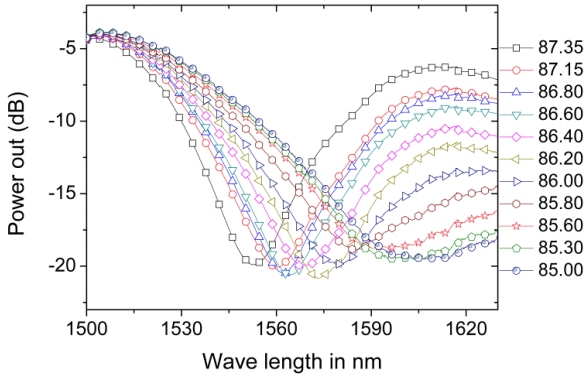

Fig. 2.7. Appearance of loss dips in the transmission spectrum in a PEO coated fiber bend at RH above 85% due to resonant mode coupling at particular RI values of the coating.

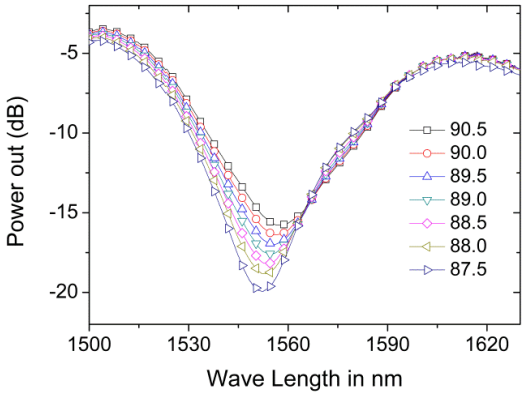

Fig. 2.8. Resonant wavelength shifts to higher wavelengths with the increase of humidity.

The input signal from the fixed wavelength tunable source using a 50:50 coupler is split into two equal power signals, one goes to the fiber sensor bend and the other is the reference signal. Two photodiodes with associated electronics and data logging are used to measure the power at the outputs of the corresponding arms. By measuring the power ratio of the two signals the transmission loss of the PEO coated fiber bend can be obtained. The output power variation of the PEO coated fiber bend is shown in Fig. 2.9. The two curves represent the measurements taken with a time gap of one week, which shows the good repeatability and long term mechanical stability of the sensor head. A large power variation of approximately 20 dB is observed above 85% RH so that the sensor as expected behaves as a humidity dependant optical switch. The developed PEO coated bent single mode fiber based humidity sensor can be applied to monitor changes in humidity in the range from 80 to 95% with a very high sensitivity.

To estimate the response time of the sensor, the coated fiber was exposed to an environment with rapid changes of the RH. First the RH in the chamber was maintained at 70% RH and then the cover of the chamber was removed quickly in order to rapidly expose the sensor to a measured environmental RH of 90%. The measured time-dependant response of the sensor is shown in Fig. 2.10. The sensor has a very fast response to humidity variations and the estimated response time (from 10% to 90% of the signal maximum) from the Fig. 2.10 is circa 780 milliseconds when the RH changes from 70% to 90%. In this study the effect of coating thickness on the response time is not considered, but it is expected that a thinner coating could yield a faster response.

The experimental results presented in this work suggest a practical motivation to investigate inexpensive and disposable PEO-based fiber optic sensors with a simple fabrication technique and fast response for relative humidity control. For example, relative humidity above 85% must be maintained in food refrigerators to protect

vegetables and fruit against rotting and to preserve their freshness for an extended time period.

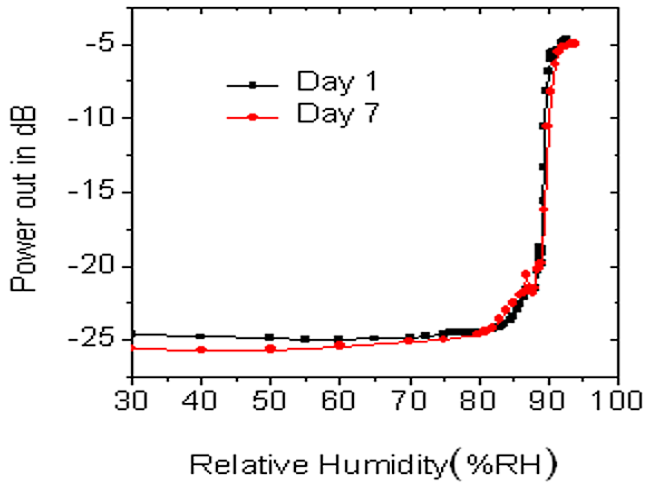

Fig. 2.9. Humidity response of the PEO coated fiber bend.

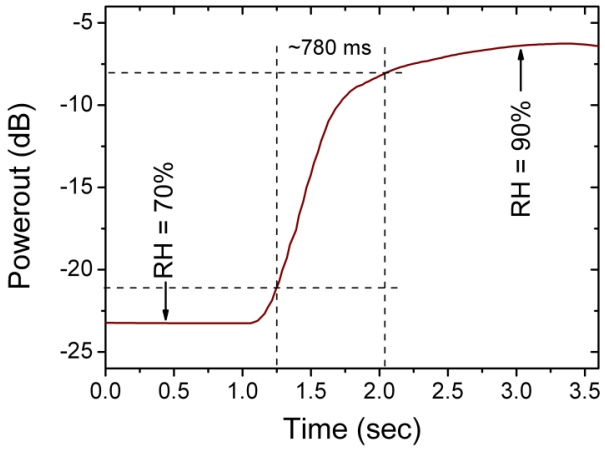

Fig. 2.10. Time response of the fiber-bend based humidity sensor.

The demonstrated sensor behaves as a humidity dependant optical switch in this region of RH values with a large power variation of about 20 dB at around 85% RH. Because of this large power variation at around 85% RH and since we know the normal room humidity is below 85% RH and the relative humidity of the human breath is above 90% RH it can also be used as a human breath rate monitor. To prove the feasibility of using

it as a breath rate monitor we placed the PEO coated fiber bend at a distance of about 2 cm from the tip of a volunteer's nose and the resulting breath RH response of the sensor is as shown in Fig. 2.11, for a time span of 60 seconds. This result also confirms the fast recovery and repeatability of the sensor. A fiber optic humidity sensor is suitable as a breathing monitor for patients during a magnetic resonance imaging (MRI) scan because of its immunity to magnetic field interference. Additionally given that humidity is being monitored using an intensity variation, there is the possibility of utilising an optical time domain reflectometer (OTDR) based interrogation scheme to allow for multiplexing of several sensors along a single fiber for distributed RH sensing but the number of sensors that could be multiplexed is limited by the optical power budget of the sensor system.

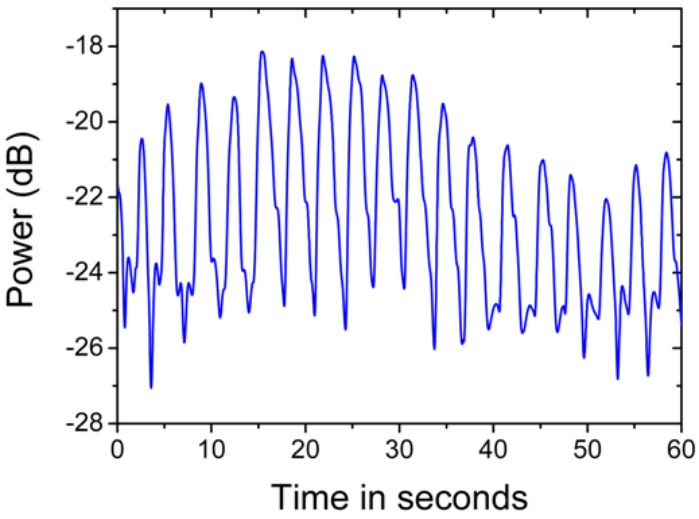

Fig. 2.11. Continuous human breath response of the PEO coated fiber bend based sensor.

In this section of the chapter a highly sensitive all-fiber humidity sensor based on power measurement at an optimised wavelength and bend radius is demonstrated. The sensor behaves as a humidity dependant optical switch between 85% and 90% RH and its

response is fast and reversible in nature. The sensor also offers the advantages of simple structure and low cost. Since the demonstrated fiber bend responds to refractive index variation the same configuration can be used for sensing humidity in various RH ranges if different suitable hydrophilic polymers are used as coatings.

2.5. Relative humidity sensor based on an Agarose coated fiber bend

Even though the humidity sensor based on a polyethylene oxide (PEO) coated fiber bend demonstrated in the above section showed significantly improved RH sensitivity, due to the limitation of the coating material, the sensor behaved as a humidity dependent optical switch, operating between 85% and 90% RH and thus showed only a narrow range of operation, but with a high sensitivity.

In this section a detailed study of such a bend loss based humidity sensor is presented with the objective of achieving a significantly improved operating range and linearity. The selection of a suitable hygroscopic coating and also the influence of bend radius on sensor performance are investigated. The sensor demonstrated in this section shows for the first time, a wide linear response using a fiber bend instead of the narrow range operation showed above. The measured response time of the sensor is about 50 ms, which is faster compared to other fiber optic humidity sensors. We show that the humidity sensitivity of the sensor is wavelength dependent and that higher sensitivity is observed at higher wavelengths. The response of the demonstrated humidity sensor also showed good reversibility.

2.5.1. Selection of a suitable coating

A suitable coating for this sensor must satisfy a number of criteria. Firstly it should be hygroscopic and should have a suitable RI change with respect to ambient humidity.

Another important requirement is that the preparation of the coating solution and the coating process should be simple. The material should also possess a good adhesion to silica and finally the coating material should have a low evaporation tendency at higher humidity and should exhibit good long term stability.

There are a number of possible hygroscopic coating materials. Sol-gel silica offers a wide humidity operating range but the preparation and coating process for this material is difficult and there is a tendency for cracks to develop in the coating reducing the uniformity of the coating and thus compromising the operation of the sensor. Polyvinyl alcohol (PVA) dissolves in water and offers a simple coating procedure but it is not suitable for sensing in a wide humidity range. The reason is that the PVA film dries completely when it reaches a RH value of ~50% so that a subsequent decrease in the environmental humidity has no effect on the coating. PEO is a possible candidate and is highly sensitive but we have already shown above that PEO does not provide a linear response and because PEO is soluble in water, long term exposure to high humidity levels is likely to damage the coating. The materials Agarose and Gelatin are potential candidates; both offer a wide operating humidity range with a simple coating procedure. However compared to Gelatine, Agarose is a more consistent product with fewer impurities and less ethical concerns. It has a higher melting point than the Gelatin and also is a more stable material with respect to temperature. Agarose shows a linear change in its RI with respect to humidity [18]. Agarose is an unbranched polysaccharide obtained from the cell walls of some species of red algae or seaweed. Chemically, Agarose is a polymer made up of subunits of the sugar galactose. Agarose has an added advantage of low material degradation compared with the materials used in [13]. Since Agarose is soluble in hot water [4, 6] the preparation and coating procedures are simple. Agarose also has a good adhesion to silica and easily forms a thin coating film on silica

fiber. All these factors make it a suitable choice as a coating for the fiber optic humidity sensor considered here.

2.5.2. Experimental results and discussion

To investigate the humidity response of the fiber bend the buffer stripped fiber bend was coated with Agarose. The sensor head is fabricated by coating the buffer stripped portion of the 1060XP fiber with hot (>35 ^{O}C) Agarose solution. The solution is prepared by dissolving 1.5 wt% Agarose in distilled water. To dissolve the Agarose in distilled water the beaker containing the mixture is placed on a heater combined with a magnetic stirrer. The temperature of the heater is set to 65 ^{O}C and at the same time the mixture of Agarose and water inside the beaker is stirred until the Agarose is completely dissolved. After this, if the mixture is cooled, the gel polymerizes and once the gelling point is reached (~35 ^{O}C) the mixture assumes its hydrogel form and will not be liquid again until is heated and reaches its melting point. For these reasons, the Agarose mixture has to be deposited on the optical fiber when the temperature of the solution is above the gelling point, that is, when the mixture has not gellified yet, and is still in liquid form. In order to undertake this process the fiber is fixed straight and horizontally above a translation stage. Below the fiber a heater is fixed on a translation stage. A small container placed at the top of the heater is filled with hot Agarose solution, forming a hemispherical dome of solution projecting outside on the top of this container. The position of this container can be adjusted to pass the fiber through the projected solution. The temperature of the heater is set at 65 ^{O}C. The fiber is drawn through the hot Agarose solution using the translation stage which is software controlled using a computer. This arrangement allows for good repeatability of the coating parameters and by varying the drawing speed of the fiber through the solution the coating layer thickness can be varied. The coated fiber is kept for one day at room

temperature until it is partially dehydrated and reaches the equilibrium with the ambient environment.

The fiber with Agarose coating is fixed between a stable and translating surface as shown in Fig. 2.12. This arrangement allows for an accurate control of the bend radius of the fiber bend. The humidity response of the Agarose coated fiber bend (ACFB) is studied at room temperature (22±0.5 ^{O}C) and normal atmospheric pressure by placing the sensing element in a controlled environment chamber (Electro Tech Systems inc., Model 5503-00 with Package F). Initially the transmission response or the insertion loss at different wavelengths of the ACFB is observed for different bend radii by connecting one end of the ACFB to a broad band source, a super luminescent diode (SLD) with an optical bandwidth of 54.5 nm and a center wavelength of 1544.5 nm (COVEGA Corporation, SLD 6593), and to an optical spectrum analyser (OSA) at the other end. To achieve a linear wide range of operation for an ACFB, apart from selecting a material with a linear RI change with respect to humidity, it is also important to select a bend radius such that there is no resonant dip in the transmission spectrum. Even though the RI of the Agarose is greater than the RI of the fiber cladding the effective refractive index of the coating will be less because its thickness is very small (~1 μm) so at a certain bend radius and operating wavelengths the power coupling from the fundamental core mode to the cladding mode will be high (resonant mode coupling at phase matched condition) [14]. In the case of the PEO coated fiber bend demonstrated above, the selected bend radius of 15 mm gives resonant dips in the 1500-1600 nm wavelength range when the RI of the coating is less than the RI of the fiber cladding (1.456). Also a dominant decrease in the RI of the PEO coating occurs at ~85% RH which brings the coating RI < 1.456 at this RH value. This results in the appearance of the resonant dip at ~85% RH, therefore its humidity reponse is non linear and shows a

switch like RH response. This work is focussing on achieving a wide linear RH response for the sensor; hence the appearance of a resonance dip in the wavelength range of interest must be avoided for a wide RH range.Therefore to achieve a linear spectral response in the range 1500-1600 nm we need to select some bend radii for which there are no resonant dips in the spectral range of interest. We have observed that there are no resonant dips in the transmission spectrum of the ACFB with bend radii circa 13.2 mm and 16.7 mm. The transmission responses of the ACFB with measured bend radii of 13.25 mm and 16.75 mm show relatively flat responses at an ambient humidity of 40% RH as shown in Fig. 2.13. As expected when the bend radius decreases the loss increases for the ACFB.

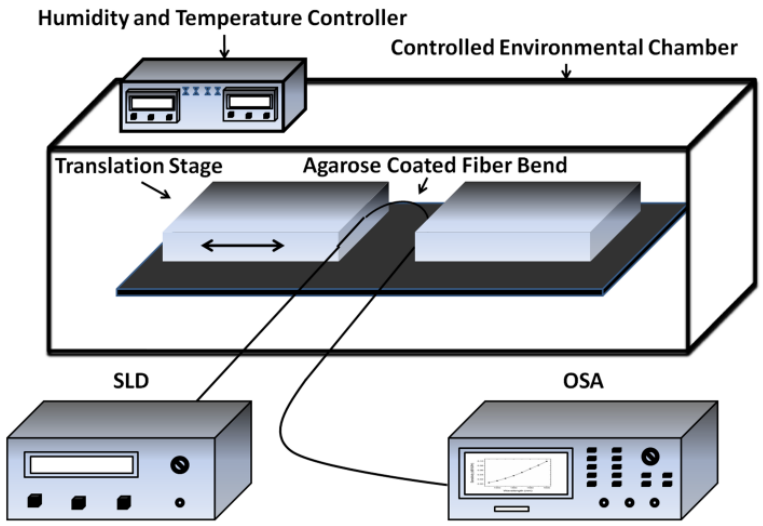

Fig. 2.12. Experimental arrangement to study the humidity response of the Agarose coated fiber bend.

We have also studied the transmission response of the ACFB at these bend radii for varying RH values and observed that the larger bend radius offers an improved linearity and a wide RH range, therefore a bend radius of 16.75 mm is selected for further study. As an additional benefit, such a relatively high bend radius selected in our experiment results in a much lower probability of stress-induced breakage of the fiber. The

transmission response of the ACFB with a bend radius of 16.75 mm and for a range of humidity values from 25% to 90% RH is shown in Fig. 2.14. No resonant dips were observed in the transmission spectrum for ambient humidity values below 90% RH.

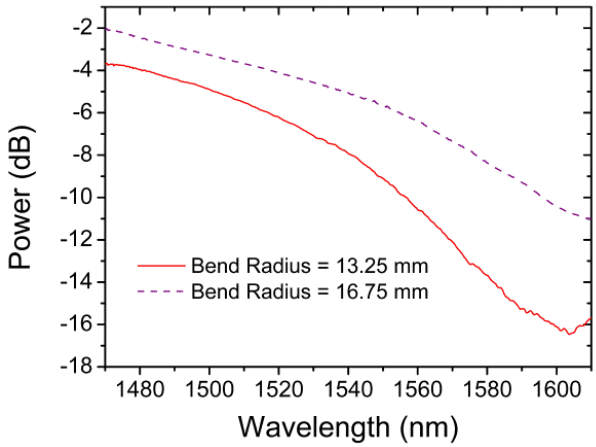

Fig. 2.13. Transmission response of the ACFB with bend radii 13.25 mm and 16.75 mm and at an ambient humidity 40% RH.

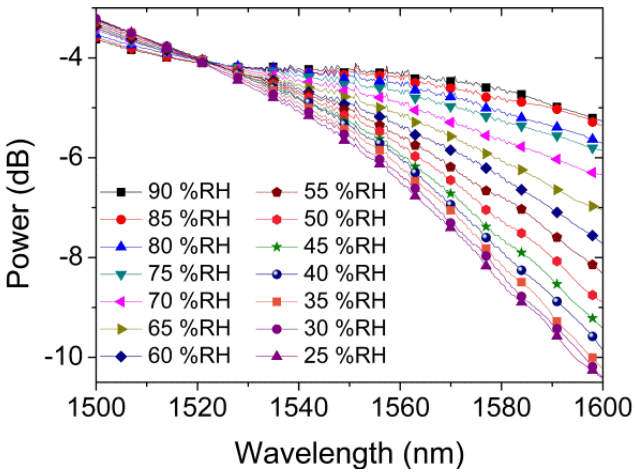

Fig. 2.14. Transmission response of the ACFB at different ambient humidity values.

In our experiment it is observed that the sensitivity of the ACFB to humidity changes is different at different wavelengths. The variation in insertion loss with respect to humidity is high at higher wavelengths. There is a large insertion loss variation of more than 5 dB at 1600 nm for a change in humidity of 65% RH. But for this same humidity

change the insertion loss variation at 1520 nm is negligibly small. The insertion loss variation with respect to humidity at different wavelengths for a humidity range of 25-90% RH is shown in Fig. 2.15. The insertion loss variation increases monotonically as the wavelength increases and it is observed that the humidity response of the ACFB is linear in the wide humidity range of 25-90% RH for the wavelengths from 1530 nm to 1560 nm and for wavelengths above 1560 nm this linear range decreases as the wavelength increases to 1600 nm. The average humidity sensitivity of the ACFB with respect to wavelength is shown in Fig. 2.16. The sensitivity increases as the wavelength increases from 1530 nm to 1600 nm.

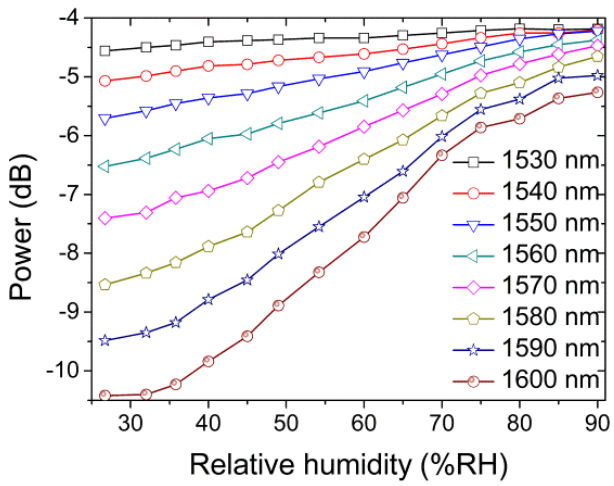

Fig. 2.15. The insertion loss variation with respect to humidity in the ACFB at different wavelengths.

When the surrounding humidity value increases above 90% RH resonant dips appear in the transmission spectrum. The appearance of these loss dips in the transmission spectrum in an Agarose coated fiber bend is due to resonant mode coupling at particular RI values. A resonant dip in the insertion loss at an ambient humidity 95% RH is shown in the Fig. 2.17. The study reveals that by selecting a suitable wavelength for interrogation it is possible to monitor the change in humidity at levels above 90 % RH

with good sensitivity. In the case of a wavelength of 1520 nm there is very little change in insertion loss up to an ambient humidity of 90% RH but above this humidity due to the appearance of loss dips, a large change in the insertion loss is observed. Thus by using a dual wavelength interrogation technique, with one wavelength for operation at or below 90% RH and a second wavelength for RH values above 90%, the range of operation of the ACFB might be extended to higher humidity values while maintaining good sensitivity.

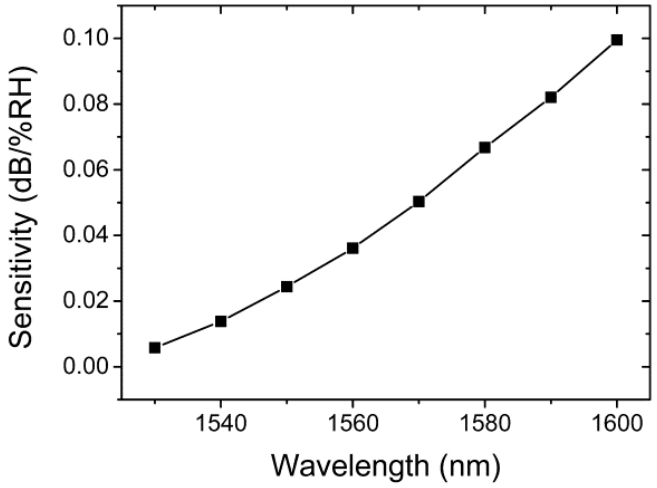

Fig. 2.16. The humidity sensitivity of the ACFB with respect to wavelength.

To study the repeatability of the ACFB performance as a humidity sensor, a tunable laser output is applied to the input of the sensor and the sensor output is connected to an optical power meter. The sensor response is observed for a humidity cycling from 60% RH to 80% RH and is shown in Fig. 2.18. Here the insertion loss is observed at the highest sensitivity wavelength, 1600 nm. At each humidity value the sensor response is observed for about 10 minutes and this humidity cycling is repeated a number of times. The response shows that the insertion loss exactly retraces the initial values in each cycle. This shows the good reversibility of the ACFB. The small variation in the insertion loss at each set humidity value is due to the fact that the climate chamber

requires some settling time to achieve a constant humidity value. During this time it produces damping oscillations in the humidity value, so corresponding damping oscillations are observed for the insertion loss also, with an amplitude <0.1 dB. Such an amplitude is relatively small compared to the large power variation of >2dB obtained for the humidity cycling with a ΔRH of 20%.

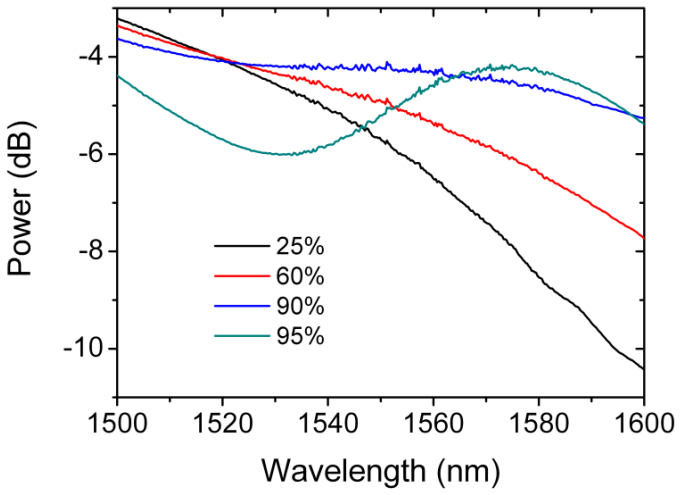

Fig. 2.17. Transmission response of the ACFB at humidity values above and below 90% RH, shows a loss dip at 95% RH

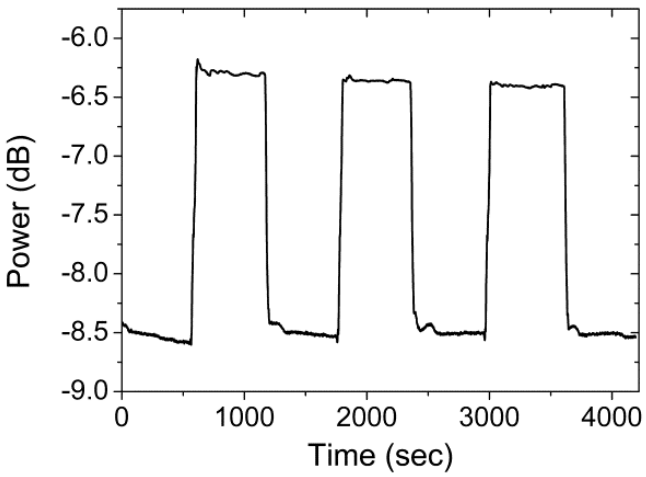

Fig. 2.18. Humidity cycling (60-80% RH) response to show the repeatability and stability of the ACFB.

The temperature dependence of the ACFB is observed by setting the ambient relative humidity value at 60% RH and is shown in Fig. 2.19. Since both propagation in the fiber bend [19] and the Agarose layer are temperature dependent the result observed is a combined effect of both dependencies. An insertion loss change of ±0.5 dB is observed for a temperature variation of 14 ^{O}C. The error bars shown in Fig. 2.19 are calculated from the data obtained from four experimental measurements taken for the temperature dependence of the ACFB.

A change of humidity inside the environment chamber from an initial value to a final value and back requires several minutes. The response time of ACFB sensor itself is observed to be much faster. Such a slow rate of RH change using the chamber is not suitable means for studying the response time of the sensor. Instead we applied a step change in humidity to the ACFB by directing a 0.5 s long breath exhale to the sensor; the resultant time dependent response is shown in Fig. 2.20. The ambient humidity during the study was 60% RH and the temperature 20 ^{O}C. The estimated response time (base line to 90% signal saturation) of the sensor is about 50 ms, when RH jumps from 60 to >90%. The recovery time of a humidity sensor depends on how fast the water vapor is removed from the sensor which is proportional to the air flow surrounding the sensor. The estimated recovery time (90% signal saturation to 20% baseline) of the sensor is 700 ms, which decreases if a flow of dry air surrounds the sensor.

The results show that the sensor has a fast, linear, wide reversible response with respect to humidity. The experimental results presented in this section suggest a practical motivation to investigate inexpensive and disposable Agarose-based fiber optic sensors with a simple fabrication technique for relative humidity control. The fast response time of the sensor also suggests that the sensor can potentially be used as a human breath rate monitor in a clinical situation. For example a fiber optic humidity sensor is suitable as a

breathing monitor for patients during an MRI scan because of its immunity to magnetic field interference.

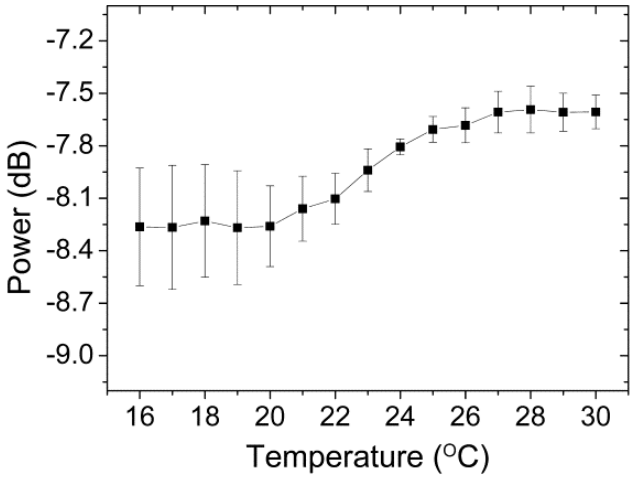

Fig. 2.19. Temperature dependence of the ACFB at an ambient humidity of 60% RH.

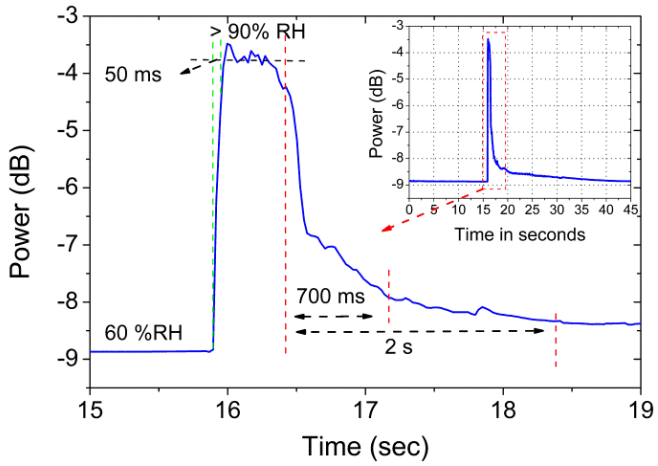

Fig. 2.20. Time response of the ACFB obtained by applying a step change of humidity.

2.6. Limitations of the fiber bend based humidity sensor

The optical transmission of a fiber bend depends on the bend radius and the wavelength of the propagating light. In practice there exists a difficulty in reproducing the exact bend radius of the fiber bend. Hence the fabrication repeatability of the humidity sensor based on fiber bend is also difficult. Furthermore, the mechanical stability of the fiber

bend based RH sensor is poor and airflow or a strong acoustic noise or some displacement to the fiber bend could result in erroneous measurement of RH. The optical transmission level of the fiber bend itself is temperature dependant so temperature compensation is required for the fiber bend based humidity sensor. It is also recognised that a limitation of a fiber bend based humidity sensor is that the sensor size is limited to the diameter of the bend. A small fiber bend will cause the stress induced breakage of the sensor head. Because of all these limitations alternative RH sensors based on a photonic crystal fiber interferometer are investigated in the following chapters.

2.7. Summary

In this chapter a detailed study of two disposable all-fiber humidity sensors based on a fiber bend are presented. The first sensor is a fiber bend coated with polyethylene oxide and the second one is a fiber bend coated with Agarose. A high bend loss fiber (1060XP) is utilised in this study to enhance the sensitivity of the sensors while keeping the bend radius of the sensors large to avoid the stress induced breakage of the fiber. The fundamental details of light propagation in a bent fiber are discussed. The spectral response of this bent fiber as a function of surrounding refractive index (RI) is characterised to enable the selection of a suitable polymer coating for humidity sensing and to establish the effect of wavelength on the sensitivity of the sensor.

The demonstrated sensor, polyethylene oxide coated fiber bend, based on power measurement at an optimised wavelength and bend radius showed a high sensitivity to RH variation. The sensor behaves as a humidity dependant optical switch between 85% and 90% RH. The sensor has a very fast response to humidity variations and the estimated response time is 780 milliseconds for a 20% RH change.

The selection of Agarose as a suitable hygroscopic coating for an RH sensor based on a fiber bend is explained and the influence of bend radius on the performance of such a sensor is discussed. The demonstrated sensor based on an Agarose coated fiber bend showed a linear change in its insertion loss for a wide humidity range, 25-90% RH. The measured response time of the sensor is circa 50 ms for a 30% RH change. It is shown that the humidity sensitivity of the sensor is wavelength dependent and high sensitivity is observed at higher wavelengths.

Both the sensors demonstrated in this chapter show a fast and reversible response to RH variations. Also it is shown that the typical humidity responses of the sensors are suitable for using them as a human breath rate monitor. Finally the limitations of the fiber bend based RH sensor are discussed in brief.

2.8. References

1. T. L. Yeo, T. Sun, K.T.V. Grattan, Fiber-optic sensor technologies for humidity and moisture measurement, *Sens Actuators A Phys* 144, pp. 280–295, (2008).
2. M. Konstantaki, S. Pissadakis, S. Pispas, N. Madamopoulos, N. A. Vainos, Optical fiber long-period grating humidity sensor with poly(ethylene oxide)/cobalt chloride coating, *Appl Opt*, 45 (19), pp. 4567-4571, (2006).
3. K. M. Tan, C. M. Tay, S. C. Tjin, C. C. Chan, H. Rahardjo, High relative humidity measurements using gelatine coated long-period grating sensors, *Sens. Actuators, B*, 110, pp. 335–341, (2005).
4. J. Mathew, K. J. Thomas, V. P. N. Nampoori and P. Radhakrishnan, A comparative study of fiber optic humidity sensors based on chitosan and agarose, *Sensors & Transducers Journal*, 84 (10), pp. 1633-1640, (2007).

5. B. D. Gupta, Ratnanjali, A novel probe for a fiber optic humidity sensor, *Sens Actuators B Chem,* 80, pp. 132-135, (2001).
6. F. J. Arregui, Z. Ciaurriz, M. Oneca, I. R. Mat´ıas, An experimental study about hydrogels for the fabrication of optical fiber humidity sensors, *Sens. Actuators, B*, 96, pp. 165-172, (2003).
7. S. Acikgoz, B. Bilen, M. M. Demir, Y. Z. Menceloglu, Y. Skarlatos, G. Aktas, and M. N. Inci, Use of Polyethylene Glycol Coatings for Optical Fiber Humidity Sensing, *Opt Rev*, 15(2), pp. 84–90, (2008).
8. D. C. Bownass, J. S. Barton, J. D. C. Jones, Serially multiplexed point sensor for the detection of high humidity in passive optical networks, *Opt Lett*, 22 (5), pp. 346-348, (1997).
9. C. Baria´in, I. R. Mat´ıas, F. J. Arregui, and M. Lo´pez-Amo, Optical fiber humidity sensor based on a tapered fiber coated with agarose gel, *Sens. Actuators, B* 69, pp. 127–131, (2000).
10. L. Zhang, F. Gu, J. Lou, X. Yin, and L. Tong, Fast detection of humidity with a subwavelength diameter fiber taper coated with gelatin film, *Opt Express*, 16(17), pp. 13349-13353, (2008).
11. J. M. Corres, I. R. Matias, M. Hernaez, J. Bravo, and F. J. Arregui, Optical fiber humidity sensors using nanostructured coatings of SiO_2 nanoparticles, *IEEE Sens J*, 8 (3), pp. 281-285, (2008).
12. Q. Wu, Y. Semenova, J. Mathew, P. Wang, G. Farrell, Humidity sensor based on a singlemode hetero-core fiber structure, *Opt Lett*, 36(10), pp. 1752-1754, (2011).

13. D. C. Bownass, J. S. Barton, J. D. C. Jones, Detection of high humidity by optical fiber sensing at telecommunications wavelengths, *Opt Commun*, 146, pp. 90-94, (1998).
14. J. Mathew, G. Rajan, Y. Semenova, and G. Farrell, All fiber tunable loss filter, *Proc. SPIE* 7503, 75037G-75037G-4, (2009).
15. J. D. Love, and C. Durniak, Bend Loss, Tapering, and Cladding-Mode Coupling in Single-Mode Fibers, *IEEE Photonics Technol Lett*, 19 (16), pp. 1257–1259, (2007).
16. L. Yao, A. Birks, and J. C. Knight, Low bend loss in tightly-bend fibers through adiabatic bend transitions, *Opt Express*, 17 (4), pp. 2962-2967, (2009).
17. H. F. Taylor, Bending Effects in Optical Fibers, *Journal of lightwave technology*, LT-2 (5), pp. 617-628, (1984).
18. K. J. Lee, D. Wawro, P. S. Priambodo, and R. Magnusson, Agarose-gel based guided-mode resonance humidity sensor, *IEEE Sens J*, 7(3), pp. 409-414, (2007).
19. G. Rajan, Y. Semenova, J. Mathew, G. Farrell, Experimental analysis and demonstration of a low cost fiber optic temperature sensor system for engineering applications, *Sens. Actuators, A*, 163(1), pp. 88-95, (2010).

CHAPTER 3. RELATIVE HUMIDITY SENSOR BASED ON A PHOTONIC CRYSTAL FIBER INTERFEROMETER

3.1. Introduction

In this chapter a novel relative humidity (RH) sensor is presented based on a reflection type photonic crystal fiber (PCF) interferometer. The existing fiber optic humidity sensors are either polymer based or require the use of a hygroscopic material to detect humidity (Table A.1). The sensor proposed here has the unique advantages that it does not require any special coatings to measure humidity and the sensor head is made of single material (silica). Because of these advantages the sensor proposed in this chapter is suitable for use in harsh and high-temperature environments.

As a basis for the sensors demonstrated in subsequent chapters, this chapter starts by presenting the relevant background material for a reflection type photonic crystal fiber interferometer (PCFI) such as the fabrication operating principle and the dependence of the interferometer's fringe spacing on the length of the PCF.

This chapter also discusses the water vapor adsorption/desorption phenomena of a silica surface, the working principle of a relative humidity sensor based on an open ended PCF interferometer. The humidity response of such a PCF interferometer and the temperature dependence of the device are then presented and discussed.

3.2. Photonic crystal fiber interferometer

Photonic crystal fiber interferometers based on micro-hole collapse have attracted significant interest in recent times due to the simple fabrication process involved and excellent sensing performance [1-7]. A reflection-type PCFI consists of a stub of PCF

fusion spliced at the distal end of a single mode fiber. The key element of the device is the hole collapsed region in the vicinity of the splice point. In addition to simplicity of fabrication, because such PCF interferometers are fabricated using only a splice, they have the advantage of high mechanical stability at high temperatures and over an extended period.

3.2.1 PCFI Working Principle

In a PCFI the excitation and recombination of modes is carried out by the hole collapsed region of the PCF [1-3]. A microscopic image of the PCFI and a schematic of the excitation and recombination of modes in the PCFI are shown in Fig. 3.1. The fundamental SMF mode begins to diffract when it enters the collapsed section of the PCF. Because of diffraction, the mode broadens; depending on the modal characteristics of the PCF and the hole collapsed region, the power in the input beam can be coupled to the fundamental core mode and to higher order core modes [2,5,8] or to cladding modes [1,4,9] of the PCF. The modes propagate through the PCF until they reach the cleaved end from where they are reflected. Since the modes propagate at different phase velocities, thus over a certain length of the PCF the modes accumulate a differential phase shift. Therefore constructive or destructive interference occurs in the PCF. Because of intermodal dispersion the phase velocities and phase differences are wavelength dependent; therefore the optical power reflected by the device will be maximum at certain wavelengths and minimum at others [6]. When the reflected modes re-enter the collapsed region they will further diffract and because the mode field of the SMF is smaller, the core acts as a spatial filter and picks up only a part of the resultant intensity distribution of the interference pattern in the PCF.

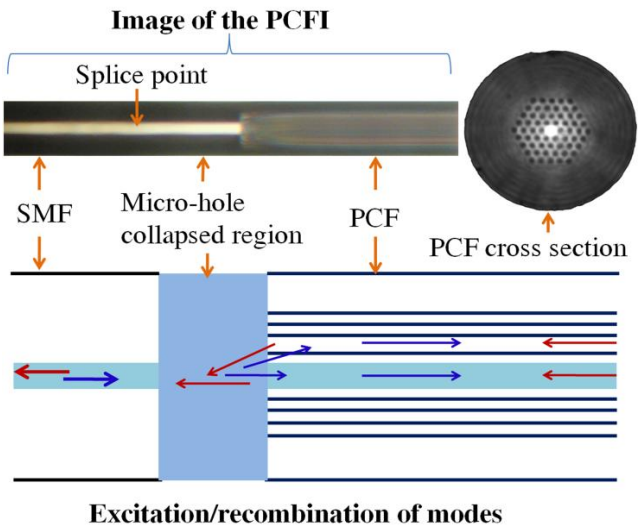

Fig.3.1. Microscope image of the PCFI (upper) & a schematic of the excitation/recombination of modes in the hole collapsed region (lower).

A regular interference pattern in the reflection spectrum of the PCFI usually suggests that only two modes are interfering in the device. In the reported works of PCF interferometer there is an inconsistency in opinions as to whether the interfering modes are core only modes or core and cladding modes. In our earlier reported work [7] on a PCFI using an LMA 10 type fiber and also the works in [2,5,8], based on the fact that higher order modes can exist in the core of a PCF with a short length [10,11], the interfering modes in the PCF are considered as two core modes. However in a later experiment, which involved varying the refractive index surrounding the cladding of a PCFI, good ambient refractive index sensitivity is observed for a PCFI fabricated using the same LMA 10 fiber. This suggests that the interfering modes are a core mode and a cladding mode of the PCF, a conclusion that is supported by [1,9] for an LMA10 fiber. Thus considering a core mode and a cladding mode as the interfering modes of the PCFI and designating the effective refractive indexes of the core mode as n_c and cladding mode as n_{cl}, the accumulated phase difference is $2\pi\Delta n(2L)/\lambda$, where $\Delta n=n_c-n_{cl}$, λ the wavelength of the optical source and L is the physical length of the PCFI [5]. The power

reflection spectrum of this interferometer will be dependent on cos($4\pi\Delta nL/\lambda$). The wavelengths at which the reflection spectrum shows maxima are those that satisfy the condition $4\pi\Delta nL/\lambda=2m\pi$, with m being an integer. This means that periodic constructive interference occurs when $\lambda m = (2\Delta nL/m)$. If some external stimulus changes Δn (while L is fixed) the position of each interference peak will change, an effect which allows the device to be used for sensing.

3.2.2 PCFI Fabrication

Fusion splicing of the PCF to the SMF is undertaken using the electric arc discharge of a conventional arc fusion splicer. During the splicing process the voids of the PCF collapse through surface tension within a microscopic region close to the splice point. In fabricating such an interferometer, one critical condition for good sensor performance is achieving a regular interference pattern and good interference fringe visibility. The visibility of the interferometer depends on the power in the excited modes, which in turn depends on the length of the collapsed region [8]. A long collapsed region length causes activation of many cladding modes and therefore degrades the sinusoidal nature of the interference patterns and furthermore increases the splice loss. Therefore to improve sensor performance, the excitation of a single cladding mode is preferred due to its simple interference with the core mode. The collapsed region length can be controlled by the arc power, arc duration [8] or by number of arcs. The microscope image of splice points given in Fig 3.2 clearly demonstrates the increase in the microhole collapsed region length with respect to number of arcs under a constant arc power and duration. The splicer used for the experiment is Sumitomo type-36 fusion splicer and its settings are arc power = 1 and arc time = 1 sec. The measured microhole collapsed region length is plotted against the applied number of arcs in Fig. 3.3.

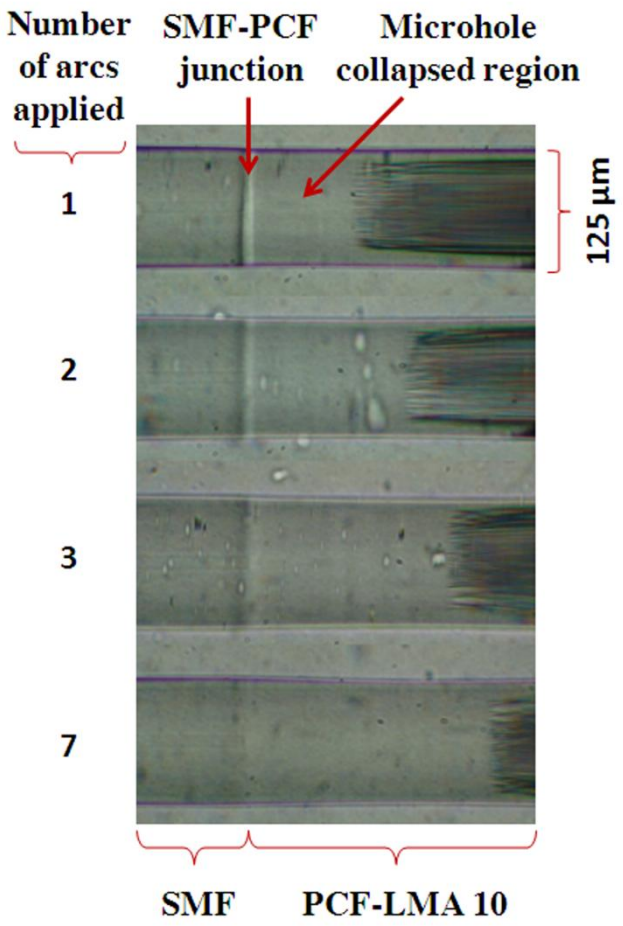

Fig. 3.2 Microscope image of the splice point showing the increase in the microhole collapsed region with respect to number of arcs.

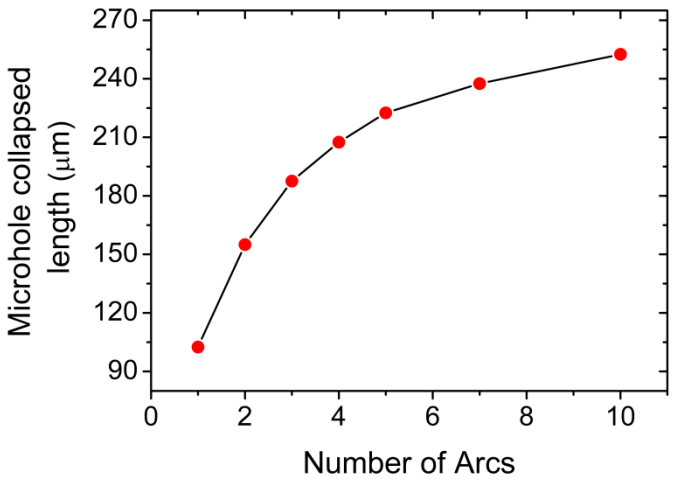

Fig. 3.3 Microhole collapsed region length with respect to the applied number of arcs.

In our experiments, PCF (LMA10, NKT Photonics) designed for an endless single-mode operation was used. It has four layers of air holes arranged in a hexagonal pattern around a solid silica core as shown in Fig 3.1. The light guidance mechanism in such a fiber is by means of modified total internal reflection. The dimensions of the LMA-10 PCF simplify alignment and splicing with the SMF with a standard splicing machine and minimize the loss due to mode field diameter mismatch compared to other PCFs. For the interferometer fabricated in our study the total length of the collapsed region is ~200 μm. After fusion splicing, the PCF was cleaved using a standard fiber cleaving machine so that the end surface of the PCF acted as a reflecting surface.

3.2.3 PCFI fringe spacing Vs length of PCF

Initially to investigate the influence of the length of the PCF on the fringe spacing of a reflection type interferometer, thirteen PCFIs were fabricated with lengths ranging from 3.5 mm to circa 100 mm. As an example Fig. 3.4 shows the measured reflection spectra of three PCFIs in the 1500-1600 nm wavelength range with lengths of 92, 10.5 and 3.5 mm. The reflection spectra of the interferometers exhibit regular interference patterns with a period or fringe spacing inversely proportional to the length of the PCF section. A modulation of the expected sinusoidal pattern is observed for the spectra shown in Fig. 3.4 possibly due to excitation of more than one cladding modes or due to polarization dependence of the intermodal interference [12]. Fig. 3.5 shows the measured fringe spacing or periods of the fabricated PCFIs spectra as a function of length of the PCF section. The measured spectral periods agree well with those expected for a two-mode interferometer and are given by the approximate expression,

$$P \approx \frac{\lambda^2}{2\,\Delta n\,L} \tag{3.1}$$

The value of Δn obtained based on the experimental data is ~4.2×10^{-3} where the source wavelength is assumed as 1550 nm and the ambient medium as air.

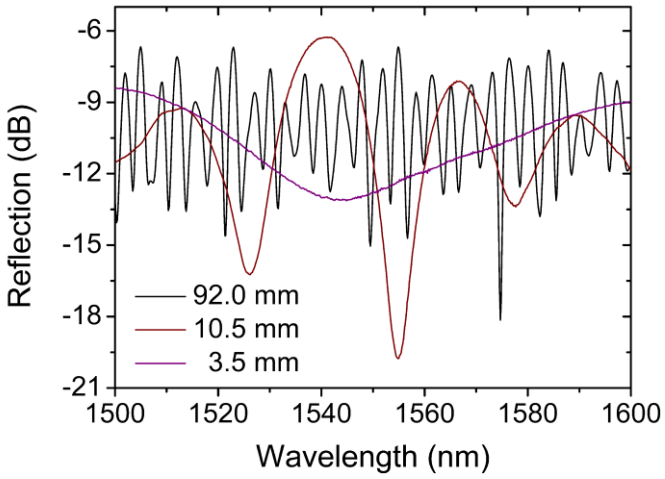

Fig. 3.4. The reflection spectra of interferometers with L = 92 mm, 10.5 mm and 3.5 mm in the wavelength range of 1500-1600 nm.

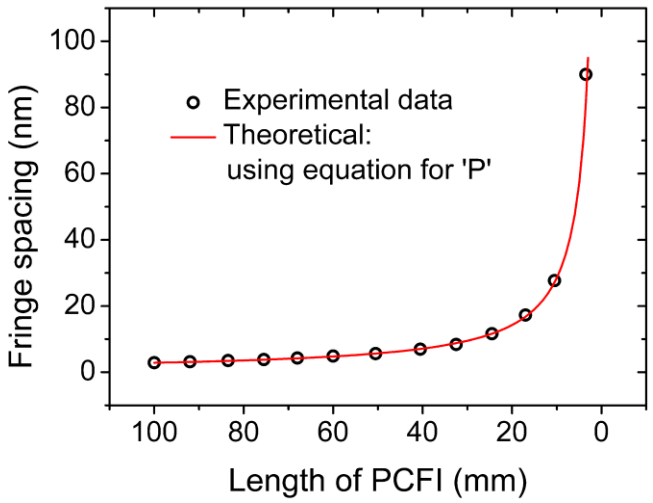

Fig. 3.5. The fringe spacing as a function of length of PCF observed for a reflection type interferometer.

3.3. Relative humidity sensor based on a PCFI

A wide range of optical fiber humidity sensors have been reported in the literature and most of these fiber optic humidity sensors work on the basis of a hygroscopic material

coated over the optical fiber to modulate the light propagating through the fiber (Table A.1). A polymer optical fiber has been adapted for humidity sensing [13] without the use of a hygroscopic coating but the fiber is highly temperature dependent and moreover is not suitable for high-temperature applications. An all-glass fiber-optic relative humidity sensor which does not require any special coatings to measure humidity using a reflection-type two-mode photonic crystal fiber interferometer is presented in this section of the chapter. The spectrum of the PCFI device exhibits good sensitivity to humidity variations.

3.3.1 Experimental characterization of the sensor

The proposed sensor system is composed of a broadband light source (SLED), a fiber coupler/circulator (FOC), the PCF interferometer or sensor head, and an optical spectrum analyser (OSA) as shown in Fig. 3.6. The free end of the PCF in the sensor head is exposed to ambient air. The humidity response of the device was studied at room temperature (25 ^{O}C) and at normal atmospheric pressure by placing it in a controlled environmental chamber as shown in Fig. 3.6. Fig. 3.7 shows the changes in the reflection spectrum with respect to ambient humidity for a device with L=40.5 mm. The curves in Fig. 3.7 show the position of a zoomed section of the device spectrum at relative humidity values of 30, 60, 80 and 90 %RH. When humidity increases the interference pattern shifts to a longer wavelength and this shift is more significant at higher humidity values. To study the effect of reducing the length of the PCFI a second PCFI was fabricated with a shorter length of 17 mm. Fig. 3.8 shows the peak shift of the interferometer with respect to humidity, obtained for two devices with L=17 mm and 40.5 mm.

It is observed from the Fig. 3.8 that the sensitivity of the device to humidity decreases as the length of the device decreases. This is due to the fact that for a small device the fiber length available for interaction between the cladding mode with the adsorbed water vapor is less so the acquired phase difference between the interfering modes will be smaller.

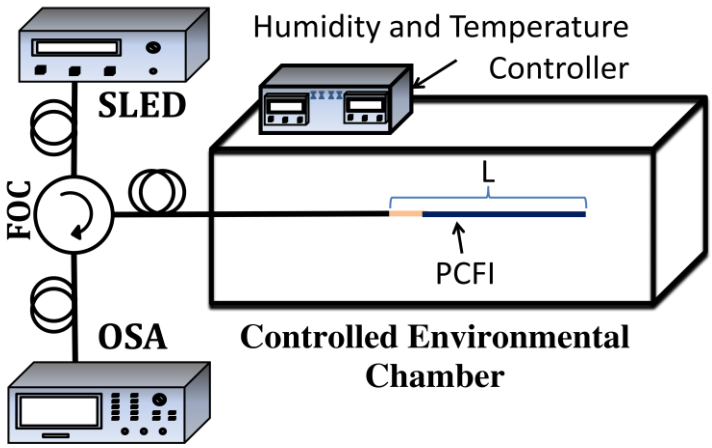

Fig. 3.6. Experimental arrangement for the characterisation of the PCFI with respect to relative humidity.

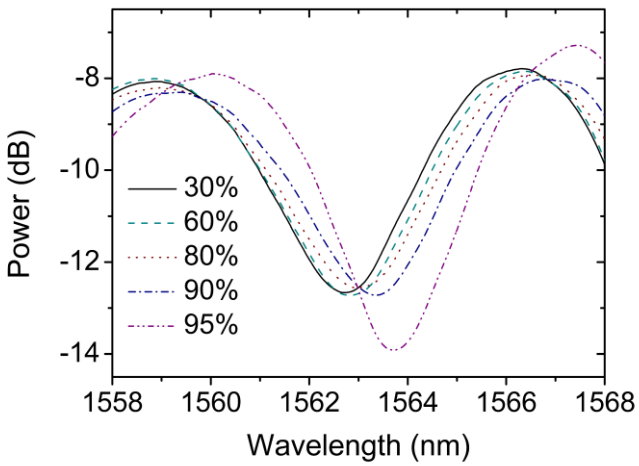

Fig. 3.7. Reflection spectrum of a 40.5 mm long PCFI at different humidity values.

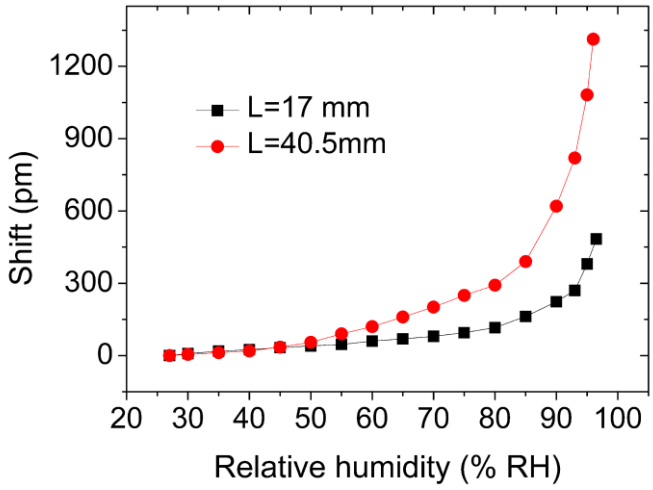

Fig. 3.8. Interference peak shift of photonics crystal fiber interferometers with L= 40.5 mm and 17 mm with respect to relative humidity.

3.3.2 Operating principle of the sensor

A bare silica PCF is used for the fabrication of the PCFI, its surface is hydrophilic and therefore the adsorption of water vapor on the surface occurs when it is exposed to humid air. Two types of water-vapor adsorption mechanisms occur in sequence at the SiO_2-air interface. The chemisorption of water vapor first modifies the SiO_2 surface, resulting in a surface with silanol groups (Si-OH). The second type of adsorption, physisorption, occurs on these silanol groups. A schematic illustration of the water-vapor adsorption is given in Fig. 3.9. At room temperature the physisorption is a reversible function of the relative humidity of the surrounding air, while the chemisorption appears to be irreversible [14], hence in the following discussion only the physisorption is considered. Adsorption is usually described through isotherms, that is, the amount of adsorbate on the adsorbent as a function of its pressure (if gas) or concentration (if liquid) at a constant temperature. Awakuni and Calderwood [15] investigated the adsorption of water vapor on the SiO_2 surface. They measured the amount of adsorbed water as a function of the partial vapor pressure at a constant

temperature. It appeared that this so-called adsorption isotherm can be described very well by the BET (Brunauer- Emmett- Teller) adsorption theory [16] that describes the multilayer adsorption of an adsobate on the adsorbent. That means the amount of water vapor adsorbed on the silica surface increases in an exponential-like manner with respect to the increase of the partial pressure of water vapor.

The evolution of an adsorbed water layer structure on silicon oxide at room temperature is demonstrated by David and Seong in [17]. They determined the molecular configuration of water adsorbed on a hydrophilic silicon oxide surface at room temperature as a function of relative humidity using attenuated total reflection-infrared spectroscopy. A completely hydrogen-bonded network of water, which is ice-like, grows up as the relative humidity increases from 0 to 30%. In the relative humidity range of 30-60%, the liquid water structure starts appearing while the ice-like structure continues growing to saturation. Above 60% relative humidity, the liquid water configuration grows on top of the ice-like layer. This structural evolution indicates that the outermost layer of the adsorbed water molecules undergoes transitions between different equilibrium states as humidity varies. Also the adsorption isotherm given in [17] shows that the thickness of the adsorbed layer at room temperature increases in an exponential like manner above 60% RH.

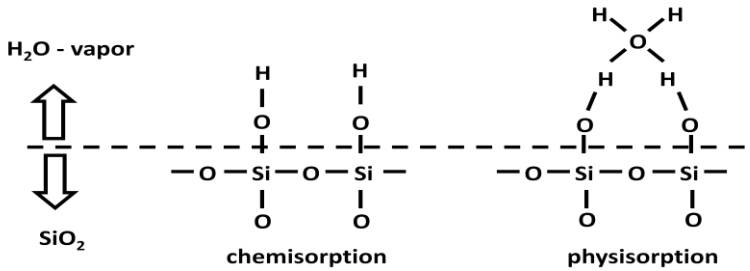

Fig. 3.9 Schematic representation of water vapor adsorption mechanisms on an SiO_2 surface (reproduced from [14])

Tiefenthaler and Lukosz [18] have shown that adsorption and desorption of water vapor by the surface of a SiO_2/TiO_2 waveguide changes the effective refractive index (RI) of the guided modes, in their case for a humidity sensor based on an integrated optical grating coupler. In the case of a PCFI a similar adsorption of water vapor changes the effective refractive index (n_{cl}) of the interfering cladding mode propagating in the PCF. Since this adsorption/physisorption is a reversible process, a modulation of the n_{cl} occurs with respect to the ambient humidity values which in turn change the position of the interference pattern accordingly. An increase in humidity increases the effective index of the cladding mode which causes the shift of the interference pattern of a PCFI toward longer wavelengths. The value of this interference peak shift is exponential-like with respect to relative humidity that means it is identical to the adsorption isotherm of water vapor on silica given in [15,17]. The shift of the interference pattern is mainly due to the adsorption and desorption of H_2O molecules along the surface of holes within the PCF, at the interface between air and silica glass. Since the whole device is exposed to humidity the adsorption and desorption of water vapor on the PCF outer surface and on the end face also contribute to the shift of the interference pattern. But considering the field distribution of the interfering cladding mode shown in [9,11] and below the dew point temperature the main contribution to the interference shift is considered to be due to the adsorption of water molecules within the voids of the PCF. The adsorption on the end face mainly causes a shift in the overall power level of the interference pattern.

3.3.3 Performance analysis of the RH sensor

The device sensitivity is estimated by dividing the experimentally measured PCFI response to humidity given in Fig. 3.8 into three humidity regions: 27-60 %RH, 60-80 %RH, and 80-96 %RH. From Fig. 3.8 the average sensitivity values observed for the PCFI with a length of 40.5 mm in these regions are 3.7, 8.5 and 64 pm/%RH

respectively and for a 17 mm long PCFI they are 1.7, 3 and 23 pm/%RH respectively. Even though the PCFI with a longer length appears more sensitive, it is likely that increasing the length of the PCFI to a much longer length is not practical because in a longer device the infiltration of water molecules may take a long time. Furthermore, since the propagation loss of the interfering cladding mode is high the fringe visibility will diminish on increasing the length of the PCF section. Also for a longer device the fringe spacing will be shorter which limits the measurement range of the device. Decreasing the length of the PCFI to a much shorter length is also not appropriate because as seen from Fig. 3.4 & 3.5 if the length is less than 3.5 mm the fringe spacing will be greater than 100 nm, the bandwidth of a typical SLED spectrum, and therefore not suitable for accurately determining the shift in the interference spectrum. Selecting a shorter length will also result in a reduced sensitivity but that can be improved by infiltrating the microholes with suitable hygroscopic materials.

The RH response of the PCFI device is studied number of times and it is observed that the device shows a good repeatability for humidity changes. This is because the chemisorption happens only once when the PCF is exposed to air for the first time, which results in the formation of a single layer of a silanol (Si-OH) group on the surface of the PCF material (requires heating to desorb). On this silanol group the physisorption takes place, it can form multiple layers of water molecules on the PCF surface and also it is a reversible process at room temperature in eqilibrium with the ambient RH. Therefore it is concluded that the physisorption is the dominant process responsible for the reversible spectral shift of the interferometer with respect to the ambient RH. Under laboratory conditions the sensor is reusable, but the measurement of humidity means that the sensor must be exposed to the local environment, which for this sensor, which relies on narrow silica microholes, has implications for contamination and degradation

of the sensor in varying degrees depending on the nature of the environment. Possible contamination agents are dust particles and chemical vapors. So a further study of the sensor head contamination in different process environments and the observation of the shift in its response in such conditions are required in order to get a better understanding of the long term stability of our sensor in field applications. In the case of a PCFI based sensor this limitation can be overcome by different ways; a recalibration of the sensor head after a certain period of time and a subsequent reuse of the sensor head during another time interval, or, since the fabrication of the PCFI based sensor head is simple and cost effective, replacing the sensor head or attaching some filters to the sensor head by which it can be protected from contamination. An ultrasonic cleaning with subsequent heating (which should remove the contaminants such as dust particles without damaging the sensor head) is another method to make the sensor reusable after contamination.

3.3.4 Temperature dependence of the device

Since the PCF is composed of fused silica only, it is expected to have minimal thermal sensitivity. The temperature dependence of the device was determined by observing the peak shift of the interference spectrum of the device for a temperature variation from 25 ^{O}C to 60 ^{O}C. The ambient humidity during the study was set to 40 % RH. When the temperature is increased from 25 ^{O}C to 60 ^{O}C the interference peak is shifted slightly to higher wavelengths. Fig. 3.10 shows this temperature dependence for two devices with L=17 mm and 40.5 mm. As expected the thermal sensitivity of the PCFI is very low and is further reduced for a device with the shorter length of the PCF section. The thermal sensitivity obtained in the experiment for a device with L= 40.5 mm is 9.5 pm/^{O}C and that for L= 17 mm is 6.2 pm/^{O}C.

The study of cross sensitivity to temperature reveals that the PCFI based humidity sensor is almost temperature independent. Conventional glass fiber relative humidity sensors require coatings and thus are always temperature dependent and, furthermore, since the majority of such sensors use polymer materials as coatings, they are not suitable for use in high-temperature applications. One significant advantage of the sensor discussed here is that the sensor head is made of single material silica. This suggests that in addition to low and room temperature applications the PCF interferometer based humidity sensor can also be used in harsh and high-temperature environments to monitor humidity.

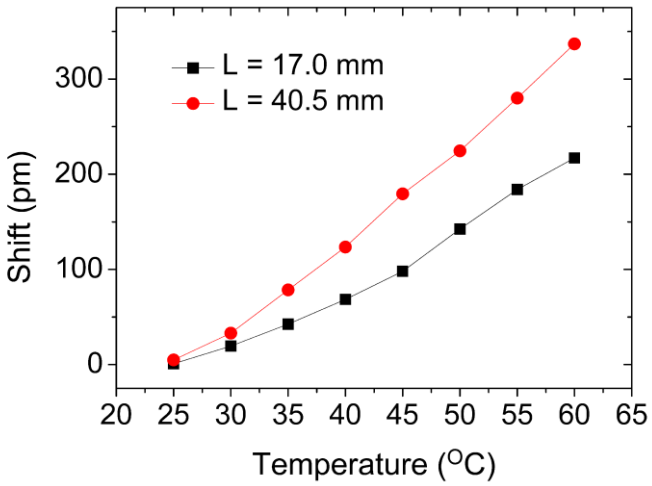

Fig. 3.10 Interference peak shift with respect to temperature for interferometers with PCF lengths L= 40.5 mm and 17 mm.

3.4. Summary

A brief overview of the operating principle and the fabrication of a reflection type PCF based modal interferometer is presented in this chapter. The dependence of the interferometer fringe spacing on the length of the PCF section is also discussed and demonstrated experimentally. The experimental investigation and demonstration of a humidity sensor based on a PCF interferometer are presented in the chapter with a brief

explanation of the operating principle of the sensor. The water vapor adsorption/desorption phenomena on silica surface are briefly addressed to explain the operating principle of the sensor. The chapter includes the experimental investigation of the relative humidity response of the sensor and the dependence of its sensitivity on the length of PCF. It is shown that a device with a longer length of the PCF section is more sensitive to relative humidity changes. The chapter also presents the temperature dependence of the PCF interferometer and the dependence of its sensitivity on the length of the PCF.

3.5. References

1. H. Y. Choi, M. J. Kim, and B. H. Lee, All-fiber Mach-Zehnder type interferometers formed in photonic crystal fiber, *Optics Express*, 15(9), pp. 5711–5720, (2007).
2. J. Villatoro, V. P. Minkovich, V. Pruneri, and G. Badenes, Simple all microstructured optical fiber interferometer built via fusion splicing, *Optics Express*, 15 (4), pp. 1491-1496, (2007).
3. J. Villatoro, V. Finazzi, V. P. Minkovich, V. Pruneri, and G. Badenes, Temperature-insensitive photonic crystal fiber interferometer for absolute strain sensing, *Applied Physics Letters*, 91 (9), pp. 091109, (2007).
4. R. Jha, J. Villatoro, and G. Badenes, Ultrastable in reflection photonic crystal fiber modal interferometer for accurate refractive index sensing, *Applied Physics Letters*, 93 (19), pp. 191106, (2008).
5. J. Villatoro, M. P. Kreuzer, R. Jha, V. P. Minkovich, V. Finazzi, G. Badenes, and V. Pruneri, Photonic crystal fiber interferometer for chemical vapor detection with high sensitivity, *Optics Express*, 17(3), pp. 1447-1453, (2009).

6. J. Villatoro, V. Finazzi, G. Badenes, and V. Pruneri, Highly sensitive sensors based on photonic crystal fiber modal interferometers, *Journal of Sensors*, 2009, Article ID 747803, 11 pages, (2009).
7. J. Mathew, Y. Semenova, G. Rajan, and G. Farrell, Humidity sensor based on photonic crystal fiber interferometer, *Electronics Letters*, 46(19), pp. 1341-1343, (2010).
8. D. Barrera, J. Villatoro, V. P. Finazzi, G. A. Cardenas-Sevilla, V. P. Minkovich, S. Sales, and V. Pruneri, Low-loss photonic crystal fiber interferometers for sensor networks. *Journal of Lightwave Technology*, 28(24), pp. 3542–3547, (2010).
9. G. A. Cárdenas-Sevilla, V. Finazzi, J. Villatoro, and V. Pruneri, Photonic crystal fiber sensor array based on modes overlapping, *Optics Express*, 19(8), pp. 7596-7602, (2011).
10. D. Káčik, I. Turek, I. Martinček, J. Canning, N. Issa, and K. Lyytikäinen, Intermodal interference in a photonic crystal fiber, *Optics Express*, 12(15), pp. 3465-3470, (2004).
11. H. P. Uranus, Theoretical study on the multimodeness of a commercial endlessly single-mode PCF, *Optics Communications*, 283(23), pp. 4649–4654, (2010).
12. W. J. Bock, T. A. Eftimov, P. Mikulic, and J. Chen, An inline core-cladding intermodal interferometer using a photonic crystal fiber, *Journal of Lightwave Technology*, 27(17), pp. 3933–3939, (2009).
13. C. Zhang, W. Zhang, D. J. Webb, and G. D. Peng, Optical fiber temperature and humidity sensor, *Electronics Letters*, 46(9), pp. 643-644, (2010).

14. J. A. Voorthuyzen, K. Keskin, and P. Bergveld, Investigations of the surface conductivity of silicon dioxide and methods to reduce it, *Surface Science*, 187 (1), pp. 201-211, (1987).
15. Y. Awakuni, and J. H. Calderwood, Water vapor adsorption and surface conductivity in solids. *Journal of Physics D: Applied Physics*, 5(5), pp. 1038, (1972).
16. S. Brunauer, P. H. Emmett, and E. Teller, Adsorption of gases in multimolecular layers, *Journal of the American Chemical Society*, 60, pp. 309-319, (1938).
17. B. A. David, and H. K. Seong, Evolution of the adsorbed water layer structure on silicon oxide at room temperature, *Journal of Physical Chemistry B*, 109(35), pp. 16760-16763, (2005).
18. K. Tiefenthaler, and W. Lukosz, Grating couplers as integrated optical humidity and gas sensors. *Thin Solid Films*, 126, pp. 205-211, (1985).

CHAPTER 4. RELATIVE HUMIDITY SENSOR BASED ON AN AGAROSE INFILTRATED PHOTONIC CRYSTAL FIBER INTERFEROMETER

4.1. Introduction

In the previous chapter it is proposed to use a photonic crystal fiber interferometer (PCFI) operating in reflection mode for relative humidity (RH) sensing, with the benefits of simplicity, low cost and the need for only one interconnecting fiber to an interrogation system. The sensor head fabrication was also simple since it involved only cleaving and splicing. The sensor showed a shift in its interference pattern due to the adsorption and desorption of water vapor with respect to ambient humidity. But the length of the sensor was relatively long (~ centimeters) and its humidity measurement resolution was relatively poor. In this chapter a new PCFI based relative humidity sensor is proposed with a focus on achieving an improved sensitivity, a very significantly reduced length and a wider humidity range. The sensitivity of the sensor is improved by infiltrating the micro holes of the PCF with a hygroscopic material. Furthermore it is shown that a suitable selection of a sub-periodic portion of the interferometer's spectrum allows a reduction in the length of the sensor head making it suitable for monitoring RH in situations when the space available is constrained. An additional advantage of selecting a compact length for the sensor is that such a sensor is more mechanically stable in the presence of vibrations and air flow currents. The selected hygroscopic polymer Agarose is proven to change its refractive index over a wide humidity range; hence a wide measurement range for the sensor is expected. The chapter also aims to study the performance of this RH sensor in terms of its sensitivity,

repeatability, long term stability, measurement accuracy, response time and temperature dependence.

In this chapter a novel fiber optic hybrid device for simultaneously measuring temperature and humidity is also investigated. The device is composed of an in-line fiber Bragg grating (FBG) and a reflection type PCFI infiltrated with humidity sensitive material Agarose. The Agarose infiltrated PCFI is used to monitor the RH and an in-line FBG is used to monitor the temperature. The RH and temperature response of the hybrid device and the cross sensitivity of the device to these measurands are also investigated in this chapter.

4.2 RH sensor based on Agarose infiltrated PCFI

4.2.1 Operating principle of the sensor

The fundamentals of light propagation in a reflection type photonic crystal fiber interferometer are given in section 3.2.1 of chapter 3. A small region of the micro holes of the PCFI is infiltrated with Agarose. The effective refractive index of the cladding mode depends on the refractive index of the Agarose material infiltrated into the PCF. Since the Agarose material is infiltrated in to the microholes where the intense field of the cladding mode is present, it is expected that the thickness change of the infiltrated Agarose is the dominant factor which determines the effective RI of the material (for more details on the effect of thickness on the RI of the material please refer to chapter 5, section 5.4). Therefore the effective refractive index of the infiltrated Agarose increases with an increase in the ambient relative humidity, which in turn changes the modal propagation constant of the cladding mode. As a result a phase change is induced between the interfering core and cladding modes which in turn causes the shift of the interference pattern. Thus the relative humidity level can be measured by monitoring the

humidity induced changes in the interference fringes in the reflection spectrum of the Agarose infiltrated PCFI. Compared to the sensor demonstrated in the previous chapter the infiltrated Agarose in this case causes an amplified effective RI change of the interfering cladding mode with respect to an RH change. Therefore a higher RH sensitivity is expected for the Agarose infiltrated PCFI demonstrated in this chapter.

4.2.2. Experimental investigation of the sensor & discussion

The fabrication process of the reflection type photonic crystal fiber interferometer used in this experiment is similar to that given in chapter 3. In this experiment the microhole collapsed region length for the device is about 250 μm and the calculated modal index difference Δn is ~3.64×10^{-3}. From equation (3.1) it is clear that when the length of the PCF is less than 3 mm the period will be greater than 100 nm. Therefore for a small sensor length only a narrow sub-periodic part of the interference pattern with a 100 nm span can be observed. In this experiment a compact length of 1 mm for the sensor head is selected. The fringe spacing of a PCFI with a 1 mm length calculated using the equation (3.1) is about 330 nm. This allows the use of a broadband source such as a super luminescent diode (SLED) for the interrogation of the device in the optical power domain.

An additional advantage of choosing a compact length is that if the length of the PCF section of the interferometer is relatively large the spectra observed may be unduly perturbed by mechanical vibrations and air flow currents. This is because bending or lateral strain of the PCFI may cause a shift in the interference pattern that is not related to humidity and this phenomenon becomes more significant as the PCFI length increases. For a sensor head with a short length of 1 mm it is observed that the spectrum is very stable when subjected to vibrations and air flow. The tolerance in the fabrication

of such a compact PCFI using a conventional cleaver is possible with a ~10% error in its length.

The complete sensor system is composed of a super luminescent diode, a fiber coupler/circulator (FOC), the Agarose infiltrated PCF interferometer as a sensor head, and a photo detector (PD)/optical spectrum analyzer (OSA). A drawing of the sensor head is given in Fig. 4.1. The light from the optical source is launched into the sensor head through a circulator. The experimental arrangement for the calibration of the sensor is similar to the one given in the previous chapter (Fig 3.6).

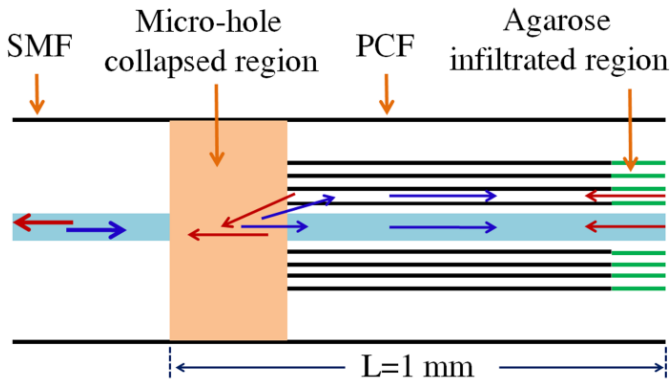

Fig. 4.1. A drawing of the sensor head for an Agarose infiltrated photonic crystal fiber interferometer.

In order to confirm that the humidity sensitivity of a compact PCFI is mainly due to the RI change of the infiltrated hygroscopic material, it is useful to initially study the relative humidity response of a compact PCFI prior to infiltration with a hygroscopic material. This was done at room temperature (23.1±0.2 ^{O}C) and at normal atmospheric pressure by placing it in the controlled environmental chamber. Fig. 4.2 shows the changes in the reflection spectrum with respect to ambient relative humidity for a PCFI with length ~1 mm. A small change in the reflected signal power (< 0.25dB for a humidity change of 58 %RH) is observed at higher relative humidity values. Therefore

it is concluded that an uninfiltrated PCFI with a compact length has only a weak sensitivity to relative humidity changes. Also this is in agreement with the results given in chapter 3, that when the length of PCF decreases the RH sensitivity of the PCFI decreases (see Fig. 3.8).

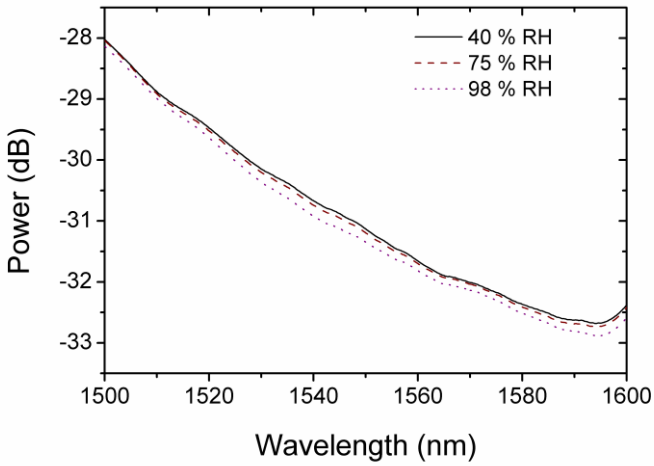

Fig. 4.2 The change in the reflection spectrum of a compact PCFI with length ~1 mm with respect to different ambient relative humidity values.

In order to improve the humidity sensitivity of a compact PCFI the micro holes of the PCF were infiltrated with hygroscopic polymer Agarose by immersing the tip of the PCF in a hot Agarose solution. The factors that make Agarose a suitable choice as a hygroscopic material are discussed in section 2.5.1 of chapter 2. The Agarose solution in this study is prepared by dissolving 1 wt% Agarose in distilled water at a temperature of 65 ^{O}C. Then keeping the solution at the same temperature the open end of the PCF is immersed in this solution for about 20 seconds. The outer portion of the fiber is wiped using a dry lens cleaning tissue immediately after the fiber is pulled out from the solution. When the infiltrated mixture is cooled, the gel polymerizes and once the gelling point is reached (<30 ^{O}C) the mixture assumes its hydro-gel form and will not take a liquid form again unless it is heated and reaches its melting point (> 60 ^{O}C). The

initial infiltration length depends on capillary forces, the length of the PCFI and the temperature. At a constant temperature it is the balance between the capillary forces and the forces exerted by the pressure of the air inside the silica holes. In this case the air inside the micro holes compresses as a result of the sudden cooling from 65 ^{O}C to room temperature of 23 ^{O}C after the fiber is taken out of the solution and this results in an increase in the infiltration length inside the microholes of the PCFI. For the sensor presented here the infiltration length was estimated using a polarizing microscope to be about 100±5 μm. The tip of the PCF is cleaned again using a scotch tape, before characterization. The Agarose infiltrated fiber is kept for one day at room temperature until it is partially dehydrated and reaches the equilibrium with the ambient environment. A schematic of the fabricated sensor is shown in Fig. 4.1. The size of the sensing element is 1 mm in length and 125 μm in diameter, the length includes both the 250 μm hole collapsed region and approximately 100 μm Agarose infiltrated region.

The humidity response of the sensor was studied at a typical room temperature (23.1±0.3 ^{O}C) and at normal atmospheric pressure by placing it in a controlled environmental chamber. Fig. 4.3 shows the changes in the reflection spectrum with respect to ambient relative humidity. The power level of the data shown in Fig. 4.3 is normalized to the reflected power from the cleaved end of a SMF at each wavelength. When humidity increases, the RI of Agarose increases and the effective index of the interfering cladding mode increases and as a result the interference pattern shifts to longer wavelengths. Therefore the reflected power decreases for the sensor in the observed wavelength region, which is a sub-periodic portion of the interference spectrum. The reflection spectrum of the sensor measured by an OSA shows a high sensitivity to humidity variations with an average change in the reflected power of about 7 dB for a humidity change of 65 %RH as shown in Fig. 4.3. In order to determine the

shift of the interference spectrum with respect to humidity in the case of an Agarose infiltrated PCFI, experiments were carried out using infiltrated PCFI's with different PCF lengths (L > 4 mm), and it is observed that the interference spectrum shifted to higher wavelengths with an increase in ambient relative humidity. That is for an increase in the refractive index of the Agarose layer with respect to relative humidity [1], the interferometer spectra shifts to higher wavelengths.

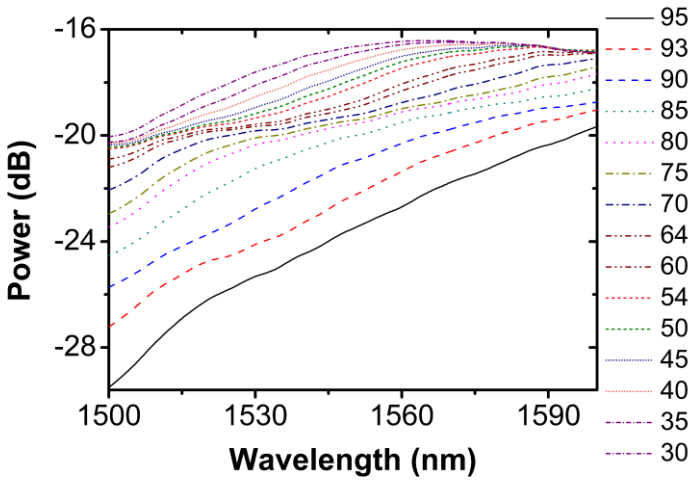

Fig. 4.3. Spectral response of Agarose infiltrated PCFI at different relative humidity values (% RH).

In practice it is not necessary to use an OSA to interrogate the sensor. In this experimental setup to demonstrate humidity measurement an SLED having an optical bandwidth of 54.5 nm and a center wavelength of 1544.5 nm (COVEGA Corporation, SLD 6593) and an optical power meter (PX Instrument Technology, PX2000-306) are used to determine the changes in the reflected power induced by humidity changes. Due to the large fringe spacing (>300 nm) of the PCFI the SLED used is suitable for interrogation of the humidity sensor. It should be noted however that a more effective approach is to replace the broadband SLED with a simple single-wavelength optical source which also reduces the cost of the system. Appropriate selection of the sensor

operating wavelength is important; in an ideal case the operating wavelength should be at the center of a selected linear region in the interference spectrum. If the source wavelength is fixed it is possible to adjust the spectral response for the sensor by controlling the PCFI length and the length of the air hole collapsed region by adjusting the arc power and arc duration during splicing. Fig. 4.4 shows the reflected power variation of the sensor with respect to humidity. The error bars shown in Fig. 4.4 are calculated based on the data obtained from six experimental measurements taken for the humidity response of the sensor. This error in measurements is found to be mainly due to the hysteresis observed for the forward and reverse response of the sensor.

The response shows two regions of different sensitivity. A wide humidity range from 14-86 %RH with a sensitivity of 0.06 dB/%RH and a small range of 86-98 %RH with a higher sensitivity of 0.6 dB/%RH. Assuming only two modes are interfering in the sensor, the change in slope and thus sensitivity in Fig. 4.4 mainly arises because of the rate of change of refractive index of Agarose with respect to relative humidity above 80 %RH, where the rate of change increases and becomes non linear. Considering the error in the measurements observed for the sensor, the accuracy of the sensor in the range 14-86 %RH varies from ±1 to ±7%RH and in the range 86-98 %RH the accuracy is about ±2 %RH.

In order to study the long term stability of the Agarose infiltrated PCFI sensor, a second series of experiments are carried out after 60 days from the initial experiments. A similar experimental condition is maintained for both these measurement series. In order to compare these results the averaged relative humidity response obtained for the sensor during these two series of measurements is plotted in Fig. 4.5. The relative humidity responses obtained are similar, confirming good long term stability for the sensor.

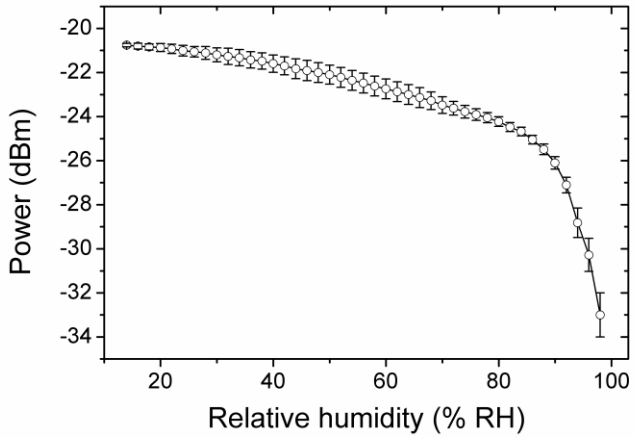

Fig. 4.4. Relative humidity response of the sensor (error bars shown are calculated based on the data obtained from six experimental measurements).

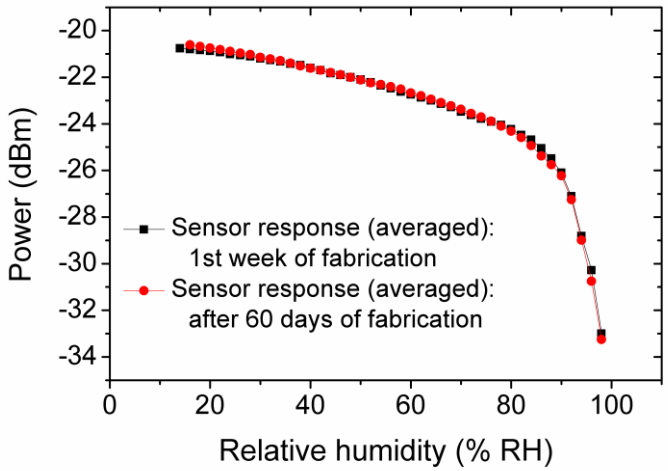

Fig. 4.5. Relative humidity response of the sensor taken with a time interval of 60 days showing the long term stability of the sensor.

4.2.3 Temperature dependence of the sensor

The temperature dependence of the Agarose infiltrated PCFI sensor was observed by setting the ambient relative humidity value at 50 % RH and is shown in Fig. 4.6. The error bars shown in Fig. 4.6 are calculated from the data obtained from four experimental measurements. A change in the reflected power of about +/-0.66 dB is

observed for a temperature variation of 10 ^{O}C. Since PCF is made of single material silica, the PCFI itself is almost temperature independent. Therefore this small power variation of 0.066 dB/^{O}C is attributed to the temperature dependence of Agarose. The thermally induced variation of the refractive index (RI) for different polymeric materials was reported in [2,3]. According to these references the RI of polymeric materials usually decrease with an increase in temperature. Similarly the RI of the Agarose also decreases with an increase in temperature which in turn results in this small power variation in the reflected signal of the sensor. While the temperature induced variation is relatively small, it is likely in an environment with large temperature changes that temperature monitoring to allow for correction of the measured RH would be required. However many applications of humidity sensors involve room temperatures, where temperature fluctuations are smaller.

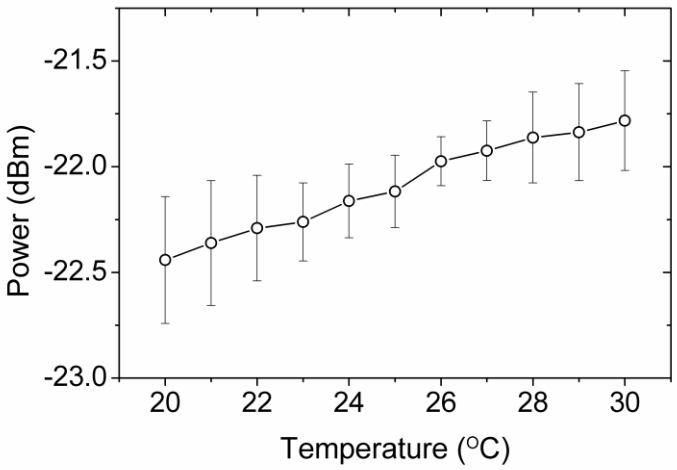

Fig. 4.6. Temperature dependence of the sensor.

4.2.4 Time response of the sensor

In order to study the response time of the sensor a step change in humidity to the sensor is applied by directing a ~ 1.5 s long human breath exhale to the sensor; the resultant

time dependant response is shown in Fig. 4.7. The ambient humidity during the study was ~60 %RH and the temperature ~23 ^{O}C. The reflection power level for the sensor shown in Fig. 4.7, at RH >90% is not a constant. This is because of the fluctuations in the humidity (95±5%) around the sensor due to the prevailing air current resulting from the applied breath exhale. The estimated response time (10% to 90% signal maximum) of the sensor is about 400 ms, when RH jumps from 60 to >90%. The method used in this experiment to provide a fast change in the humidity gives one low RH level ie room RH (60%) and one high RH level (>90%) so the time taken to stabilise the sensor reading for the higher RH can only be an estimate and cannot be found accurately by this experiment. The estimated recovery time (90% signal maximum to 10 % baseline) of the sensor is 500 ms, which decreases if a flow of dry air surrounds the sensor because the recovery time of a humidity sensor depends on how fast the water vapor is removed from the sensor, which in turn is proportional to the air flow surrounding the sensor.

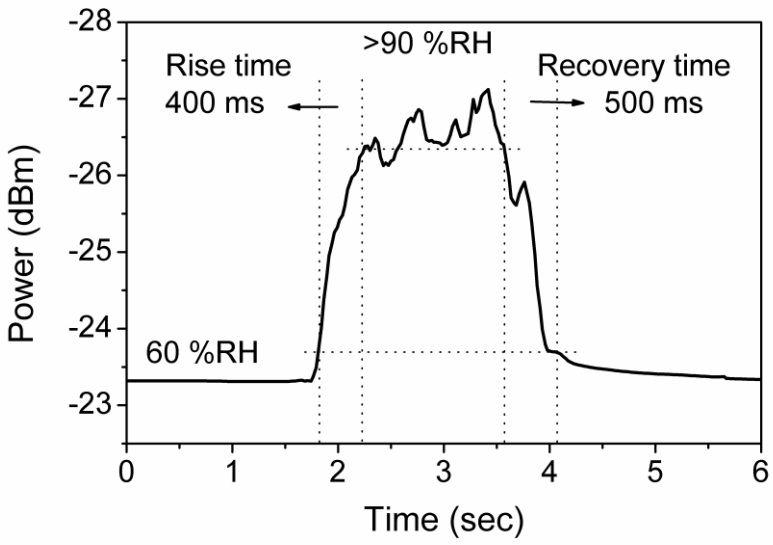

Fig. 4.7. Response time of the sensor.

4.2.5 Fabrication repeatability of the sensor

Finally the repeatability of sensor head fabrication is studied. It is important to note that a slight change in the sensor's length results in a small variation in the spectrum of a PCFI. In this experiment the control of the device's length was achieved by using a conventional fiber cleaver. Since the exact repeatability of the length is difficult with this method, the fabrication of a sensor with improved tolerance would require a modified cleaver with precise length control to set the length exactly. To determine how much the relative humidity response of the device varies with a 10 % change in PCFI length, a second Agarose infiltrated PCFI with a length circa 900 μm is fabricated. The infiltration length of the Agarose material within the sensor is ~100 μm. Fig. 4.8 shows the relative humidity response of the new device. The humidity response of the new device is different from the device with a 1 mm length, but there is still a strong variation in power level with RH evident and with an appropriate calibration each device can function effectively as a humidity sensor. Also for some possible applications such as breath rate monitoring this slight difference in humidity response is not a problem because only two states of humidity (room humidity level and a high humidity of > 90 %RH) need to be determined to measure the breathing rate.

Compared to the existing optical fiber based RH sensors, the sensor proposed in this chapter has the advantages of a very compact length, low cost and ease of fabrication. The end-type sensor head configuration offers advantages in terms of operating in environments which demand a compact probe and also reduced system complexity as only one interconnecting fiber is needed. Since the size of the actual sensor head is in micrometers, the reported sensor is suitable for sensing humidity in space constrained environments.

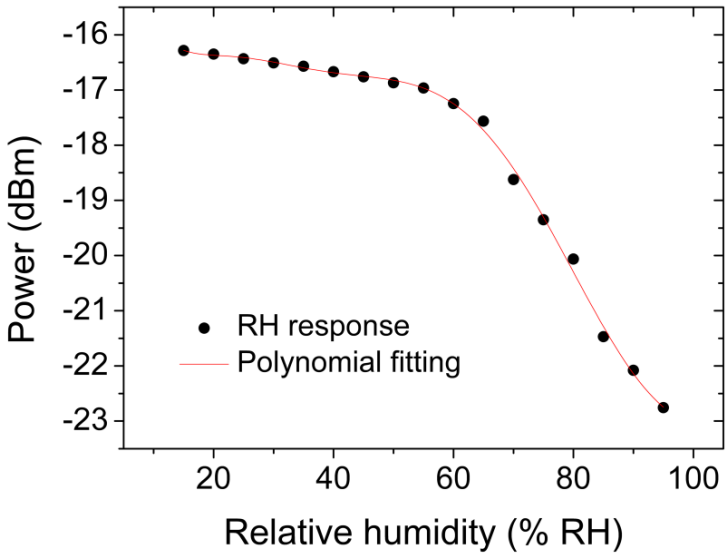

Fig. 4.8. Relative humidity response of the Agarose infiltrated PCFI with a length of 900 µm.

4.3. Simultaneous measurement of humidity and temperature using an Agarose infiltrated PCFI and FBG

Most of the sensors available on the market provide the humidity measurement values in relative humidity units. For a constant volume of air and at constant pressure if the temperature changes the RH will change even though the water vapor content of the air remains the same. Therefore a sensor for simultaneous measurement of humidity and temperature is an important requirement for a variety of applications including meteorological services, the chemical and food processing industries, fruit and vegetable storage, comfort systems for indoor environmental control, electronic processing, pulmonary diagnosis and fuel cells. Because of their unique advantages several sensors capable of simultaneous measurement of temperature and humidity based on an optical fiber have been reported to date: a sensor head composed of a cholesteric liquid crystal cell and a corner cube prism coated with cobalt chloride [4], a

sensor head composed of a fiber Bragg grating and a low-finesse Fabry–Perot interferometric cavity [5], a sensor comprising of two Bragg gratings recorded in silica and polymer fiber [6], a sensor based on an etched fiber, polymer-coated FBG and uncoated FBG [7] and a sensor based on a SiO_2 -nanospheres film deposited on a long-period grating in-line with a fiber Bragg grating [8]. In this section a novel fiber optic sensor design for simultaneously measuring temperature and relative humidity is proposed. The device is composed of an FBG and an Agarose infiltrated photonic crystal fiber interferometer (AI-PCFI) where the AI-PCFI is used to monitor the RH and an in-line FBG is used to monitor the temperature. The sensor proposed in this section offers a high RH sensitivity, equal or better temperature sensitivity and minimal cross sensitivity compared to other reported sensors.

4.3.1. Operating principle of the hybrid sensor

The use of an AI-PCFI for sensing is demonstrated in section 4.2 and the sensing mechanism of the FBG is well known [9]. The hybrid sensor reported here is formed from the in-line combination of an FBG and an AI-PCFI and is implemented as follows. Optical radiation from a broadband source is inputted into the combined FBG and AI-PCFI sensor head (as shown in Fig. 4.9). The FBG reflects optical power with a reflection maximum centered at the Bragg wavelength. Monitoring this wavelength will allow temperature to be measured. The FBG also behaves as a stopband optical filter, so optical wavelengths outside of the Bragg grating window are transmitted with negligible attenuation and thus a portion of the broadband optical source power reaches the humidity sensor. The optical signal reflected by the AI-PCFI will change depending on the humidity level. The reflected optical power from the AI-PCFI again passes through the Bragg grating, this time in the opposite direction. The FBG passes the reflected signal with very low attenuation since this reflected signal matches the transmission

window of the Bragg grating. Therefore, by monitoring the reflected optical power it is possible to measure intensity changes corresponding to variations in the humidity. Thus in summary, the temperature may be measured by detecting the spectral shift in the central wavelength of the fiber Bragg grating spectrum in nanometers and the humidity may be independently measured by monitoring the reflected optical power in dBm.

4.3.2. Experimental investigation of the hybrid sensor and discussion

The hybrid sensor system is composed of a super luminescent diode (SLED) (COVEGA Corporation, SLD1005), a fiber optic coupler/circulator (FOC), the AI-PCFI (RH sensor), the FBG (temperature sensor) and an optical spectrum analyzer (OSA), as shown in Fig. 4.9. The fabrication process for the AI-PCFI is given in section 4.2 while the size of the fabricated AI-PCFI is similar to the sensor demonstrated in the section above. The dimensions are 1 mm length and 125 μm diameter; the length includes both the 250 μm hole collapsed region and approximately 100 μm long Agarose-infiltrated region. The calculated fringe spacing for the sensor is ~330 nm, therefore only a narrow sub-periodic part of the interference pattern could be observed in this experiment. The large fringe spacing of the AI-PCFI makes the selection of FBG wavelength trivial as the spectral width of the reflected FBG spectrum is much smaller than that of the interference pattern.

A commercial FBG (Alxenses Company Ltd.) with a centre wavelength (λ_B) of 1540 nm, 3 dB bandwidth of 0.5 nm and a reflectivity at Bragg wavelength larger than 70 % is used for temperature monitoring. One end of the FBG is spliced to the SMF side of the AI-PCFI and the other end is connected to the FOC as shown in Fig 4.9.

The performance of the fabricated FBG-AI-PCFI hybrid sensor is evaluated at normal atmospheric pressure by placing it in a controlled environmental chamber. First, the

humidity response of the hybrid sensor is studied at a constant temperature of 22 ^{O}C. Measurements for relative humidity values ranging from 20% to 95% are performed, and hybrid sensor output spectral data for different values of relative humidity in this range are shown in Fig. 4.10. In the region 2 where the different humidity curves overlap, it is noticeable that the reflected optical power at the Bragg wavelength is not affected by humidity changes. In contrast, in the regions 1 and 3 the reflected optical power changes as a function of the relative humidity. When humidity increases, analogously to Fig. 4.3 the interference pattern shifts to longer wavelengths. Therefore, the output power decreases for the sensor in the observed wavelength region, which is a sub-periodic portion of the interference spectrum. Spectral output data for region 3 for wavelengths slightly longer than the Bragg wavelength are shown in Fig. 4.11. An optical power variation of >7 dB was observed for a humidity change of 75%RH in region 3 of the sensor spectral response.

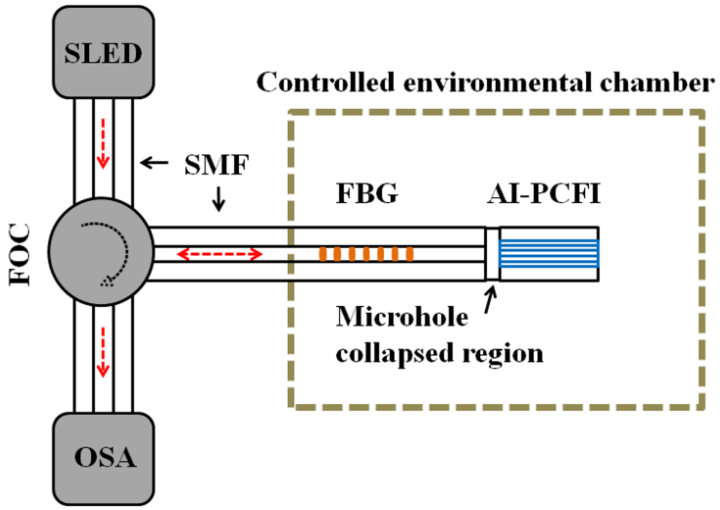

Fig. 4.9. Schematic diagram of the hybrid fiber optic sensor system for simultaneous measurement of RH and temperature (SLED- Super luminescent diode, FOC- Fiber optic circulator, SMF-Single mode fiber, FBG-Fiber Bragg grating, AI-PCFI-Agarose infiltrated-photonic crystal fiber interferometer, OSA-Optical spectrum analyser; dotted arrows represent the light path).

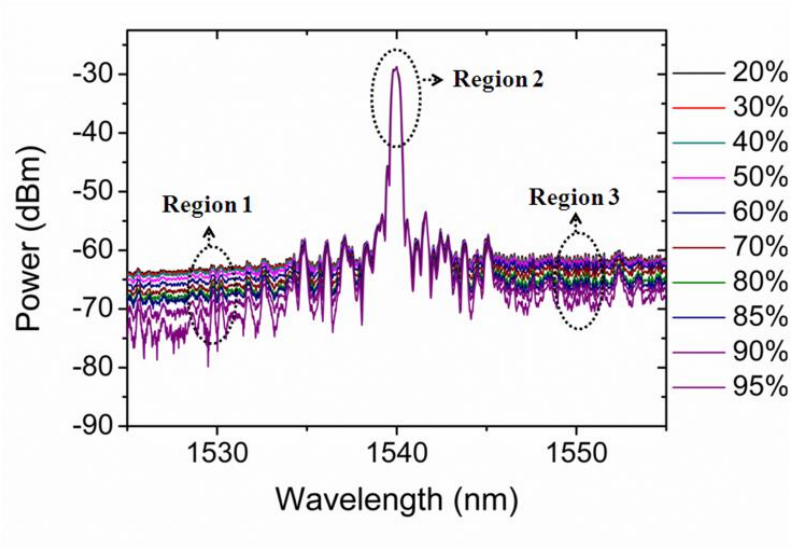

Fig. 4.10. Spectral response of the hybrid sensor at constant temperature and different RH.

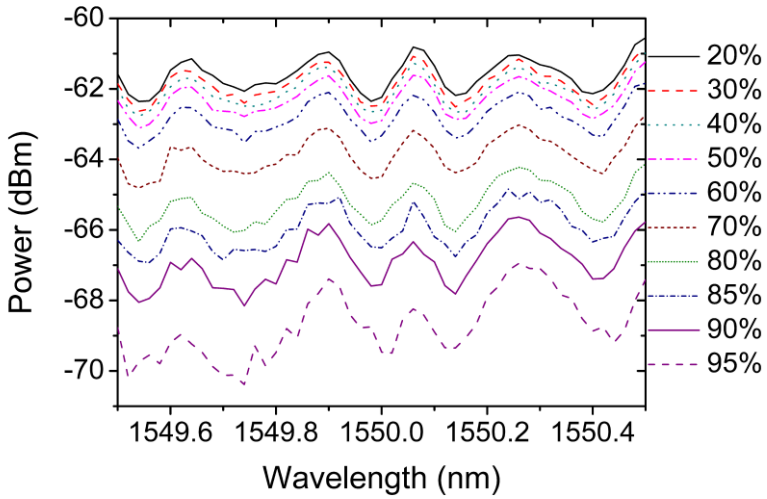

Fig. 4.11. Power variation of the hybrid sensor response in the region 3 of Fig. 4.10 at a constant temperature and different RH.

The temperature response of the hybrid sensor was also studied at a constant relative humidity (40 %) by varying the temperature from 10 to 45 ^{O}C and the result is shown in Fig. 4.12. In this case the Bragg wavelength shifts while the optical power levels in regions 1 and 3 are nearly constant. Fig. 4.13 shows a detail of the Bragg wavelength shift in region 2.

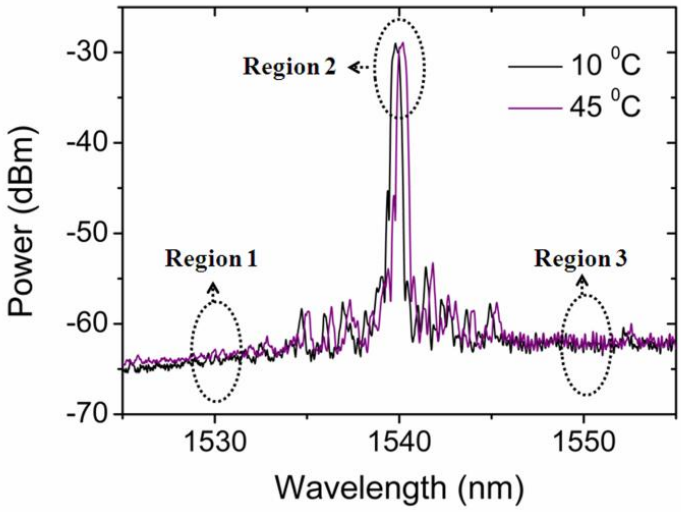

Fig. 4.12. The spectral response of the hybrid sensor at constant RH and different temperatures.

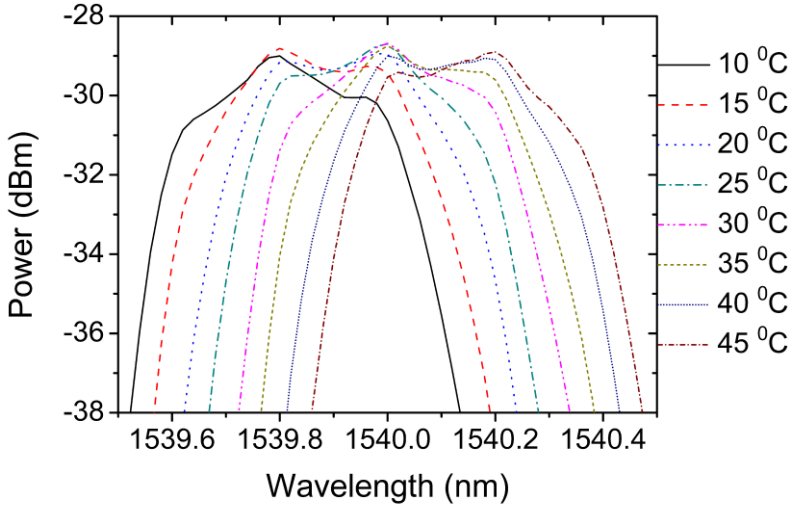

Fig. 4.13. Bragg wavelength shift of the hybrid sensor in the region 2 of the Fig. 4.12 at constant RH and different temperatures.

The cross sensitivity of the hybrid sensor to the measured RH and temperature is also studied. Fig. 4.14 shows the Bragg wavelength (λ_B) shift of the FBG for different temperatures and RH values. A temperature sensitivity of 9.8 pm/^{O}C and humidity sensitivity of 0.3 pm/%RH are observed. The small cross sensitivity to RH observed in the FBG response is most likely due to its polyimide coating. It has been shown in [6-8,

10-15] that a polyimide recoated FBGs are slightly RH sensitive. Therefore the sensitivity of the FBG to RH could be avoided by using an uncoated FBG.

The sensor power variation in region 3 (@ 1550 nm) of its spectral response for different temperatures and RH values is shown in Fig. 4.15. The RH response is non-linear and the humidity sensitivity is higher at higher RH values. At a wavelength of 1550 nm a power variation of >7dB for an RH change of 75% is observed with a humidity sensitivity of 0.026 dB/%RH and 0.163 dB/%RH in the RH ranges 20-60 % and 60- 95 % respectively. The temperature dependence of the AI-PCFI is also studied at a constant RH value of 40%. The temperature response of the sensor observed at a wavelength of 1550 nm is shown in Fig. 4.15. The response is slightly non-linear due to the shift of the FBG side lobes. A change in the reflected power of about 0.65 dB is estimated for a temperature variation of 30 ^{O}C equivalent to a temperature sensitivity of 0.02 dB/^{O}C. Since the PCF is made of a single material - silica, the PCFI itself is almost temperature independent [16]. Therefore, this small power variation of 0.02 dB/^{O}C is attributed to the temperature dependence contributed by Agarose. The experimental results indicate that the FBG element in the sensor has very low sensitivity to RH, and the reflected optical power from the AI-PCFI, shown in region 1 and 3 is sensitive to RH and has only very low sensitivity to temperature. In summary, due to the minimal cross sensitivity between the two measurands, by applying suitable signal processing the sensor demonstrated here can be used for simultaneous measurement of temperature and RH.

In addition in this sensor the maximum power reflected by the Bragg grating also provides a relative power reference and thus can be used to ensure independence of the measured intensity changes from the source power fluctuations caused by source power variations and changes in the path attenuation in interconnecting fibers. As result the

difference between the reflected optical power in region 2 and region 1 or 3 is a function of the humidity and is not affected by undesirable and uncontrollable losses or variations along the optical path between the optical source and the sensor.

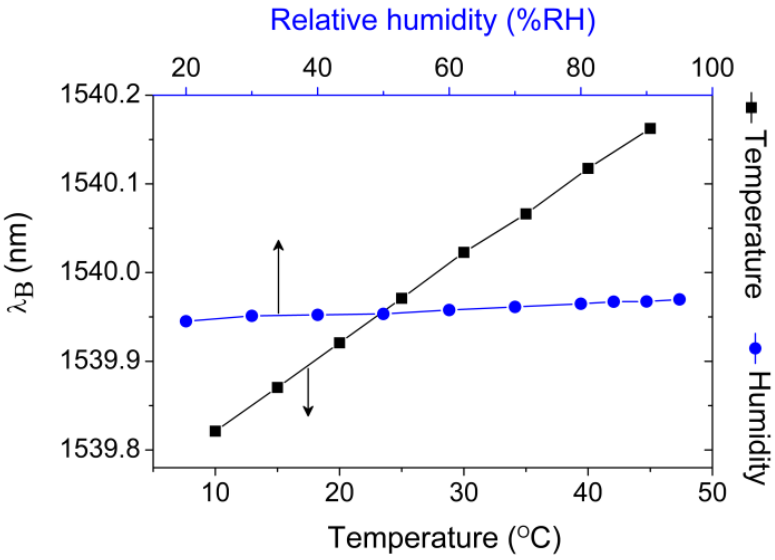

Fig. 4.14. Cross sensitivity of the hybrid sensor in terms of Bragg wavelength (λ_B) at different temperature and RH.

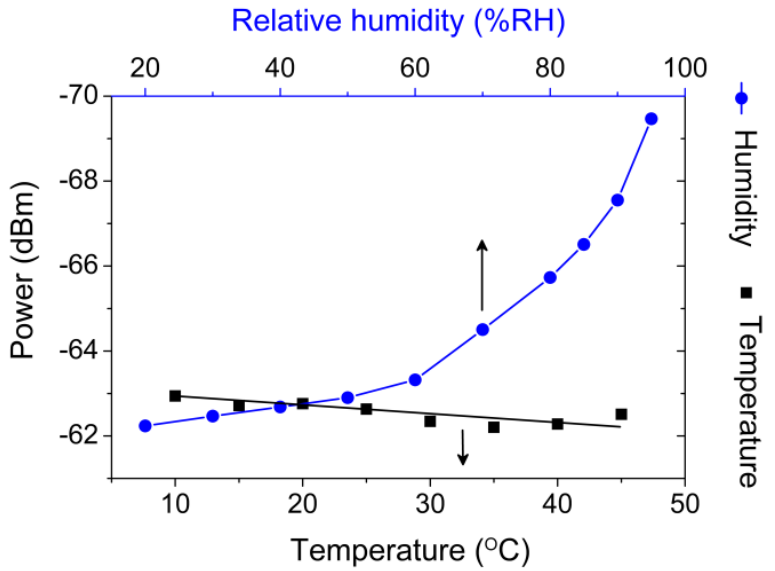

Fig. 4.15. Cross sensitivity of the hybrid sensor in terms of the sensor power variation at 1550 nm for different temperature and RH.

Compared to the existing optical-fiber-based RH and temperature hybrid sensors, the sensor proposed here has the advantages of a high RH sensitivity, minimal cross sensitivity, fast response time (estimated response time of this sensor is less than a second) and ease of fabrication. The end-type sensor head configuration offers advantages in terms of operating in environments, which demand a compact probe-type sensor and also reduced system complexity as only one interconnecting fiber is needed. The diameter of the dual sensor head is 125 μm and the length is in centimeters, so the sensor is suitable for sensing humidity and temperature in space constrained environments. A possible cost effective solution to replace the OSA in the sensor system is the use of suitable wavelength dependant optical filters (eg: arrayed waveguide demultiplexer) and photo detectors. This also potentially allows for multiplexing of several sensors within a single optical fiber network.

4.4. Summary

This chapter demonstrated a novel RH sensor based on an Agarose infiltrated PCFI. The sensor shows a sensitivity of 0.06 dB/%RH in the range 14-86 %RH and 0.6 dB/%RH in the range 86-98 %RH. The sensor response is found to be repeatable with good long term stability. The size of the sensor is 1 mm in length and 125 μm in diameter. The thermal sensitivity of the sensor is 0.066 dB/^{O}C. The study on the fabrication repeatability of the sensor shows a good repeatability of the sensor characteristics. The observed fast response time of 400 ms suggests that the sensor can potentially be used as a human breath rate monitor in a clinical environment. For example, a fiber optic humidity sensor is suitable as a breathing monitor for patients during an MRI scan because of its immunity to magnetic field interference.

A novel fiber optic hybrid device for simultaneously measuring temperature and relative humidity is experimentally demonstrated in this chapter. A reflection type photonic crystal fiber interferometer infiltrated with humidity sensitive material Agarose acts as the RH sensor and an in-line FBG is used to monitor the temperature. The sensor showed a temperature sensitivity of 9.8 pm/^{O}C and an optical power variation of >7 dB for an RH change of 75 %. The minimal cross sensitivity of the sensors suggests that by applying suitable signal processing the sensor proposed and demonstrated here can be used for simultaneous measurement of temperature and RH.

4.5. References

1. K. J. Lee, D. Wawro, P. S. Priambodo, and R. Magnusson, Agarose-gel based guided-mode resonance humidity sensor, *IEEE Sens J*, 7(3), pp. 409-414, (2007).
2. R. S. Moshrefzadeh, M. D. Radcliffe, T. C. Lee, and S. K. Mohapatra, Temperature dependence of index of refraction of polymeric waveguides, *J. Lightwave Technol.*, 10(4), pp. 420-425, (1992).
3. S. N. Kasarova, N. G. Sultanova, and I. D. Nikolov, Temperature dependence of refractive characteristics of optical plastics, *J. Phys.: Conf. Ser.*, 253(1), Article ID 012028, 6 pages, (2010).
4. M. Kawamura, T. Takeuchi, H. Fuad, and S. Sato, Humidity and temperature sensing using an optical fiber and a corner cube prism, *Jpn. J. Appl. Phys., Part-1*, 38, pp. 849–850, (1999).
5. F. J. Arregui, I. R. Matías, K. L. Cooper, and R. O. Claus, Simultaneous measurement of humidity and temperature by combining a reflective intensity-based optical fiber sensor and a fiber Bragg grating, *IEEE sensors journal*, 2(5), pp. 482-487, (2002).

6. C. Zhang, W. Zhang, D. J. Webb and G. D. Peng, Optical fiber temperature and humidity sensor, *Electronics letters*, 46(9), pp. 643-644, (2010).
7. N. A. David, P. M. Wild, J. Jensen, T. Navessin, and N. Djilali, Simultaneous in situ measurement of temperature and relative humidity in a PEMFC using optical fiber sensors, *J. Electrochem. Soc.*, 157, pp. B1173–9, (2010).
8. D. Viegas, M. , J. Goicoechea, J. L. Santos, F. , F. Arregui, and I.R. Matias, Simultaneous measurement of humidity and temperature based on an SiO_2 -nanospheres film deposited on a long-period grating in-line with a fiber Bragg grating, *IEEE Sensors Journal*, 111, pp. 162-166, (2011).
9. K. O. Hill and G. Meltz, Fiber Bragg grating technology-Fundamentals and overview, *J. Lightwave Technol*., 15, pp. 1263-1275, (1997).
10. P. Giaccari, H. G. Limberger, and P. Kronenberg, Influence of humidity and temperature on polyimide-coated fiber Bragg gratings, in Proc. Trends in Optics and Photonics Series: Bragg Gratings, Photosensitivity, and Poling in Glass Waveguides, Washington DC, 61, pp. BFB2, (2001).
11. P. Kronenberg, P. K. Rastogi, P. Giaccari, and H. G. Limberger, Relative humidity sensor with optical fiber Bragg grating, *Opt. Lett*. 27, pp.1385-1387, (2002).
12. T. L. Yeo, T. Sun, K. T. V. Grattan, D. Parry, R. Lade, and B. D. Powell, Polymer-coated fiber Bragg grating for relative humidity sensing, *Sensors Journal, IEEE*, 5(5), pp.1082-1089, (2005).
13. T. L. Yeo, T. Sun, K. T. V. Grattan, D. Parry, R. Lade, and B. D. Powell, Characterisation of a polymer-coated fiber Bragg grating sensor for relative

humidity sensing, *Sensors and Actuators B: Chemical*, 110(1), pp.148-156, (2005).

14. X. F. Huang, D. R. Sheng, K. F. Cen, and H. Zhou, Low-cost relative humidity sensor based on thermoplastic polyimide-coated fiber Bragg grating, *Sensors and Actuators B: Chemical*, 127(2), pp.518-524, (2007).
15. N. A. David, P. M. Wild, and N. Djilali, Parametric study of a polymer-coated fiber-optic humidity sensor, *Meas. Sci. Technol*., 23, 035103 (8pp), (2012).
16. J. Mathew, Y. Semenova, and G. Farrell, Photonic crystal fiber interferometer for humidity sensing, in *Photonic Crystals - Introduction, Applications and Theory*, A. Massaro, Ed. InTech, 2012, chapter 8.

CHAPTER 5. RELATIVE HUMIDITY SENSOR BASED ON AN AGAROSE COATED PHOTONIC CRYSTAL FIBER INTERFEROMETER

5.1. Introduction

Among the different configurations of photonic crystal fiber interferometers (PCFI) fabricated via microhole collapse [1-10], a reflection type PCFI which was demonstrated for relative humidity (RH) sensing in the previous chapters offer some unique advantages such as the absence of the need for hygroscopic materials or miniature size etc. A transmission type PCFI in which the two ends of a PCF are fusion spliced to lead-in and lead-out single mode fibers has already been demonstrated for strain [3,4] and refractive index (RI) [5,6] sensing. In this chapter a transmission type PCFI is investigated for RH sensing given that it has advantages compared to a reflection type PCFI: the microholes of a transmission type PCFI are not exposed to the environment so the contamination by micro dust particles is eliminated and a transmission type PCFI does not require a circulator for interrogation.

The aim of this work is (1) to study the effect of the hygroscopic Agarose coating thickness on the RH sensitivity, and (2) to demonstrate a high sensitivity RH sensor based on the transmission type PCF interferometer. To study the effect of the Agarose coating thickness on the RH sensitivity initially several PCFI devices with the same length but different coating thicknesses are fabricated and their individual humidity response is studied. Influence of both the thickness change and RI change of the coating with respect to an RH change on the spectrum of the device is investigated. To achieve a higher RH sensitivity for the Agarose coated PCFI, an interferometer with large fringe

spacing is fabricated. A coating thickness for this device is selected such that its effective RI is in the high RI sensitivity region of the device. The RH response of the sensor is investigated. Furthermore a detailed study of the sensor performance in terms of its sensitivity, repeatability and long term stability, time response and temperature dependence are carried out. The work carried out in this chapter also can be applied to sensors based on optical fibers coated with other materials for the selection of a suitable operating point in terms of sensitivity and range of operation.

5.2. Fabrication and operating principle of a transmission type PCFI for RH sensing

The transmission type PCFI in the experiment is fabricated by fusion splicing a length of commercial PCF (LMA-10, NKT Photonics) between standard optical fibers with a conventional splicing machine. Two regions with PCF hole-collapse are thus required, using the splicing technique detailed in section 3.2.2 of chapter 3, and as a result the voids of the PCF are sealed after fabrication of the PCFI, preventing contamination by dust particles. In addition, since the device is a transmission type sensor, it does not require the use of a fiber optic circulator. To understand how this interferometer works it is useful to analyze the guided beam when it travels from the input SMF to the PCF and then from the PCF to the output SMF (Fig. 5.1). As with the reflection type PCFI, the fundamental SMF mode experiences diffraction and broadening in the entry hole-collapsed region, which causes two modes (a core and a cladding modes) to propagate and interfere in the PCF section. However, in contrast to the reflection-type PCFI where both modes experience reflection at the end of PCF section, in the transmission-type PCFI there is an exit microhole-collapsed region and an output SMF where the output SMF acts as a spatial filter and picks up only a part of the resultant intensity distribution of the interference pattern in the PCF. Thus the optical power coupled to the output

SMF displays maxima and minima at certain wavelengths of the input light. The positions of these minima and maxima on the wavelength axis depend on the interference conditions for the core and cladding modes, such as the geometry of the sensor and its surrounding RI, which in turn allows the structure to be used for sensing. For RH sensing, the surface of the interferometer is coated with Agarose whose refractive index will change with respect to humidity. Only the cladding mode interacts with the coating, since the core mode is isolated from the external environment. The Agarose coating changes the effective index of the cladding mode with respect to RH and consequently the phase difference between the interfering cladding modes and the core mode results in a shift in the interference pattern. An increase in the effective RI of the cladding mode causes a spectral red shift and a decrease in the effective RI causes a blue shift.

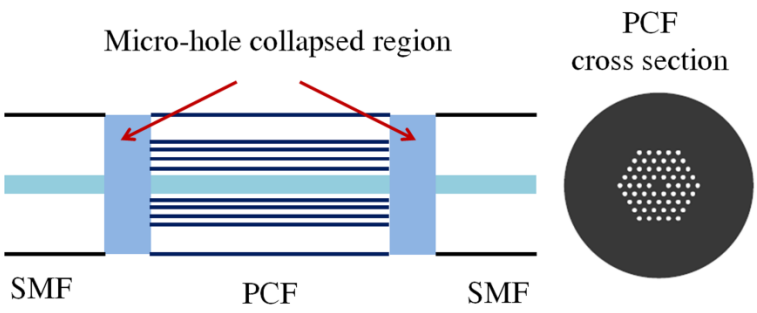

Fig. 5.1. A drawing of the transmission type PCF interferometer and a diagram of the cross section of the PCF employed. (SMF- single mode fiber, PCF- photonic crystal fiber).

5.3. PCF length vs fringe spacing of a transmission type PCFI

Unlike the reflection type PCFI where the light is passing through the PCF twice, for a transmission type PCFI the light is passing through the PCF only once so it is important to point out that the variable L used in the expressions to explain the working principle

of the PCFI should be replaced with L/2 for a transmission type PCFI used in this chapter. So the expression for the period/ fringe spacing of a transmission type PCFI is,

$$P \approx \frac{\lambda^2}{\Delta n L} \tag{5.1}$$

where Δn is the difference between the effective RI of core and cladding modes, λ the wavelength of the optical source, and L the physical length of the PCFI [5]. In order to verify this expression and to calculate the value of Δn, ten PCFIs were fabricated with lengths ranging from 10 mm to circa 100 mm and their spectra are studied. As an example Fig. 5.2 shows the measured transmission spectra of four PCFIs in the 1500-1600 nm wavelength range with lengths of 100, 40, 20 and 10 mm. The transmission spectra of the interferometers exhibit regular interference patterns with a period or fringe spacing inversely proportional to the length of the PCF section.

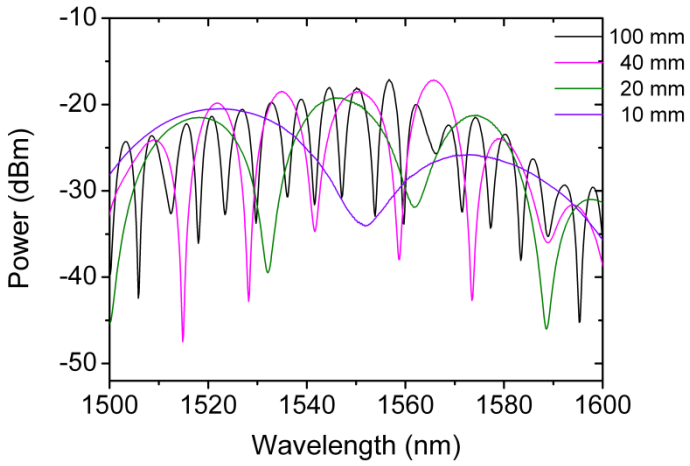

Fig. 5.2. The transmission spectra of interferometers with L = 100 mm, 40 mm, 20 mm and 10 mm in the wavelength range of 1500-1600 nm.

Fig. 5.3 shows the measured fringe spacing or periods of the fabricated PCFIs as a function of length of the PCF section. The measured periods agree well with the expected ones for a two-mode interferometer given in equation (5.1). The value of Δn

obtained based on the experimental data is ~4x10^{-3} where the source wavelength is assumed as 1550 nm and the ambient medium as air.

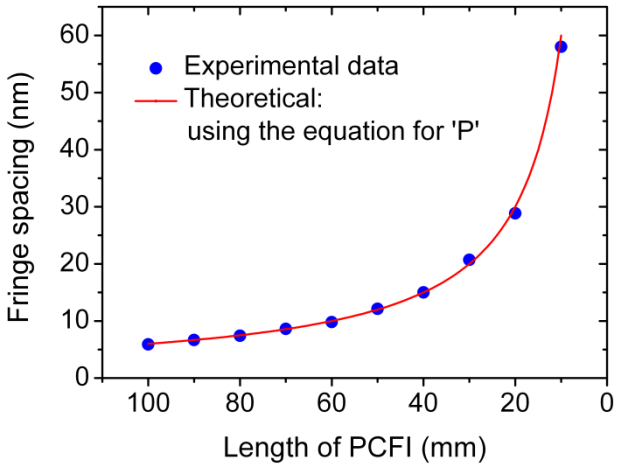

Fig. 5.3. The fringe spacing as a function of length of PCF observed for a transmission type interferometer.

5.4. Effect of coating thickness on the sensitivity of a RH sensor based on an Agarose coated photonic crystal fiber interferometer

In order to study the effect of coating thickness on the sensitivity of an RH sensor based on an Agarose coated PCFI, four identical PCFI devices with a PCF length of 40 ±0.015 mm and fringe spacing of 14.8 ±0.22 nm are fabricated. The transmission spectra of these PCFIs are shown in Fig. 5.4. The similarity of spectra obtained for different devices confirms the very good fabrication repeatability for the interferometer. The response of these PCFIs to external RI variations is studied by immersing the devices in different calibrated RI solutions, over an RI range from 1.33 to 1.45. It is observed that for the same change in RI, the shift in the individual peaks of the interference pattern varies slightly. To avoid ambiguity in determining the sensitivity, the average peak shift of the sensor response is calculated at each RI value over the wavelength range observed. Fig. 5.5 shows the average spectral peak shift of the device

with respect to external RI. As expected all the devices showed very similar RI responses. It is also observed that as expected the RI sensitivity of the interferometer is higher in the region close to the RI of the PCF material, this is, silica (n_D ~1.45).

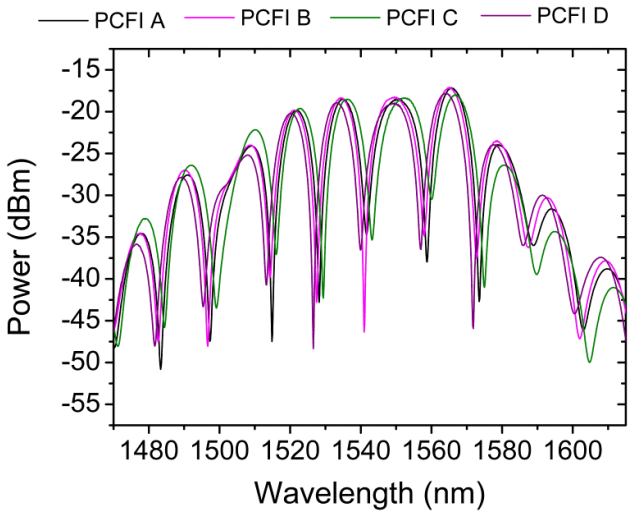

Fig. 5.4. Transmission spectra of different PCFIs with lengths of 40±0.015 mm.

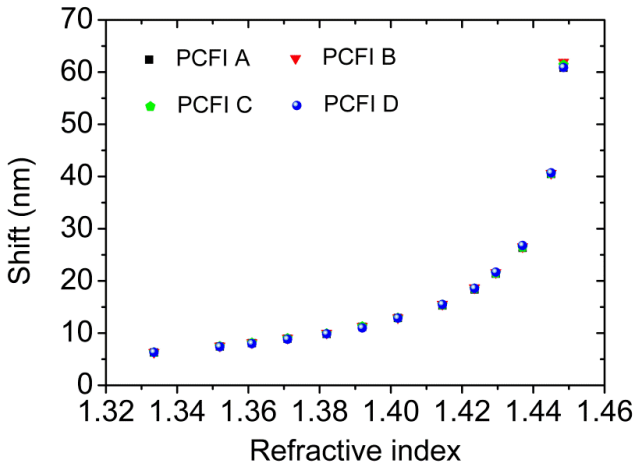

Fig. 5.5. Response to the ambient refractive index changes for different PCFI samples.

Coating with Agarose is carried out by drawing the interferometer through a hot (65 ^{O}C) Agarose solution [11]. A schematic diagram of the experimental setup for Agarose coating is shown in Fig. 5.6. The solution is prepared by dissolving 1 wt% Agarose in

distilled water. In order to undertake the coating process the fiber is fixed straight and horizontally above a translation stage. Below the fiber a heater is fixed on a translation stage. A small container placed at the top of the heater is filled to the rim of the container with a hot Agarose solution. Because of surface tension the surface of the solution forms a dome-like shape which projects slightly above the rim of the container. The position of this container can be adjusted to allow the fiber to pass through this dome of the Agarose solution. The temperature of the heater is set at 65 ^{O}C. The fiber is drawn through the hot Agarose solution using a translation stage which is software-controlled using a computer. This arrangement allows for good repeatability of the coating parameters.

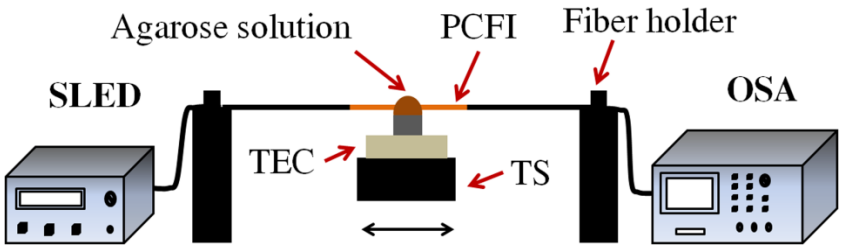

Fig. 5.6. Schematic diagram of the experimental setup for Agarose coating. (SLED-super luminescent diode, TEC- thermo electric cooler, TS- translation stage, OSA-optical spectrum analyzer, PCFI- photonic crystal fiber interferometer).

A desired coating thickness can be achieved using this setup by varying the drawing speed of the fiber through the solution or by passing the fiber multiple times through the solution. Practically the latter technique is found to be best in order to achieve a repeatable thickness. Thus in the experiment the fiber is drawn through the solution multiple times but with a constant speed of 5 mm/sec. Accurate measurement of the film thickness during the coating process is difficult due to the fiber geometry and thus in the experiment the device's spectrum is monitored each time the fiber passes through

the solution. The observed shift in the interference spectrum confirms the formation of a coating on the PCFI as it is in agreement with the expected red shift of the PCFI response with an increase in ambient RI for the interferometer (Fig. 5.5).

The repeatability of the Agarose coating layer formation is studied using five PCFI devices with a similar length and passing the devices through the solution a constant number of times. The spectral shift of the devices obtained for a single pass of the fiber through the solution is shown in Fig. 5.7(a). The average spectral shifts observed are in the range from 1.25-2.5 nm. The spectral shift of the devices obtained for a double pass of the fiber through the solution is shown in Fig. 5.7(b). The average spectral shifts observed are in the range from 2.85-10.95 nm. Also it is found that during the multi pass process, for some cases the shift is observed to be close to zero. This study shows that passing the fiber through the Agarose solution a fixed number of times does not ensure that an exact required coating thickness is achieved and it is necessary to always monitor the spectral shift during the coating process to achieve an exact spectral shift/thickness/RI for the coating.

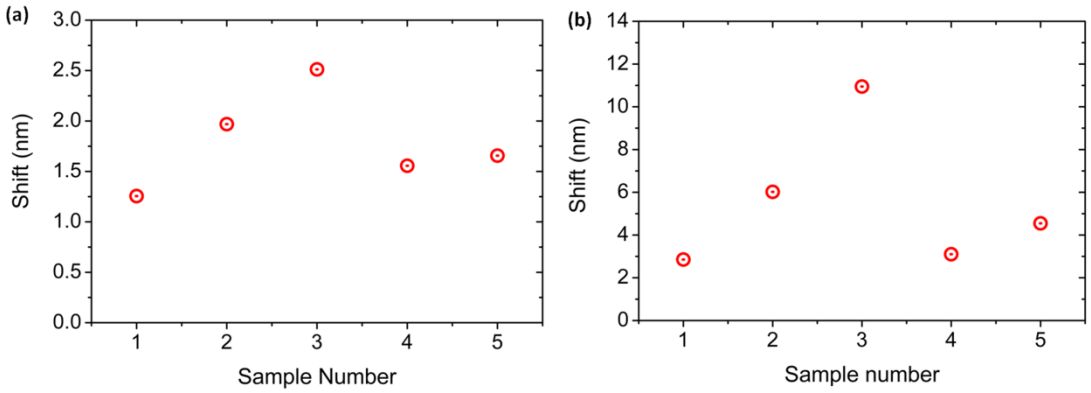

Fig. 5.7. Spectral shift of different devices obtained (a) after single pass of the fiber through the solution (b) after double pass the device through the solution.

To study the influence of the Agarose film thickness on the properties of the PCFI the four PCFI devices (A, B, C, D) previously fabricated are coated with different thicknesses of Agarose film by passing the fiber through the solution multiple times simultaneously monitoring the spectral shift of the coated device. In the case of device A the coating process is stopped when the average peak shift reaches a value of 2.3 nm and for devices B, C and D the coating process is stopped when the shift reaches 3.55 nm, 14.5 nm and 26.6 nm respectively.

The parameters of all four Agarose coated photonic crystal fiber interferometer (AC-PCFI) devices are listed in Table 5.1. The spectral peak shifts are calculated as the average difference in the peak positions for all the individual peaks in the transmission spectrum for each device before and after coating it with Agarose. The effective refractive index of the coating is estimated using the peak shift data obtained from the studies of the PCFIs response to changes in ambient RI (Fig. 5.5). The thickness of the coated device is estimated using an optical microscope at a room RH of 60±2%. From the data shown in the Table 5.1 it is obvious that when the coating thickness increases, the effective RI of the coating experienced by the cladding mode of the PCFI increases.

Table 5.1. Parameters of the different AC-PCFI devices at ~60 % RH

AC-PCFI	Average red peak shift of the coated PCFI relative to the uncoated PCFI (nm)	Refractive index of coating (deduced from the RI response of the PCFI)	Estimated thickness of coating (±100 nm) in nm
A	2.3	1.24	250
B	3.55	1.28	400
C	14.5	1.408	800
D	26.6	1.437	1250

The RH responses of the AC-PCFI devices are studied by placing them inside a controlled environmental chamber (Electro Tech Systems inc., Model 5503-00 with Package F) as shown in Fig. 5.8. The ambient temperature during the study was set at 24 ±1 ^{O}C at normal atmospheric pressure.

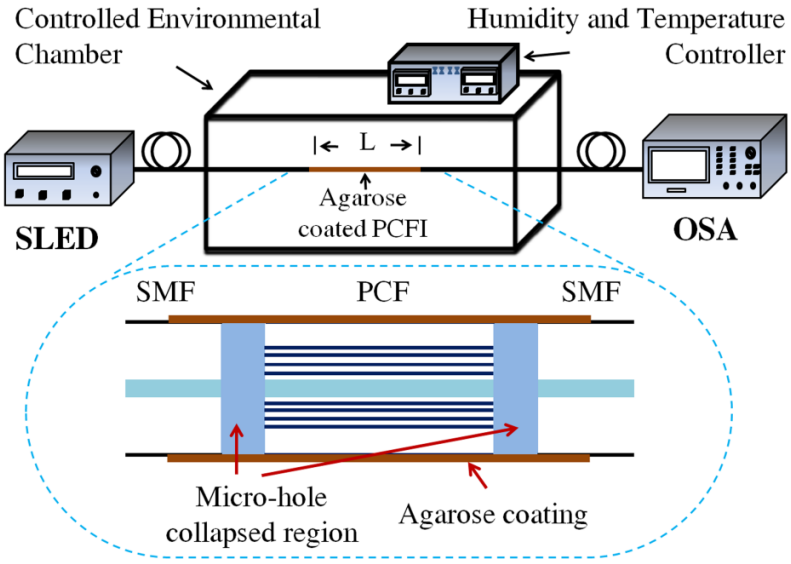

Fig. 5.8. Schematic diagram of the experimental setup to study the sensor's response to humidity changes. Inset: a diagram of the Agarose coated interferometer, (SLED- super luminescent diode, OSA- optical spectrum analyzer, SMF- single mode fiber, PCF- photonic crystal fiber, PCFI- photonic crystal fiber interferometer).

Previously reported studies on humidity sensing based on the use of Agarose coatings considered only the bulk RI change of the coating induced by changes in ambient RH. It should be noted however that there exists some conflicting evidence in the literature regarding the refractive index change of an Agarose coating with respect to RH [9, 11-17]. The study presented in this chapter gives further insight into the behaviour of an Agarose coating with the change of ambient RH.

It is well known that the thickness of a hygroscopic coating can be affected by ambient RH, to verify this for the coated PCFIs, the thickness of the Agarose layer for each of

the fabricated PCFI devices at different RH conditions was estimated using an optical microscope. Fig. 5.9 shows the changes in thickness of the Agarose coating for all four studied PCFIs at two values of RH: room RH of 60±2 % and a higher RH of >90 %. It is observed that as expected the thickness of the coating increases significantly (> 60%) when RH increases from ~60 % to >90 % RH. Physically when the RH level increases, more water molecules are diffused into the Agarose coating, resulting in the inflation of the Agarose and increase in the thickness of the coating. Similar to any other swelling polymer an increase in water content will decrease the bulk refractive index of the Agarose coating, in accordance with the Lorenz- Lorentz relation [18].

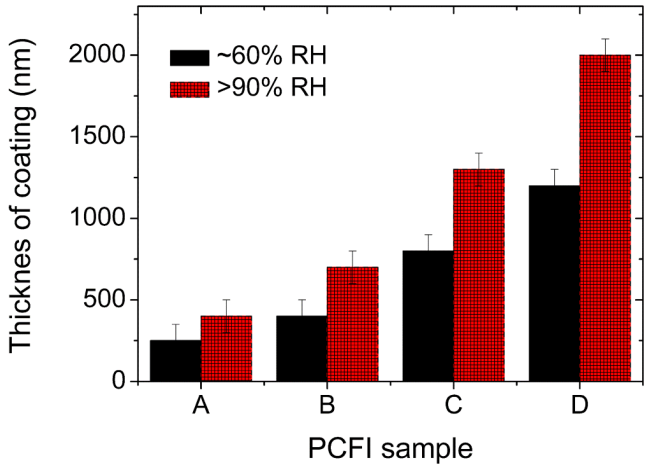

Fig. 5.9. The estimated thickness of the four different AC-PCFI devices at room RH of ~60 % and at a higher RH of >90%.

It has been shown in [6,19] that for fiber devices with coatings of sub-micron thickness as the thickness of the coating increases the effective RI experienced by the cladding mode increases even though the bulk RI of the coating is a constant. This effect is also confirmed by the data in Table 5.1 which illustrates the increase in the refractive index of the coating with the increase of the coating thickness. The data are taken at a fixed

ambient RH and therefore the increase of the RI can only be attributed to the increased thickness of the Agarose coating layer.

It can be thus be concluded that when ambient RH changes two factors alter the effective RI of the cladding mode: the bulk RI change of the coating and the thickness change of the coating. When the RH increases the decrease in the bulk RI of the coating causes a blue shift to the interference spectrum while the increase in the thickness of the coating causes a red shift to the interference spectrum.

It is found that for coatings of thickness less than the penetration depth of the evanescent part of the cladding mode, which is normally significant up to one third the wavelength of the propagating light [20-21], the increase in the effective RI as a result of the increase in the thickness of the Agarose dominates and is more significant than the effect of the bulk RI change, resulting in a net red shift of the interference spectrum for all RH values. This is the case with the devices A and B in the experiment. Fig. 5.10(a) shows the average peak shift of the interference pattern for samples A and B with respect to RH. The peak wavelength shift shown is normalized with respect to the peak value at the lowest measured RH (25% RH). The AC-PCFI A shows a spectral red shift with an increase in RH and the observed shift is linear in the range from 25 to 90 % RH with a slope of 5 pm/%RH. Above 90 % RH the sensitivity of the device is much higher, most likely due to the water vapor condensation on the coating at these higher RH values. With an increase in humidity sample B shows a red shift with a slope of 9 pm/%RH in the range from 25 to 90 % RH. It can be concluded that when the thickness of the coating increases the humidity sensitivity of the AC-PCFI also increases. One possible reason for this behavior is that when the thickness of the coating increases, the effective RI of the coating then lies in the high RI sensitivity region of the PCFI (the

higher slope region in Fig. 5.5) and hence the change in the effective RI of the coating with respect to an RH change results in an increased spectral shift.

When the coating thickness is greater than the penetration depth of the evanescent wave part of the cladding mode, the effect of a bulk RI decrease with ambient RH dominates the effective RI experienced by the cladding mode. In the experiment it is observed that when the coating thickness is greater than ~800 nm, which is the case with AC-PCFI devices C and D, a blue shift of the interference spectrum of the AC-PCFI is observed with the increase of ambient RH. For verification of this result the evanescent wave penetration depth was calculated using equation (1) of reference [20] for device C at 60 % RH by setting the value of the RI of the silica as n_1= 1.44, the RI of the Agarose coating as n_2 =1.408 (Table 5.1) and assuming the angle of incidence at the fiber-coating interface $\theta = 90^O$. Using these values the calculated penetration depth is 817 nm, verifying the observation that the wavelength shift changes from a red to a blue shift when the coating thickness is in the region of 800 nm.

The humidity responses of the AC-PCFI devices C and D are shown in Fig. 5.10(b). The AC-PCFI C shows a spectral red shift when humidity increases from 25 % RH to 60 % RH and then it shows a blue shift on a further increase of RH from 60 % to 98 %. This is due to the fact that below 60% RH the thickness change factor dominates by comparison to the bulk RI change of the coating and above 60% RH the coating thickness is greater than the penetration depth of the evanescent wave portion of the cladding mode interacting with the coating so that the effective RI of the cladding mode is mainly determined by the bulk RI of the coating. For AC-PCFI D, the point on the RH axis at which the red shift changes to a blue shift, changes to a lower RH of 40% which is expected because here the coating is thicker than for sample C. For AC-PCFI D the RI of the coating is in a more RI sensitive region of the PCFI therefore the RH

sensitivity observed for this sample is higher compared to other devices with smaller thicknesses of Agarose coating. The AC-PCFI D shows a sensitivity of 64 pm/%RH in the region 25-40 % RH and -137 pm/%RH in the range 40-90 %RH. Assuming the OSA used for measurement has a wavelength resolution of 0.01 nm, the AC-PCFI D has a humidity resolution of 0.07% RH in the RH range from 40% to 90% RH.

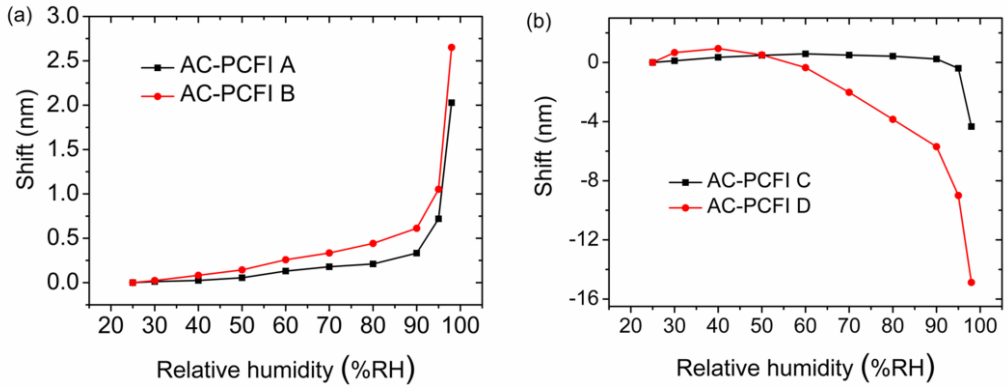

Fig. 5.10. (a) The average spectral peak shift for AC-PCFI samples A and B with respect to relative humidity. (b) The average spectral peak shift for AC-PCFI samples C and D with respect to relative humidity.

The calculated RH sensitivities of the AC-PCFI devices in different linear RH response regions are listed in Table 5.2, where the positive sensitivity values represent spectral red shift and negative values represent a blue shift. Above 90 % RH the response is nonlinear so the Table 5.2 shows the average sensitivity.

Table 5.2. RH sensitivity of AC-PCFI devices in different RH regions

AC-PCFI	A		B		C			D		
RH range (%RH)	25-90	90-98	25-90	90-98	25-60	60-90	90-98	25-40	40-90	90-98
Sensitivity (pm/%RH)	5	198	9	238	17	-11	-525	64	-137	-1100

Previously published studies on humidity sensing based on Agarose coated optical fibers do not give a clear picture of the refractive index change and the thickness change of Agarose coating with respect to RH. The results presented in this chapter reveal that there is a significant and complex dependence of the sensor response on the thickness of the coating. This result can potentially be applied to different types of coatings on a PCFI device which may result in improved sensors performance.

5.5. A high sensitivity humidity sensor based on an Agarose coated photonic crystal fiber interferometer

In the above section, the effect of Agarose coating thickness on the sensitivity of a RH sensor based on a PCFI is reported. It is found that the RH sensitivity of the sensor significantly depends on the thickness of the coating. The length of the PCF section used for the sensors in the above experiments was 40 mm with a fringe spacing of ~15 nm. It is difficult to monitor spectral shifts greater than the fringe spacing, which is problematic if the fringe spacing is relatively small. Monitoring spectral shifts is very important during the coating process in order to achieve highest RH sensitivity, where a shift of greater than 50 nm needs to be monitored. In addition the small fringe spacing limits the RH measurement range of such a sensor because a full RH range could give a spectral shift of greater than 55 nm.

As a starting point for a high sensitivity RH sensor, described in this section, a small length of PCF is selected for the interferometer so that the PCFI fringe spacing is large. As a result, larger spectral shifts can be monitored during the coating with Agarose, which allows one to obtain the value of the effective refractive index of the coating so that it lies in an RI region close to the RI of silica and therefore achieve the highest sensitivity for the PCFI device.

In order to achieve suitable large fringe spacing for the interferometer in this experiment a PCFI with a PCF length of 10 mm is fabricated. The corresponding fringe spacing of the device is 58 nm (Fig. 5.3). The optical bandwidth of the available source used for interrogation is 54.5 nm which limits the minimum possible length of PCF for the sensor because a fringe spacing greater than 58 nm would be difficult to monitor with this optical source.

For the selection of a suitable coating thickness with effective refractive index in the higher RI sensitivity region of the PCFI, initially the response of the device to external RI variations is studied by immersing the device in different calibrated RI solutions, over an RI range from 1.33 to 1.45. Fig. 5.11 shows the spectral peak shift of the device with respect to external RI. As discussed earlier RI sensitivity of the interferometer is higher in the region close to the RI of PCF material silica (n_D ~1.45). A coating thickness in the possible highest RI sensitivity region of the device is selected by comparing the spectral shift obtained during the coating process to the corresponding spectral shift of its RI response.

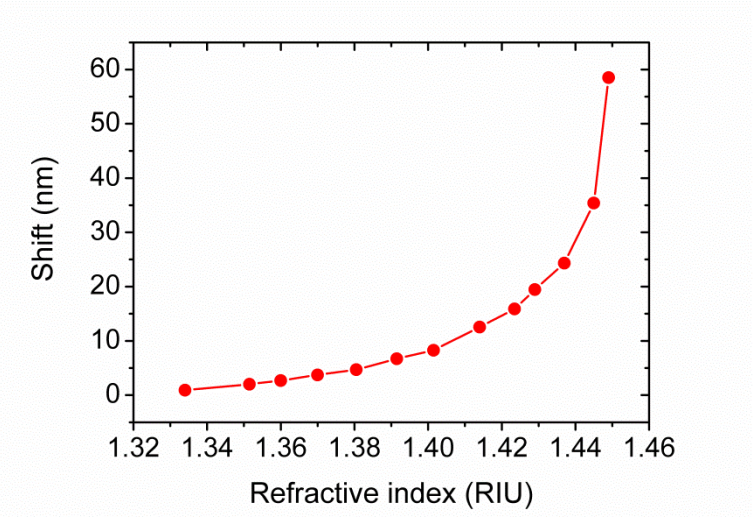

Fig. 5.11. Ambient refractive index response of the interferometer with a length of 10 mm.

Coating with Agarose is carried out by drawing the interferometer through a hot (65 ^{O}C) Agarose solution as explained above in this chapter. In the experiment the desired coating thickness is achieved by passing the fiber multiple times through the solution with a constant speed of 5 mm/sec. From Fig. 5.11 it is known that maximum RI sensitivity is achieved for RI values close to 1.45. Thus the multipass process of building up layer upon layer of Agarose and thus increasing the effective RI of the layer is halted when the spectral shift reaches a value associated with an RI value of approximately 1.45, based on Fig. 5.11.

The Fig. 5.12 shows how the interference spectrum shifts as a function of the number of times the fiber passes through the solution, building up the Agarose coating layer with each pass. The observed shift in the interference spectrum confirms the formation of a coating on the PCFI as it is in agreement with the RI response of the PCFI where a red shift is observed for an increase in ambient RI (Fig. 5.11). In the experiment the coating process is stopped when the average peak shift reaches a value of 51.88 nm which corresponds to an RI value in the high sensitivity region of the PCFI. After processing, the coated PCFI is kept at room temperature for one day until it is partially dehydrated and reaches equilibrium with the ambient environment.

Table 5.3 gives the estimated parameters of the sensor at two RH values of 60% and 90%. These observations are in agreement with the results given above in this chapter and confirm that when RH changes the bulk refractive index of the Agarose decreases and the thickness of the coating increases. Since the coating thickness is greater than the penetration depth (~800 nm) of the evanescent wave part of the interfering cladding mode the effect of thickness change can be neglected and the coating is acting as a bulk material to the cladding mode. Therefore the bulk refractive index change of the coating determines the spectral shift with respect to RH.

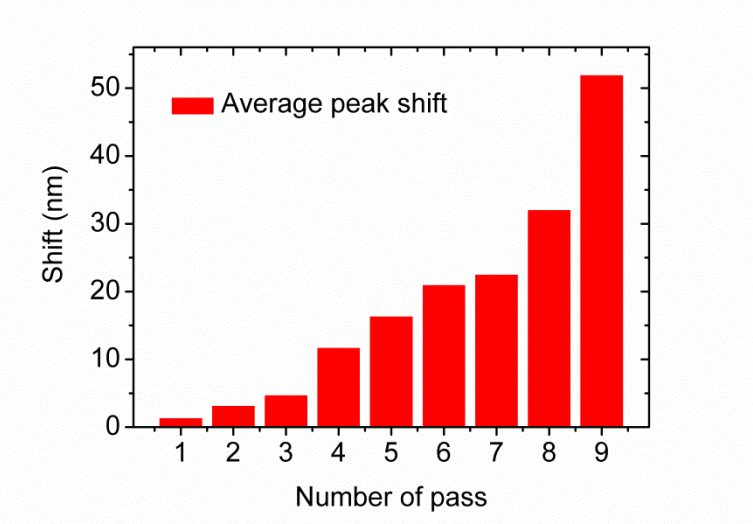

Fig. 5.12. Evolution of the Agarose coating layer is confirmed by the increase in spectral shift as the number of times the fiber passes through the solution increases.

Table 5.3. Parameters of the AC-PCFI device at two RH values

Relative Humidity (%)	Average red peak shift of the coated PCFI relative to the uncoated PCFI (nm)	Refractive index of coating (deduced from the RI response of the PCFI)	Estimated thickness of coating (±100 nm) in nm
60	51.88	1.446	1600
90	27.82	1.440	2700

Fig. 5.13 shows the changes in the device spectrum with respect to ambient RH. As RH increases from 40% to 98%, the interference spectrum of the device shifts to a shorter wavelength because the bulk RI of the Agarose decreases with RH. By monitoring the wavelength shift of the interference pattern, one can determine the ambient RH and its changes, assuming a suitable calibration has taken place.

It is clear from Fig 5.13 that for the same change in RH, the shift in the individual peaks of the interference pattern varies slightly. Thus a relatively better RH sensitivity can be achieved by monitoring the peak giving the maximum shift (the lower peak close to

1560 nm at 40% RH in the studied wavelength range 1470-1620 nm) for the sensitivity analysis. Fig. 5.14 shows this peak shift of the sensor with respect to RH. The error bars shown in Fig. 5.14 are calculated from the data obtained from six experimental measurements taken for the humidity response of the sensor. This error in measurements is found to be mainly due to the hysteresis observed for the forward and reverse response of the sensor. The hysteresis is mainly due to the difference in the time responses of the Agarose coating to an increase and decrease of RH where the recovery time (the time required to remove the water vapor from the bulk Agarose) is always greater than the response time (the time required to penetrate the water vapor and to reach the fiber surface). The limitation in the accuracy (±2% RH) of the chamber control system might also contribute to the observed hysteresis of the sensor.

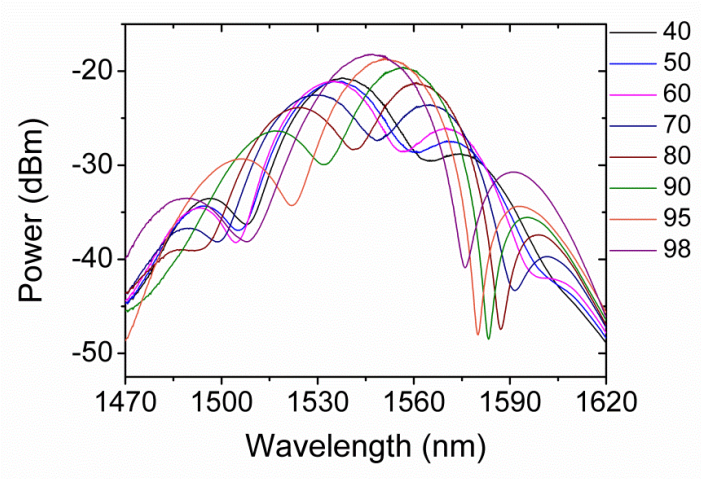

Fig. 5.13. The spectral responses of the sensor at different relative humidity values.

The total wavelength shift in the RH range from 40% RH to 98% RH for the sensor is circa 56 nm which is much higher compared to the wavelength shift of 16 nm obtained for a humidity change of 58 %RH in the case of the RH sensor (AC-PCFI D) demonstrated above in this chapter. Also this wavelength shift is higher than the reported highest sensitivity (a wavelength shift of 45 nm for an RH change of 60%) humidity sensor based on Agarose coated optical fiber devices [17]. The sensor

presented here is simple and gives a higher wavelength shift compared to the complex device used in [17] where a cladding etched multimode fiber hetero-structure coated with indium tin oxide and then with Agarose is used.

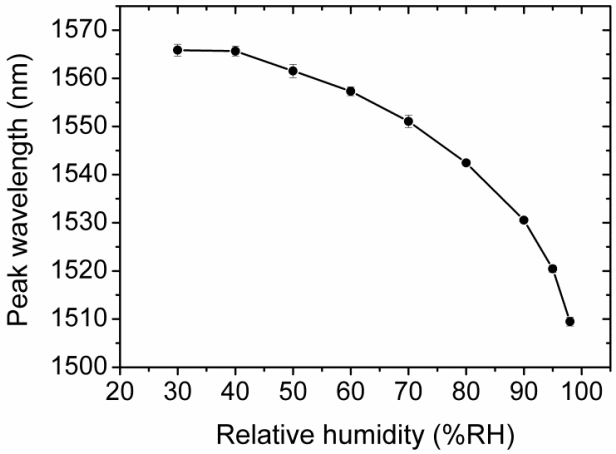

Fig. 5.14. Spectral peak shift versus ambient relative humidity (error bars shown are calculated from the data obtained from six experimental measurements).

Fig. 5.14 shows that the wavelength peak shift is more significant at higher humidity values. The average peak shift is linear in the range 40-80 %RH with a sensitivity of 0.57 nm/%RH and in the range 80-95 %RH it is 1.43 nm/%RH. Furthermore assuming the OSA has a wavelength resolution of 0.01 nm, the proposed sensor has a humidity measurement resolution of 0.017% RH in the RH range from 40% RH to 80% RH, and 0.007% RH in the RH range from 80% to 95% RH. Considering the error in the measurements observed for the sensor and the RH sensitivity, the accuracy of the sensor in the RH range 40-80% is estimated to be ±2% RH, and in the range 80-95%, the accuracy is about ±1% RH.

In order to study the long term stability of the Agarose coated PCFI sensor, experiments are repeated 20 days after since the initial experiments. A similar experimental condition is maintained for both sets of measurements. For comparison the averaged

relative humidity responses obtained for the sensor during the two sets of measurements are plotted in Fig. 5.15. The relative humidity responses obtained are similar, confirming good long term stability for the sensor.

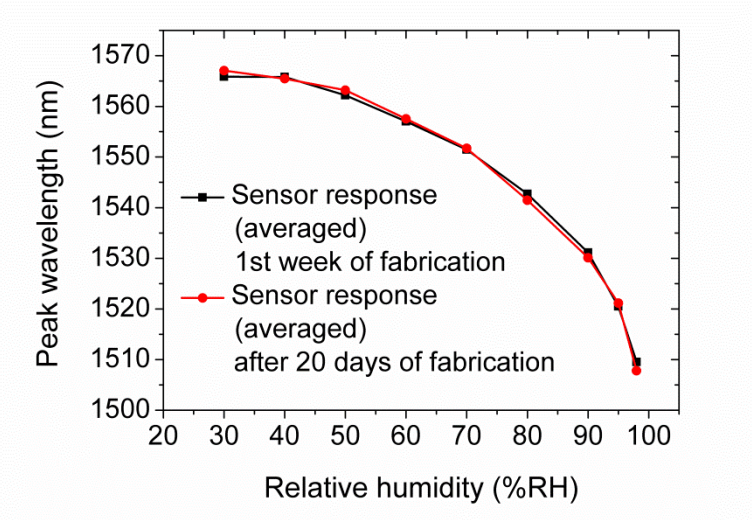

Fig. 5.15. Relative humidity response of the sensor: measurements are taken with an interval of 20 days and show the long term stability of the sensor.

The temperature dependence of the Agarose coated PCFI sensor was studied by setting the ambient relative humidity value at 50 % RH and is shown in Fig. 5.16. A spectral shift of 2.7±1 nm is observed for a temperature variation of 10 ^{O}C. The estimated error in the measurement data ±1 nm is due to the difficulty in maintaining a constant RH inside the environmental chamber when the temperature is varying. Since PCFI is almost temperature independent, the small temperature dependant shift of 0.27 nm/^{O}C obtained for the sensor is attributed to the contribution of the temperature dependence of Agarose. An increase in temperature decreases the RI of the Agarose, which in turn results in the blue shift of the interference spectrum of the sensor. Note that a temperature change of 1 ^{O}C gives a relative humidity measurement error of only about <0.5 %RH and taking into account the accuracy of the sensor, temperature

compensation may not be needed for this type of sensor if it is used in environments having no significant variations in temperature.

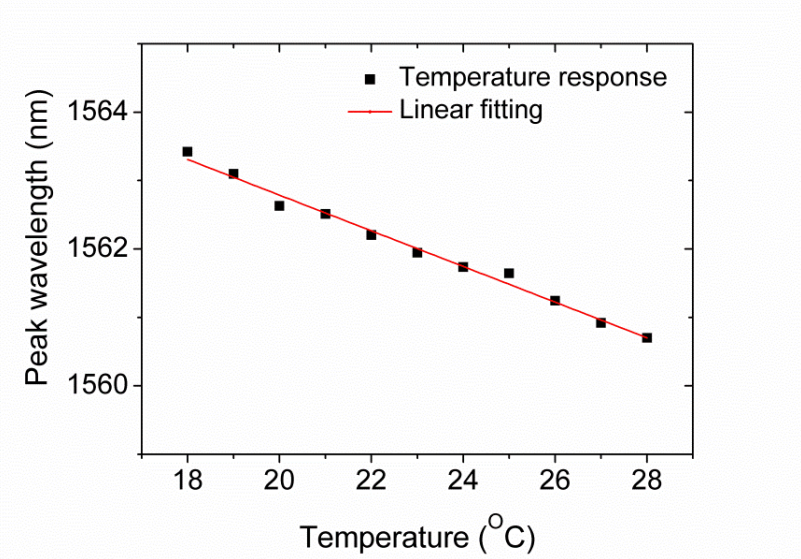

Fig. 5.16. Temperature dependence of the sensor

The response time of the sensor is studied by applying a step change in humidity to the sensor by directing a human breath exhale toward the sensor. The resultant time dependant response is found to be faster than the time response of the OSA. Therefore an optical power meter (PX Instrument Technology, PX2000-306) and a suitable wavelength output of a tunable laser source (Anritsu, Tunics plus CL/WB) are used to measure the change in the transmission of the device in response to a sudden RH change. The time dependant response of Agarose coated-PCFI device is shown in Fig. 5.17. The ambient humidity during the study was ~50 %RH and the temperature ~22 ^{O}C. The estimated response time (10% base line to 90% signal maximum) of the sensor is about 86 ms, when the RH jumps from 50 to >90%. The recovery time of a humidity sensor depends on how fast the water vapor is removed from the sensor which is proportional to the air flow surrounding the sensor. The estimated recovery time (90% signal maximum to 10 % baseline) of the sensor is 230 ms, which decreases if a flow of

dry air surrounds the sensor. It is expected that the response time of the sensor will decrease with a decrease in the thickness of the coating. But it is experimentally very difficult to apply a fast step change of humidity that can reveal these differences in the response time; therefore such a study is not included in the Thesis.

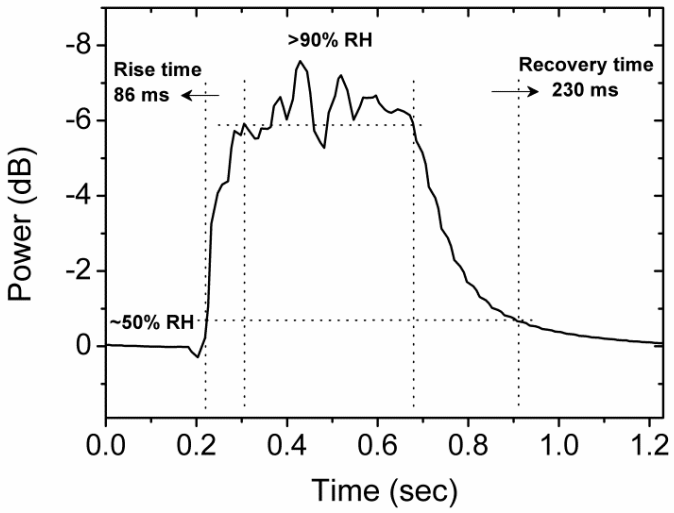

Fig. 5.17. Response time of the sensor

As the RH value is extracted from wavelength measurements, the sensor presented in this chapter is free from any errors due to power fluctuations in the optical source. The work presented in this chapter also provides the basis for the selection of an optimal operating point in terms of sensitivity and range of operation in the case of a PCFI coated with other materials for different sensing applications.

5.6. Summary

In this chapter the structure, fabrication and the working principle of a transmission type PCFI are discussed for sensing of RH. The relation between the fringe spacing and the length of the PCF section of the PCFI is verified experimentally. A PCFI is coated with Agarose layers of different thickness and it is demonstrated that the RI of the coating experienced by the mode interacting with the coating depends on the thickness of the

coating. It is also demonstrated that both bulk RI change and the thickness change of the Agarose coating with respect to changes in ambient RH affect the spectrum of the PCFI. The effect of coating thickness on the RH response of the AC-PCFI device is studied and it is shown that the RH sensitivity of an AC-PCFI depends strongly on the thickness of the coating.

Based on the study of the effect of coating thickness on the RH response of the AC-PCFIs a highly sensitive RH sensor based on an AC-PCFI is also demonstrated experimentally. The selection of an interferometer with large fringe spacing allowed achieving the effective index of the coating in a higher RI sensitivity region of the PCFI device and resulted in an improved sensitivity for the sensor. Refractive index characterisation of the device is performed experimentally to provide an approximate guide to the selection of a suitable coating thickness. The repeatability of the coating layer formation and the evolution of the coating layers on passing the device though Agarose solution multiple times are discussed.

The high sensitivity RH sensor presented in this chapter gives a large wavelength shift of 56 nm for an RH change of 58%. The sensor shows a linear response for an RH change in the range of 40-80 %RH with sensitivity of 0.57 nm/%RH and in the range 80-95 %RH it is 1.43 nm/%RH. The measurement accuracy of the sensor in the RH range 40-80% is ±2% RH, and in the range 80-95%, the accuracy is circa ±1% RH. The response time of the sensor is 86 ms for an RH change from 50% to 90% and the temperature dependence of the sensor is found to be 0.27 nm/^{O}C which is quite small compared to the RH sensitivity of the sensor. The work demonstrated in this chapter is useful for the development of various kinds of sensors for environmental, physical, biological or chemical parameters based on a PCF interferometer, where a coating acts as the transducer for an external parameter.

5.7 References

1. H. Y. Choi, M. J. Kim, and B. H. Lee, All-fiber Mach-Zehnder type interferometers formed in photonic crystal fiber, *Opt. Express*., 15, pp.5711-5720, (2007).
2. R. Jha, J. Villatoro, and G. Badenes, Ultrastable in reflection photonic crystal fiber modal interferometer for accurate refractive index sensing, *Appl. Phys. Lett*., 93, 191106, (2008).
3. J. Villatoro, V. Finazzi, V. P. Minkovich, V. Pruneri, and G. Badenes, Temperature-insensitive photonic crystal fiber interferometer for absolute strain sensing, *Appl. Phys. Lett*., 91, 091109, (2007).
4. D. Barrera, J. Villatoro, V. P. Finazzi, G. A. Cardenas-Sevilla, V. P. Minkovich, S. Sales, and V. Pruneri, Low-Loss Photonic Crystal Fiber Interferometers for Sensor Networks, *J. Lightwave Technol*., 28, pp.3542-3547, (2010).
5. R. Jha, J. Villatoro, G. Badenes, and V. Pruneri, Refractometry based on a photonic crystal fiber interferometer, *Opt. Lett*., 34, pp.617-619, (2009).
6. M. Smietana, D. Brabant, W. J. Bock, P. Mikulic, T. Eftimov, Refractive-index sensing with inline core-cladding intermodal interferometer based on Silicon Nitride nano-coated photonic crystal fiber, *J. Lightwave Technol*., 30, pp.1185-1189, (2012).
7. J. Mathew, Y. Semenova, G. Rajan, and G. Farrell, Humidity sensor based on photonic crystal fiber interferometer, *Electron. Lett*., 46, pp. 1341-1343, (2010).
8. J. Mathew, Y. Semenova, and G. Farrell, Photonic crystal fiber interferometer for dew detection, *J. Lightwave Technol*., 30, pp.1150-1155, (2012).

9. J. Mathew, Y. Semenova, and G. Farrell, Relative humidity sensor based on an Agarose infiltrated photonic crystal fiber interferometer, *IEEE J. Sel. Topics Quantum Electron.*, 18, pp.1553-1559, (2012).
10. W. J. Bock, T. A. Eftimov, P. Mikulic, and J. Chen, An inline core-cladding intermodal interferometer using a photonic crystal fiber, *J. Lightw. Technol.*, 27, (17), pp. 3933-3939, (2009).
11. J. Mathew, Y. Semenova, G. Farrell, A fiber bend based humidity sensor with a wide linear range and fast measurement speed, *Sens. Actuators A*, 174, pp.47-51, (2012).
12. J. Mathew, K. J. Thomas, V. P. N. Nampoori, P. Radhakrishnan, A comparative study of fiber optic humidity sensors based on chitosan and agarose, *Sens. Transducers J.*, 84, pp.1633-1640, (2007).
13. J. Mathew, Y. Semenova, G. Farrell, Polymer coated photonics crystal fiber interferometer for relative humidity sensing, A. Ghosh and D. Choudhury (Eds.): *Proc. IConTOP–II*, pp. 73-78, (2011).
14. F. J. Arregui, Z. Ciaurriz, M. Oneca, I. R. Matías, An experimental study about hydrogels for the fabrication of optical fiber humidity sensors, *Sens. Actuators B*, 96, pp.165-172, (2003).
15. K. J. Lee, D. Wawro, P. S. Priambodo, R. Magnusson, Agarose-gel based guided-mode resonance humidity sensor, *IEEE Sens J*, 7, pp.409-414, (2007).
16. C. Bariaˇıin, I. R. Matías, F. J. Arregui, and M. López-Amo, Optical fiber humidity sensor based on a tapered fiber coated with agarose gel, *Sens. Actuators B*, 69, pp.127-131, (2000).
17. M. Hernaez, C. R. Zamarreño, C. Fernandez-Valdivielso, I. del Villar, F. J. Arregui, and I. R. Matias, Agarose optical fiber humidity sensor based on

electromagnetic resonance in the infra-red region, *Phys. Status Solidi C*, 7, pp.2767-2769, (2010).

18. T. Watanabe, N. Ooba, Y. Hida, and M. Hikita, Influence of humidity on refractive index of polymers for optical waveguide and its temperature dependence, *Applied Physics Letters*, 72 (13), pp.1533-1535, (1998).
19. I. del Villar, I. R. Matias, F. J. Arregui, P. Lalanne, Optimization of sensitivity in Long Period Fiber Gratings with overlay deposition, *Opt Express*., 13(1), pp.56-69, (2005).
20. J. Lu, Z. Chen, F. Pang, T. Wang, Theoretical analysis of fiber-optic evanescent wave sensors, in *Proceedings of IEEE Microwave Conference*, (China-Japan Joint, 2008), pp.583-587, (2008).
21. S. T. Lee, P. S. Kumar, K. P. Unnikrishnan, V. P. N. Nampoori, C. P.G. Vallabhan, S. Sugunan, and P. Radhakrishnan, Evanescent wave fiber optic sensors for trace analysis of Fe3+ in water, *Meas. Sci. Technol*., 14, pp.858-861, (2003).

CHAPTER 6. PERFORMANCE COMPARISON OF RH SENSORS FOR DEW SENSING AND BREATHING MONITORING

6.1. Introduction

In this chapter a performance comparison of the relative humidity (RH) sensing devices demonstrated in the previous chapters is carried out. Comparison parameters are RH range, sensitivity, response time, presence or absence of hygroscopic materials, the type of probe (inline or end type), sensor size and temperature dependence. The advantages and limitations of the various sensors are also discussed.

Using this performance comparison as a starting point, the requirements for sensor for dew sensing are also discussed in this chapter and subsequently the use of a PCFI as a dew sensor is demonstrated. A dew point hygrometer using PCFI is also proposed.

Again using the performance comparison as a starting point, the requirements for sensors for breath rate sensing are also discussed in this chapter and subsequently a miniature optical breathing sensor based on an Agarose infiltrated photonic crystal fiber interferometer is presented. The sensor detects the variation in relative humidity that occurs between inhaled and exhaled breath. The sensor interrogation system can determine the breathing pattern in real time and can also predict the breathing rate and the breathing status during respiration.

6.2. Performance comparison of the RH sensors

Based on the parameters such as RH range, RH sensitivity, response time, sensor size, temperature dependence, advantages and limitations of the sensor, the performance,

comparison of the four RH sensing devices is presented in tables 6.1 to 6.3. Table 6.1 gives a comparison of different sensors in terms of their measurement range and sensitivity.

Table 6.1. Comparison of different sensors with respect to their measurement range and sensitivity.

RH Sensor		Measurement range	Sensitivity
Sensor based on a fiber bend	Polyethylene oxide coated fiber bend	80-90%	2 dB/%RH
	Agarose coated fiber bend	25-90%	0.1 dB/%RH
Sensor based on a photonic crystal fiber interferometer		27-96%	27-60 %RH→3.7 pm/%RH 60-80 %RH→8.5 pm/%RH 80-96 %RH→64 pm/%RH
Sensor based on an Agarose infiltrated photonic crystal fiber interferometer		14-98%	14-86 %RH→0.06 dB/%RH 86-98 %RH→0.6 dB/%RH
Sensor based on an Agarose coated photonic crystal fiber interferometer		30-95%	40-80 %RH→0.57 nm/%RH 80-95 %RH→1.43 nm/%RH

From the Table 6.1 it can be concluded that in terms of wavelength sensitivity, a sensor based on an Agarose coated photonic crystal fiber interferometer offers the highest sensitivity. In terms of power sensitivity a sensor based on Polyethylene oxide coated fiber bend is characterised by the highest sensitivity but only over a narrow RH range.

Table 6.2 gives a comparison of different sensors in terms of their size, response time and temperature dependence.

Table 6.2. Comparison of different sensors with respect to their size, response time and temperature dependence.

RH Sensor		Response time	Temperature dependence	Size of sensor head
Sensor based on a fiber bend	Polyethylene oxide coated fiber bend	780 ms when RH increases rapidly from 70% to 90%	Not studied	Bend radius 15 mm
	Agarose coated fiber bend	50 ms when RH increases rapidly from 60% to >90%	Power variation of ±0.5 dB is observed for a temperature change of 14 ^{O}C	Bend radius 16.75 mm
Sensor based on a photonic crystal fiber interferometer		Not studied	9.5 pm/^{O}C	40.5 mm
Sensor based on an Agarose infiltrated photonic crystal fiber interferometer		400 ms, when RH increases rapidly from 60 to >90%	0.066 dB/^{O}C	1 mm
Sensor based on an Agarose coated photonic crystal fiber interferometer		86 ms, when RH increases rapidly from 50 to >90%	0.27 nm/^{O}C	10 mm

From Table 6.2 it can be concluded that the response times of all the sensors are less than a second and the temperature dependence is low. Among all these sensors the

sensor based on an Agarose infiltrated photonic crystal fiber interferometer has the smallest size. Table 6.3 lists the key advantages and the limitations of the sensors.

Table 6.3. Key advantages and the limitations of the sensors

RH Sensor		Key advantages of the sensor	Limitations of the sensor
Sensor based on a fiber bend	Polyethylene oxide coated fiber bend	✚ Simple fabrication, low cost and disposable ✚ High sensitivity for a short RH range of 80-90% ✚ Fast response time	✚ Requires calibration for each sensor because of the poor fabrication repeatability ✚ Sensor size is limited by the diameter of the fiber bend ✚ Poor mechanical stability of the fiber bend structure ✚ Not suitable for high RH operations
	Agarose coated fiber bend	✚ Wide linear response ✚ Fast response time ✚ Simple fabrication, low cost and disposable ✚ Suitable for high RH operation	✚ Requires calibration for each sensor because of the poor fabrication repeatability ✚ Sensor size is limited by the diameter of the fiber bend ✚ Poor mechanical stability of the fiber bend structure
Sensor based on a photonic crystal fiber interferometer		✚ No hygroscopic materials required ✚ Temperature independent ✚ Suitable for high temperature and high pressure operations ✚ Suitable for dew sensing ✚ End type sensor because it requires only one interconnection	✚ For the long term use of the sensor a recalibration or cleaning of the sensor head required to overcome the contamination effects.

	fiber. - Simple fabrication, low cost and disposable	
Sensor based on an Agarose infiltrated photonic crystal fiber interferometer	- Miniature size - Improved sensitivity - Fast response time - Mechanical stability is best - Simple fabrication and disposable - End type sensor because it requires only one interconnection fiber. - Best sensor for breathing monitoring	- Because of the limitations in the fabrication accuracy only an approximate fabrication repeatability is possible
Sensor based on an Agarose coated photonic crystal fiber interferometer	- Suitable configuration for the study of effect of coating thickness on the sensitivity of a RH sensor - Possible to tune the RH sensitivity by changing the thickness of the coating - Fast response time - Simple fabrication and disposable	- Not an end type sensor because it requires an input and output fiber connected to the sensor. - Sensor interrogation is costlier

It is found that if hygroscopic materials are involved in the sensor design then the condensed moisture degrades the material behaviour and the recovery time required to go back to a low RH is usually high. This makes the RH sensors utilising hygroscopic materials not suitable for dew sensing. Another required parameter for a dew sensor is that the sensor response should be temperature independent. Therefore based on the performance comparison given above in Tables 6.1 to 6.3, the sensor based on a

photonic crystal fiber interferometer is suitable for dew sensing. The absence of hygroscopic materials, temperature independence, high and low temperature operation capability reinforce its suitability for dew sensing.

A breath monitor based on an RH sensor detects the variation in relative humidity that occurs between inhaled and exhaled breath. One basic requirement for the sensor is that both its response time and the recovery times should be less than breathing response times. If the size of the RH sensor is small then it can be easily fixed inside a respiration mask. The breathing rate sensor should be highly stable against air currents and the associated air turbulance during respiration, which can be achieved with a small size of the sensor because small size provides a higher mechanical stability against these factors. Also an end type sensor is prefered because then it will require only one connecting fiber connected to the respirator mask. Based on these considerations the RH sensor based on an Agarose infiltrated photonic crystal fiber interferometer is most suitable for breathing rate monitoring.

6.3. Dew sensor based on a PCFI

6.3.1. Introduction

Dew (condensed moisture) is a problem in the fields of precision electrical devices, automobiles, air conditioning systems, warehouses, domestic equipment, etc. High humidity and condensation can create an environment where the development of mould on the wooden parts can take place and it can also cause corrosion of iron parts. This is a major problem in the case of the works of art in the museums and churches [1]. Therefore there is a strong demand for a sensor capable of accurate detection of a high humidity or dew condensation state.

Approaches to dew detection using optical fiber have been previously reported in [2,3]. The working principle of these sensors is based on the change in the reflectivity which is observed on the surface of the fiber tip, when a water layer is formed on its distal end. The dependence on reflected power measurement scheme used in [2,3] increases the chance of measurement error due to source power fluctuations. A simple sensor head for humidity sensing based on a photonic crystal fiber interferometer operated in reflection mode is demonstrated in chapter 3. The fabrication of such a sensor is very simple since it only involves cleaving and fusion splicing. Furthermore, the spectral measurement technique utilized in this work is free from errors due to source power variations. In the following section of this chapter a dew sensor based on such a PCFI is demonstrated. The sensor shows good dew point measurement accuracy. Since the sensor head is fabricated from a single material, silica, its temperature dependence is very low. From the results for the dew sensor performance with different lengths of photonic crystal fiber (PCF) it was shown that a device with a compact length of PCF is suitable for dew sensing albeit with a reduction in the speed of response. The dew response of the sensor at different ambient humidity values is also demonstrated in this section.

6.3.2. Operating principle of the dew sensor

To study the response of the PCFI to dew formation it is required to set the temperature of the PCFI to dew point temperature, which is obtained from the values of ambient relative humidity and temperature. To do this let us consider a quantity of air with a constant water vapor concentration at a certain temperature, T, and relative humidity, RH < 100%. The dew point temperature, T_d, is defined as the temperature to which this quantity of air must be cooled down such that, at a constant pressure, condensation occurs (RH = 100%). In terms of relative humidity RH and ambient temperature T, the dew point temperature is given by the Magnus formula [4]:

$$T_d(T, RH) = \alpha \frac{\ln\left(\frac{RH}{100\%}\right) + \frac{\beta T}{\alpha + T}}{\beta - \ln\left(\frac{RH}{100\%}\right) - \frac{\beta T}{\alpha + T}} \quad (6.1)$$

where, α=243.04 ^{O}C and β=17.62 are the so-called Magnus parameters for the temperature range -45 to 50 ^{O}C. Therefore decreasing the temperature of the PCFI increases the relative humidity in its vicinity. At certain temperature the relative humidity becomes 100% or reaches the dew point temperature and hence the water vapor starts to condense. The condensed water vapor on the PCFI surface causes a large change in the effective refractive index of the cladding mode which in turn causes a large phase change between the interfering modes and therefore a large wavelength shift of the interference peaks is expected.

6.3.3. Experimental characterization of the sensor

The dew response of the PCF interferometer was studied by placing it on a thermoelectric cooler (TEC) as shown in Fig. 6.1. In order to study the influence of dew on the PCFI, it was decided to limit the PCFI length used in this experiment to 42 mm or less, to suit the size of the available TEC used for temperature control. The temperature of the TEC element was controlled by a temperature controller. A thermistor was used to provide temperature feedback to the controller from the TEC element. An additional handheld thermometer was used to confirm the temperature on the TEC surface. The entire setup was placed inside a controlled environmental chamber. The relative humidity and the temperature inside the chamber can be controlled with an accuracy of ±2 %RH and ±1 ^{O}C respectively. For the purpose of this experiment the ambient temperature inside the chamber was fixed at 25 ^{O}C.

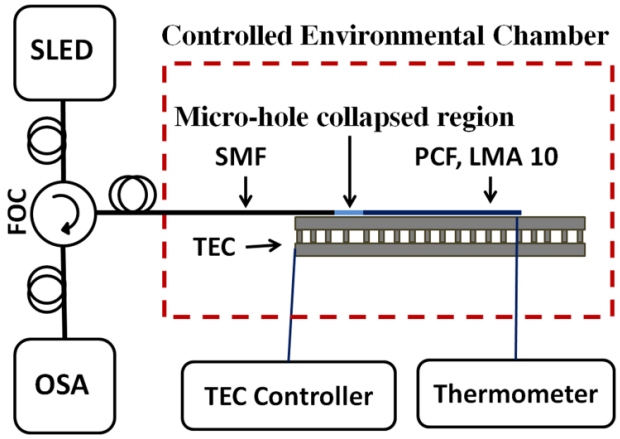

Fig.6.1. Experimental arrangement for the calibration of PCFI based dew sensor.

Temperature dependance of this type of PCFI was reported in chapter 3 and it was shown to be very small < 10 pm/^{O}C, in other words the PCFI is almost temperature independant. The dew sensing experiments were carried out at normal atmospheric pressure. To study the dew response of the device the temperature of the PCFI was decreased from an ambient temperature (25 ^{O}C) to the dew point temperature at a fixed ambient relative humidity. It was found that the position of the interference peaks shifted to longer wavelengths with a decrease in temperature. This shift is similar to the humidity response of the PCFI as shown in Fig. 3.6 and 3.7 of chapter 3. This occurs because the relative humidity inside the microholes and in the vicinity of the PCFI increases with a decrease in temperature and causes a shift. At or just below the dew point temperature (100% RH) water vapor condensation occurs, the condensed water vapor on the outer surface of the PCF also contributes to the change in the effective refractive index (RI) of the cladding mode, which results in a large spectral shift.

The spectra of two interferometers at room temperature and at the dew point temperature for devices fabricated with lengths 40.5 mm and 3.5 mm are shown in Fig. 6.2 & 6.3. The lengths selected are practically the largest and the smallest PCF lengths that could be studied using the experimental setup. The ambient humidity during this

study was set at 60 % RH. From the Fig. 6.2 & 6.3 it is clear that relatively to the period of the interferometer the shift will be larger for a longer PCFI due to a longer interaction length available for the interference between the cladding mode and the adsorbed water vapor. Hence the sensitivity to water vapor content and thus dew point temperature is higher for a device with a longer length of PCF.

It is important to note that due to the large fringe spacing it is difficult to measure the peak shift accurately for a short PCFI, therefore the comparison of sensitivities for PCFIs with different lengths is not straightforward. It should also be noted that even a PCFI with a small length (3.5 mm, fringe spacing ~90 nm) when exposed to dew point temperature for a relatively long time, i.e. several minutes, will result in a measurable fringe shift as shown in Fig. 6.3. This is because an increasingly thicker adsorbed water layer is formed on the silica surfaces of the PCF as time progresses. Thus compared to 3.5 mm device the ~40.5 mm device is preferable for achieving a fast response time (in the order of seconds), but when a compact length is the main requirement a shorter PCFI also can be used as a dew sensor with a reduced measurement speed.

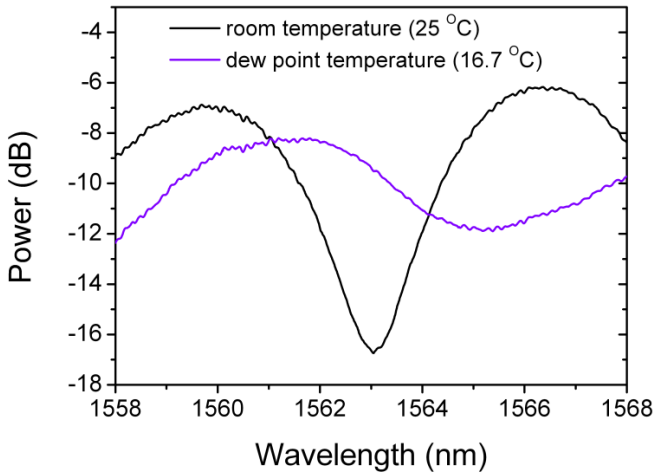

Fig. 6.2. Interference spectra for a device with a length of 40.5 mm at room temperature and at dew point temperature.

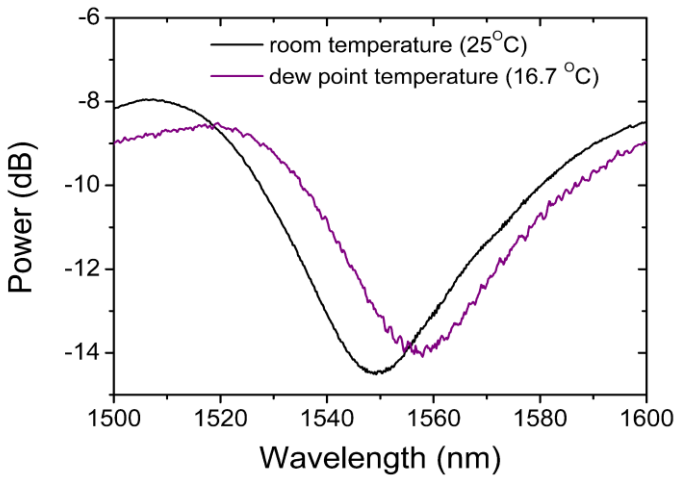

Fig. 6.3. Interference spectra for a device with a length of 3.5 mm at room temperature and at dew point temperature.

The dew sensing performance of a PCFI at different environmental conditions was determined by studying the dew response of the PCFI with L= 40.5 mm at three ambient humidity values of 40, 60 and 80 %RH. At each humidity value the temperature of the PCFI is reduced from 26 ^{O}C to the corresponding dew point temperature. The peak wavelength shift of the device is plotted against temperature in Fig. 6.4. The three curves represent the peak shift corresponding to the ambient relative humidity values of 40, 60 and 80 %RH. The onset of the dew formation is characterized by a large shift of the interference peak which is clear in Fig. 6.4. The dew point temperature calculated by using equation (6.1) based on the corresponding ambient conditions is marked on each curve in Fig. 6.4. For all these three ambient humidity values the continuous spectral shift starts exactly at the dew point temperature which confirms the high dew point measurement accuracy (estimated as ±0.1 ^{O}C) of the sensor.

By bringing the temperature of the PCFI back to room temperature the interference peaks also shift back to their initial position. This shows the reversibility of the sensor.

Because of the small size of the sensor head and the high sensitivity to adsorbed water vapor the demonstrated sensor response time is in seconds which is relatively fast compared to existing dew point hygrometers that take several minutes for a single measurement. The simple fabrication method, small size and the all-silica nature of the demonstrated sensor head suggest that with some simple additions such as attaching a TEC element with temperature feedback on to the PCFI, the combination can be used as a dew point hygrometer.

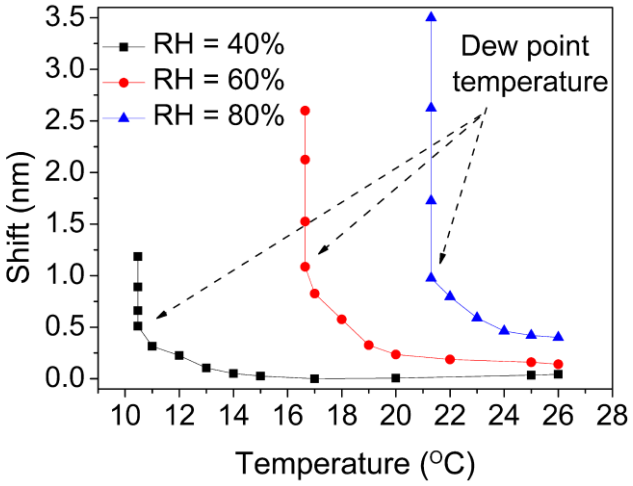

Fig. 6.4. Interference peak shift of the PCFI with respect to temperature at three ambient humidity values of 40, 60 and 80 %RH.

6.4. A miniature breathing sensor based on PCFI

6.4.1. Introduction

Breathing is a vital human sign; it is the process that moves varying volumes of air into and out of the lungs. This is required to provide an adequate oxygen (O_2) supply to meet the energy production requirements of the body and maintain a suitable acid-base status by removing carbon dioxide (CO_2) from the body. The act of normal breathing has a

relatively constant rate. The rate is noted by observing the frequency of breathing. The number of breaths per minute is called the breath rate.

Breathing monitoring is one of the most important elements of assessing physiological state. It can provide valuable information related to cardiac, neurological and pulmonary conditions [5]. Breath rate monitoring is important during certain imaging and surgical procedures where the patient needs to be sedated or anesthetized [6,7] because respiratory failure is difficult to predict and in just a few minutes life-threatening conditions can arise due to its failure. On the other hand, some illnesses such as apnea, tachypnea, hyperpnea, hypopnea and Cheyne-Stokes respiration syndromes can be diagnosed by detecting alterations in breathing patterns such as delayed breathing, voluntary breath holding, shortness of breath, hyperventilation, or abnormal respiratory rate etc. [8,9]. Continuous monitoring of respiratory activity is also of great importance in the case of infants susceptible to sudden infant death syndrome.

Breathing can be monitored utilizing nose exhaled air (using a humidity sensor, temperature sensor, capnometer or spirometer) or by monitoring the movement across the thoracic cavity/chest from the rise and fall of the abdomen, or with a plethysmograph. The most popular commercially available sensors are electronic sensors [10]. Electronic breathing sensors are not suitable when patients are for example in a magnetic resonance imaging (MRI) system, or during any oncological treatment that requires the administration of radiation or high electric/magnetic fields. MRI is a powerful, non-invasive way of obtaining detailed internal images of the human body which probes the inside of the body with strong magnetic fields. Sensors including metallic parts or electrical conductive wire are inappropriate during MRI, since they disturb the imaging process and also can cause burns on the patient's skin [11-13]. Respiratory rate and apnea may be monitored during MRI procedures using an end-tidal

carbon dioxide monitor or a capnometer. These devices measure the level of carbon dioxide during the end of the respiratory cycle (i.e., end-tidal carbon dioxide). The interface between the patient for the end-tidal carbon dioxide monitor and capnometer is a nasal or oro-nasal cannula that is made from plastic. This interface prevents potential adverse interactions between the monitor and the patient during an MRI procedure but some delay in measurement exists because the air has to reach the sensor from the subjects nose through the cannula [7,11]. In addition, the patients cannot be monitored during the transport in or out of the MRI room since such MRI compatible monitoring systems are not easily transportable and often exclusively used for MRI examination due to their high cost.

Fiber optic sensors are advantageous for such applications because of their electromagnetic immunity and because they can be interrogated remotely as demonstrated in many application areas. Breath monitoring using optical fiber sensors can be undertaken by detecting the contraction and expansion of the patient's chest and abdomen that occur during breathing [14-19]. This can be done by means of highly-sensitive strain, bending or pressure sensors set in a strap, belt or patch attached to the patient's body [14-19]. However this technique is only capable of recording body movements associated with respiratory effort. Therefore, such optical fiber based respiratory rate monitoring techniques do not detect apneic episodes related to upper airway obstruction (i.e., absent airflow despite respiratory effort) and may not provide sufficient sensitivity for assessing patients during MRI procedures. The cross sensitivity to extraneous body movements will also affect the performance of these kind of sensors making them less suitable for accurate breath monitoring. Breathing can also be monitored using a fiber optic air flow sensor placed close to the patient's nose or mouth

[20] but it will show high cross sensitivity to vibrations associated with body movements.

Another approach to breath rate monitoring is using fiber-based humidity or temperature sensors placed close to the patient's nose or mouth since the air exhaled has higher humidity and is warmer than the inhaled air [8, 21-25]. Air in the lungs is essentially saturated with water at body temperature of 37 ^{O}C [26]. Most of that water is supplied by evaporation from the membranes lining the nose and as a result, these surfaces are cooled a bit. When one exhales, the breath passes over these cooled surfaces and loses some of its moisture, thus conserving at least some of the body water. However, the air exhaled is still saturated (100% relative humidity) or very close to it.

A miniature optical humidity sensor based on an Agarose infiltrated photonic crystal fiber interferometer (AI-PCFI) has been demonstrated in chapter 4. Compared to the existing optical-fiber-based humidity sensors, the sensor proposed in chapter 4 has the advantages of a very compact size, good sensitivity, fast response time and ease of fabrication. The sensor head is also low cost and thus could be disposable. Disposable sensors are required while monitoring breathing from the nose or mouth because exhaled breath condensate can contaminate the sensor head making the sensor unsuitable to reuse on another patient. The end-type sensor head configuration offers the advantages of being able to operate in environments which demand a compact probe-type sensor and also reduced system complexity as only one interconnecting fiber is needed. These advantages underpin the motivation to investigate disposable sensors for breathing monitoring in a clinical situation using AI-PCFI. In this section of the chapter a breathing pattern and breathing rate sensor developed using an AI-PCFI is demonstrated. The sensor registers a change in the received optical power as a function of time as the air is exhaled making it suitable for monitoring breathing patterns. It has

been demonstrated that by appropriate signal processing one can determine the breathing rate and the breathing status during expiration. The demonstrated sensor is also suitable for monitoring a decrease in respiratory rate, hypoxemia, or airway obstruction associated with the use of sedatives and anesthetics in the MRI environment.

6.4.2. Experimental demonstration and discussion

The complete experimental sensor system is composed of a light source - tunable laser (Anritsu, Tunics plus CL/WB), a fiber optic coupler/circulator (FOC), the AI-PCFI (relative humidity sensor), an optical detector (PX Instrument Technology, PX2000-306) and a PC with a breath analysis application program, as shown in Fig. 6.5.

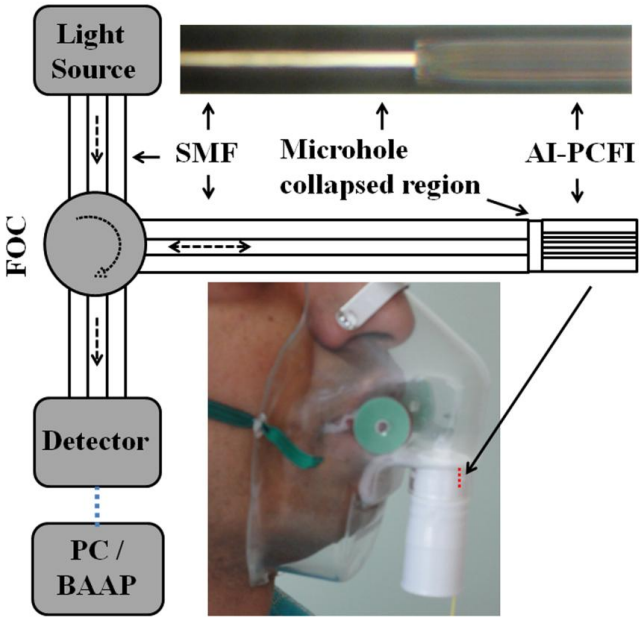

Fig. 6.5. Schematic diagram of a fiber optic breath sensor system, (upper) microscope image of an AI-PCFI and (lower) a photograph of the mask placed on the volunteer's face showing the position of the sensor inside the mask (dotted line). (FOC- Fiber optic circulator, SMF-Single mode fiber, AI-PCFI-Agarose infiltrated-photonic crystal fiber interferometer, PC/BAAP-Personal computer/Breath analysis application program; dotted arrows represent the light path).

The detailed fabrication procedure for the AI-PCFI is explained in chapter 4. The size of the AI-PCFI used for breathing monitoring is 1 mm in length and 125 μm in diameter; the length includes both the 250 μm hole collapsed region and approximately 100 μm long Agarose-infiltrated region. Such a small sensor length gives a large fringe spacing (calculated fringe spacing for a 1 mm length photonic crystal fiber interferometer in chapter 4 is 330 nm). An advantage of choosing a compact length is that the spectrum remains very stable when the sensor is subjected to vibrations, most particularly from airflow in this case. The effective RI of the cladding mode of the device depends on the RI of the Agarose material infiltrated into the microholes of the PCF. The RI of the Agarose changes with the ambient RH, which in turn changes the modal propagation constant of the cladding mode. As a result, a phase change is induced between the interfering core and cladding modes, which in turn causes the shift of the interference pattern. A detailed calibrated RH response of the AI-PCFI is given in chapter 4. So by monitoring the humidity-induced changes in the interference fringes in the reflection spectrum of the device due to breath exhalation, the breathing rate and pattern can be measured.

In the experiment the optical power change obtained due to the spectral shift induced by changes in humidity during the breathing cycle is monitored. For this purpose a tunable laser output at a wavelength of 1550 nm is fed to the AI-PCFI via the FOC and the reflected optical power from the AI-PCFI is measured using a detector. Accurate measurement of pulmonary ventilation or breathing often requires the use of devices such as masks or mouthpieces coupled to the airway opening. For this purpose the device was mounted in an inexpensive, disposable plastic oxygen mask which in turn was attached to a volunteer's nose and mouth and secured with the elasticized headband of the mask (See Fig. 6.5). The sensor was set in such a way that it was kept

approximately 5 cm from the patient's nose to avoid condensation on the device. The distance between the tip of the nose and the tip of the sensor is estimated using a conventional measuring scale. In the present study this distance could vary depending on the patient's nose size because the sensor is fixed on the oxygen mask (Fig. 6.5). However in practice this distance can be maintained by fixing the sensor on to a moving platform inside the oxygen mask or by suitably fixing the sensor inside the mask with a prior knowledge of the patient nose size. The normal baseline RH signal depends on the room humidity and also on the distance of the sensor from the patient's nose. The time-dependent RH signal when the patient is breathing normally is equal to the ambient RH (< 80% RH) during inhalation and ~100% RH during exhalation. The detailed packaging of the AI-PCFI is not investigated in this study. But it is important to point out that before using the sensor in a clinical environment the sensor would have to be packaged inside a suitable plastic tube to prevent the transmitted light reaching the volunteer's eyes, face or skin.

The optical power received by the detector is acquired in real time (with a maximum delay of the order of ms) using the breath analysis application program based on LabVIEW platform. Fig. 6.6 shows a screen shot of the user interface of the breath analysis application program, for the case of a regular breathing pattern. The real time breathing response of the sensor system is displayed by the application program user interface. During breath expiration due to an increase of the ambient humidity in the vicinity of the sensor, the reflected power received by the detector decreases [chapter 4]. In the real time breathing response trace there are valleys which represent exhalation and peaks which represent inhalation. The lower plot in Fig. 6.6 is the breathing state indicator calculated from the breathing pattern using a preset threshold. It has two states, a high level represents the state after air is exhaled and a low indicates the state

after air is inhaled. Each time when the power decreases below the preset threshold value, the breath count (BC) is incremented once and it is displayed in the user interface of the program. Since breath rate is the number of breaths per minute, after every 60 seconds the counter is reset. Average Breath Rate (BR) is calculated as BR = (BC*60)/ET where ET is the elapsed time since the last reset. For user convenience the elapsed time, breath rate and breath status are also displayed in the user interface/front panel of the application. Breathing status is described as follows 'NORMAL' when BR is between 10-20; 'LOW' when BR<10; 'HIGH' when BR>20.

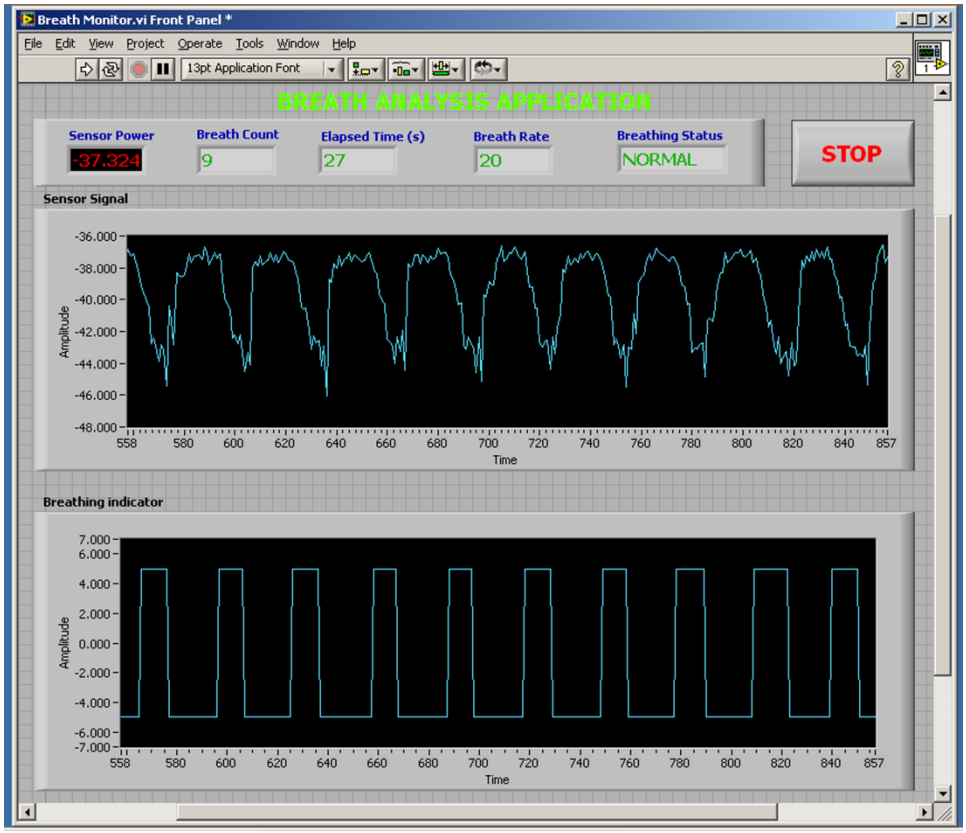

Fig. 6.6. Screen shot of the user interface of the breath analysis application program showing the continuous breathing response. Upper plot shows the breathing pattern (inhalation → peaks and exhalation → valleys) and the lower plot indicates the derived breathing state (inhalation → low and exhalation → high). Units of the axis are: upper plot x-axis is seconds multiplied by 10 and y-axis is dB; lower plot x-axis is seconds multiplied by 10 and y-axis is arbitrary units.

Fig. 6.7 shows a screen shot of the user interface for an irregular breathing pattern, where the subject ceases breathing for a few seconds, in order to demonstrate that the sensor system is capable of monitoring breathing abnormalities in real time. The valleys shown in the upper plots of Fig. 6.6 and 6.7 are due to the air breathed out by the volunteer and the area inside each of these valleys can be correlated with the amount of air breathed out. Thus by applying an appropriate signal analysis and calibration, the breathing air volume could be estimated from the sensor response. The value of breathing volume could be used as an indicator of potential respiratory dysfunction and subject's pulmonary health status.

Since the dimensions of the sensor head are very small, the breathing response is unaffected by the turbulence and vibrations that result from air flow during breathing and other mechanical effects that may occur due to the movement of a patient. Given that the interrogation system measures the reflected intensity of light, a possible source of error could arise from random variations in the received power resulting from variations in the bend radius at any bends in the fiber connecting the sensor to the interrogation system. To prevent such a failure the fiber cable connected to the sensor would need to be packaged to avoid small bend radii and significant changes in bending radius. Other fluctuation sources are the variations in the ambient RH, the distance between patient's nose and the sensor and the fluctuations in the RH of the exhaled air. The source power fluctuation, wavelength drift and the detector noise might also contribute to the measurement errors in the system demonstrated. However selecting a threshold power equivalent to a higher RH than the ambient RH should overcome the effect of these fluctuation sources on monitoring the breath rate. Finally, it should be pointed out that failure of the sensor may occur if a person coughs or contaminates the

device with fluids (saliva, sputum, etc.). However, these issues can be avoided or overcome by embedding the device in a nasal clip or by adequate packaging.

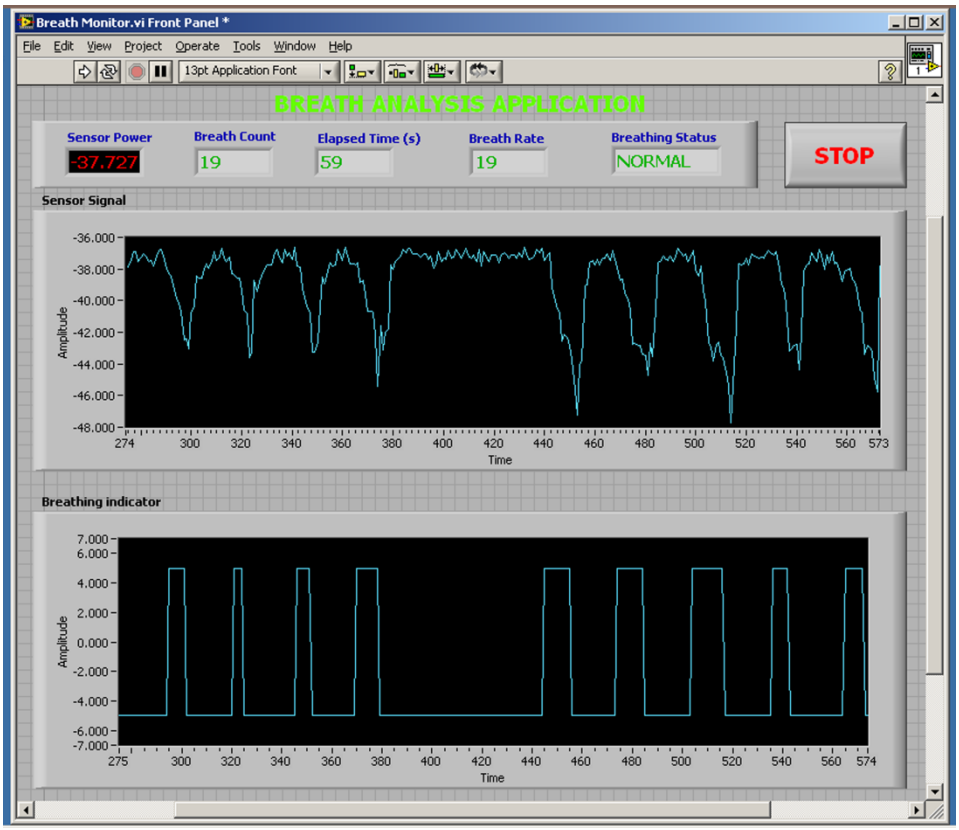

Fig. 6.7. Screen shot of the user interface of the breath analysis application program showing a breath-hold. Upper plot shows the breathing pattern (inhalation → peaks and exhalation → valleys) and the lower plot indicates the derived breathing state (inhalation → low and exhalation → high). Units of the axis are: upper plot x-axis is seconds multiplied by 10 and y-axis is dB; lower plot x-axis is seconds multiplied by 10 and y-axis is arbitrary units.

Finally while a tunable laser source was used in the demonstration described here, in order to reduce the cost of the system for real-world applications the tunable laser can be readily replaced with a low cost fixed wavelength laser diode. A high power change of >5 dB will be obtained using this sensor during breathing even in the event of the source intensity and/or center wavelength drift. In addition a shift in the dynamic signal

power level of the sensor can be addressed easily in the LabVIEW program by suitably shifting the threshold, so that the source power fluctuation and the wavelength drift of a low cost source will not degrade the accuracy of the breath rate monitoring.

6.5. Summary

The performance comparison of the RH sensing devices demonstrated in previous chapters is carried out in this chapter based on various parameters such as RH range, sensitivity, response time, sensor size, temperature dependence, key advantages and limitations of the sensor. It is concluded that in terms of wavelength resolution sensor based on an Agarose coated photonic crystal fiber interferometer offers the highest resolution. In terms of power resolution sensor based on Polyethylene oxide coated fiber bend offers the highest resolution but only in a narrow RH range. The response time of the presented sensors is less than a second and the temperature dependence is very low. Among all these sensors the sensor based on an Agarose infiltrated photonic crystal fiber interferometer has the smallest size.

The selection of suitable devices for dew sensing and breathing monitoring is demonstrated based on the performance comparison of these sensors. A reflection type PCFI not using a hygroscopic material is utilised for dew sensing and an Agarose infiltrated PCFI with miniature size and good sensitivity is used for breathing monitoring.

A dew sensor based on a reflection type PCFI is demonstrated in section 6.3. The basic sensing principle of the dew sensor and the dew response of the PCF interferometer are explained in detail. The demonstrated sensor shows good dew point measurement accuracy ($\pm 0.1\ ^{O}C$). From the results of the dew sensor performance with different lengths of photonic crystal fiber it was shown that a device with a compact length of

PCF is suitable for dew sensing albeit with a reduction in the speed of response. The dew response of the sensor at different ambient humidity values is also demonstrated in this section.

A miniature optical breathing sensor is demonstrated in section 6.4. The sensor is based on an Agarose infiltrated photonic crystal fiber interferometer which detects the variation in relative humidity that occurs between inhaled and exhaled breath. The sensor interrogation system determines the breathing pattern in real time and also predicts the breathing rate and the breathing status during respiration. The demonstrated sensor is also suitable for monitoring patients during a magnetic resonance imaging scan.

6.6. References

1. D. Camuffo, and S. Valcher, A dew point signaller for conservation of works of art, *Environmental Monitoring and Assessment*, 6(2), pp. 165-170, (1986).
2. F. Baldini, R. Falciai, A. A. Mencaglia, F. Senesi, D. Camuffo, A. D. Valle, and C. J. Bergsten, Miniaturised optical fiber sensor for Dew detection inside organ pipes, *Journal of Sensors*, 2008, Article ID 321065, (2008).
3. S. M. Kostritskii, A. A. Dikevich, Y. N. Korkishko and V. A. Fedorov, Dew point measurement technique utilizing fiber cut reflection, *Proceedings of SPIE*, Vol. 7356, pp. 73561K, (2009).
4. M. G. Lawrence, The Relationship between relative humidity and the dew point temperature in moist air: a simple conversion and applications, *Bulletin of the American meteorological society*, 86, pp.225-233, (2005).
5. S. R. Braun, *Clinical Methods, The History, Physical, and Laboratory Examinations* (Butterworth Publishers, Stoneham, MA, 1990), Chap. 43.

6. M. Folke, L. Cernerud, M. Ekström, and B. Hök, Critical review of non-invasive respiratory monitoring in medical care, *Med. Biol. Eng. Comput*., 41(4), pp.377-383, (2003).
7. L. Schulte-Uentrop, and M. S. Goepfert, Anaesthesia or sedation for MRI in children, *Curr. Opin. Anaesthesio*., 23(4), pp.513-517, (2010).
8. S. Akita, A. Seki, and K. Watanabe, A monitoring of breathing using a hetero-core optical fiber sensor, *Proc. SPIE* 7981, 79812W (2011).
9. P. Várady, T. Micsik, S. Benedek, and Z. Benyó, A novel method for the detection of apnea and hypopnea events in respiration signals, *IEEE T Bio-Med Eng*., 49(9), pp.936-942, (2002).
10. F. Q. AL-Khalidi, R. Saatchi, D. Burke, H. Elphick, and S. Tan, Respiration rate monitoring methods: a review, *Pediatr. Pulm*., 46(6), pp.523-529, (2011).
11. Shellock R & D Services, Inc. and Frank G. Shellock, Ph.D., "Monitoring patients in the MRI environment," (2012), http://www.mrisafety.com/safety_article.asp?subject=40.
12. C. T. Results, "Optical sensors make MRI scans safer," Science Daily 20 September 2008, www.sciencedaily.com/releases/2008/09/080918091609.htm.
13. M. F. Dempsey, and B. Condon, Thermal injuries associated with MRI, *Clin. Radiol.*, 56, pp.457-465, (2001).
14. A. Babchenko, B. Khanokh, Y. Shomer, and M. Nitzan, Fiber optic sensor for the measurement of respiratory chest circumference changes, *J. Biomed. Opt*., 4(2), pp.224-229, (1999).
15. G. Wehrle, P. Nohama, H. J. Kalinowski, P. I. Torres, and L. C. G. Valente, A fiber optic Bragg grating strain sensor for monitoring ventilatory movements, *Meas. Sci. Technol*., 12(7), pp.805-809, (2001).

16. A. Grillet, D. Kinet, J. Witt, M. Schukar, K. Krebber, F. Pirotte, and A. Depré, Optical fiber sensors embedded into medical textiles for healthcare monitoring, *IEEE Sens. J*., 8(7), pp.1215-1222, (2008).
17. M. Nishyama, M. Miyamoto, and K. Watanabe, Respiration and body movement analysis during sleep in bed using hetero-core fiber optic pressure sensors without constraint to human activity, *J. Biomed. Opt*., 16(1), 017002, (2011).
18. A. F. Silva, J. P. Carmo, P. M. Mendes, and J. H. Correia, Simultaneous cardiac and respiratory frequency measurement based on a single fiber Bragg grating sensor, *Meas. Sci. Technol*., 22(7), 075801, (2011).
19. J. Witt, F. Narbonneau, M. Schukar, K. Krebber, J. D. Jonckheere, M. Jeanne, D. Kinet, B. Paquet, A. Depré, L. T. D'Angelo, T. Thiel, and R. Logier, Medical textiles with embedded fiber optic sensors for monitoring of respiratory movement, *IEEE Sens. J*., 12(1), pp.246-254, (2012).
20. L. Mohanty, and K. S. C. Kuang, A breathing rate sensor with plastic optical fiber, *Appl. Phys. Lett*., 97, 073703, (2010).
21. S. Muto, H. Sato, and T. Hosaka, Optical humidity sensor using fluorescent plastic fiber and its application to breathing-condition monitor, *Jpn. J. Appl. Phys*., 33(10), pp.6060-6064, (1994).
22. F. J. Arregui, Y. Liu, I. R. Matias, and R. O. Claus, Optical fiber humidity sensor using a nano Fabry–Perot cavity formed by the ionic self-assembly method, *Sensor Actuat B-Chem*, 59(1), pp.54-59, (1999).
23. Y. Kang, H. Ruan, Y. Wang, F. J. Arregui, I. R. Matias, and R. O. Claus, Nanostructured optical fiber sensors for breathing airflow monitoring, *Meas. Sci. Technol*., 17(5), pp.1207-1212, (2006).

24. W. J. Yoo, K. W. Jang, J. K. Seo, J. Y. Heo, J. S. Moon, J. H. Jun, J. Y. Park, and B. Lee, Development of optical fiber-based respiration sensor for noninvasive respiratory monitoring, *Opt. Rev*., 18(1), pp.132-138, (2011).
25. F. C. Favero, J. Villatoro, and V. Pruneri, Microstructured optical fiber interferometric breathing sensor, *J. Biomed. Opt*., 17(3), 037006, (2012).
26. Natural science forum results, "Relative humidity of human exhaled breath," NatScience.com 03 Jul 2004, http://www.natscience.com/Uwe/Forum.aspx/bio/233/Relative-humidity-of-human-exhaled-breath.

CHAPTER 7. CONCLUSIONS AND FUTURE RESEARCH

This chapter presents achievements and conclusions from across the thesis. Future research as an extension of this PhD thesis is also discussed.

7.1 Conclusions from the research

The core aim of this research as stated in chapter 1 was to investigate several approaches to humidity sensing using optical fiber which both overcome the disadvantages of existing fiber optic sensors and also allow fiber humidity sensors to be applied in new application areas. The novel fiber structures investigated for humidity sensing are an optical fiber bend and different configurations of photonic crystal fiber interferometers (PCFI). Two types of relative humidity (RH) sensor based on a fiber bend have been developed: a polyethylene oxide coated fiber bend and an Agarose coated fiber bend. The developed RH sensors based on photonic crystal fiber interferometer are an open ended reflection type PCFI, an Agarose infiltrated PCFI and an Agarose coated transmission type PCFI. All these sensors showed good sensitivity and a reversible, repeatable and fast response to RH variations. A performance comparison of the developed RH sensors is carried out and applications of the RH sensors as a dew sensor and as a breathing monitor are demonstrated. These conclusions are divided into five sections based on the different research strands investigated and reported in this thesis.

I. Relative humidity sensor based on a fiber bend

In this thesis detailed studies of two disposable humidity sensors based on a fiber bend are reported. The first sensor is a fiber bend coated with Polyethylene oxide and the second sensor is a fiber bend coated with Agarose. A high bend loss fiber (1060XP) is utilised in this study. The spectral response of the fiber bend as a function of the

surrounding refractive index (RI) is characterised to enable the selection of a suitable polymer coating for humidity sensing and to establish the effect of wavelength on the sensitivity of the sensor. Based on the discussion of the suitability of various hygroscopic coatings, Agarose is chosen for the later RH sensor designs.

The conclusions from these studies are:

- The use of high bend loss fiber enhances the sensitivity of the RH sensors and also allows one to utilize relatively large bend radii to avoid stress induced breakage of the fiber.
- The RH sensor based on a polyethylene oxide coated fiber bend with an optimised wavelength and bend radius utilizing power measurement for interrogation showed a high sensitivity to RH in a narrow range (85-90%) of RH variation.
- The estimated response time of the polyethylene oxide coated fiber bend is 780 milliseconds for a 20% RH change from 70% to 90%.
- The sensor based on an Agarose coated fiber bend showed a linear change in its insertion loss for a wide humidity range: 25-90% RH.
- The estimated response time of the Agarose coated fiber bend based RH sensor is circa 50 ms for a 30% RH change.
- The humidity sensitivity of the Agarose coated fiber bend based RH sensor is wavelength dependent and high sensitivity is observed at higher wavelengths.
- The typical humidity responses of both the sensors are suitable for human breath rate monitoring.

- The limitations of the fiber bend based RH sensor are the sensor size which is limited to the diameter of the bend and poor mechanical stability.

II. Relative humidity sensor based on a photonic crystal fiber interferometer

A brief analysis of modal interferometers based on PCF is reported in this thesis along with a discussion of the operating principle and the fabrication techniques of a reflection type PCF based modal interferometer. A humidity sensor based on an open ended PCF interferometer is demonstrated. The temperature dependence of the sensor and the dependence of the RH sensitivity on the length of PCF are also experimentally investigated.

From the studies, it can be concluded that:

- The characteristics of a reflection type PCFI depend on the splicing conditions and the length of the PCF section.
- It has been demonstrated that an open ended reflection type PCF interferometer is suitable for RH sensing.
- The RH sensitivity of the sensor depends on the length of the PCF and a device with a longer length PCF section is more sensitive to relative humidity changes.
- The sensitivity of an open ended reflection type PCF interferometer is different for different RH ranges.
- The sensitivities of the sensor with a 40.5 mm length are 3.7, 8.5 and 64 pm/%RH in the RH ranges of 27-60%, 60-80% and 80-96% respectively.
- The sensitivities of the sensor with 17 mm length are 1.7, 3 and 23 pm/%RH in the RH ranges of 27-60%, 60-80% and 80-96% respectively.

- The temperature dependence of the sensor with a length of 40.5 mm is 9.5 pm/^{O}C and for a 17 mm length it is 6.2 pm/^{O}C.
- Since the sensor is made of single material silica it is potentially suitable for monitoring humidity at high temperatures.

III. Relative humidity sensor based on an Agarose infiltrated photonic crystal fiber interferometer

A novel RH sensor based on an Agarose infiltrated PCFI is demonstrated in this thesis. The sensor has the advantages of a very compact size and improved sensitivity compared to the open ended PCFI based RH sensor. The size of the sensor is 1 mm in length and 125 μm in diameter. The sensitivity of the sensor is improved by infiltrating the micro holes of the PCF with a hygroscopic material Agarose. It is shown that a suitable selection of a sub-periodic portion of the interferometer's spectrum allows a reduction in the length of the sensor head making it suitable for monitoring RH in situations when the space available is constrained. An additional advantage of a compact length for the sensor is that it is more mechanically stable in the presence of unwanted vibrations and air flow currents.

A novel fiber optic hybrid device for simultaneously measuring temperature and relative humidity is also experimentally demonstrated in this thesis. A reflection type photonic crystal fiber interferometer infiltrated with humidity sensitive material Agarose acts as the RH sensor and an in-line FBG is used to monitor the temperature. The RH and temperature response of the hybrid device and the cross sensitivity of the device to these measurands are demonstrated in this thesis.

The conclusions from these studies are:

- The infiltration of Agarose amplifies the RH sensitivity of a reflection type PCFI.
- The RH sensor based on an Agarose infiltrated PCFI shows a sensitivity of 0.06 dB/%RH in the range 14-86 %RH and 0.6 dB/%RH in the range 86-98 %RH.
- The sensor's response is repeatable and shows good long term stability.
- The thermal sensitivity of the sensor is 0.066 dB/^{O}C.
- The response time of the sensor is 400 ms which suggests that the sensor can potentially be used as a human breath rate monitor in a clinical situation.
- Fabrication of the sensor shows a good repeatability of the sensor characteristics
- The hybrid sensor has a temperature sensitivity of 9.8 pm/^{O}C and a nonlinear RH sensitivity with an optical power variation of >7 dB for an RH change of 75 %.
- The hybrid sensor is shown to have minimal cross sensitivity.

IV. Relative humidity sensor based on an Agarose coated transmission type photonic crystal fiber interferometer

In this thesis, the structure, fabrication and the working of a transmission type PCFI is demonstrated. The relation between the fringe spacing and the length of the PCF section of the transmission type PCFI is verified experimentally. The transmission type PCFI is coated with Agarose layers of different thickness and it is demonstrated that the RI of the coating experienced by the mode interacting with the coating depends on the thickness of the coating. The effect of coating thickness on the RH response of the AC-PCFI devices is studied and based on this study a highly sensitive RH sensor based on

an AC-PCFI is proposed and demonstrated. The refractive index response of the device is investigated experimentally to enable the selection of a suitable coating thickness. The repeatability of the coating layer formation and the evolution of the coating layers after passing the device though an Agarose solution multiple times are studied in the thesis.

From the studies, it can be concluded that:

- The RH sensitivity of an AC-PCFI depends strongly on the thickness of the Agarose coating due to the fact that the RI of the coating experienced by the mode interacting with the coating is dependent on the thickness of the coating and when this RI comes close to the RI of the silica, the result is a high RH sensitivity of the PCFI device.
- The RH response of the Agarose coated PCFI depends on both bulk RI change and the thickness change of the Agarose coating with respect to RH.
- The high sensitivity RH sensor presented in this thesis gives a large wavelength shift of 56 nm for a RH change of 58% which is the largest reported wavelength shift for an Agarose coated fiber optic RH sensor.
- The sensor shows a linear response for an RH change in the RH ranges of 40-80 % and 80-95 % with a sensitivity of 0.57 nm/%RH and 1.43 nm/%RH respectively.
- The measurement accuracy of the sensor in the RH range 40-80% is ±2% RH, and in the range 80-95%, the accuracy is circa ±1% RH.
- The response time of the sensor is 86 ms for an RH change from 50% to 90%.

- The temperature dependence of the sensor is found to be 0.27 nm/^{O}C, which is relatively small, compared to the RH sensitivity of the sensor.

- The work demonstrated is useful for the selection of an operating point in terms of sensitivity and range of operation for the development of various kinds of sensors for environmental, physical, biological or chemical parameters based on a PCF interferometer, where the coating acts as the transducer for an external parameter.

V. Performance comparison of the RH sensors for suitable derived applications

A performance comparison of the RH sensing devices demonstrated in this thesis is carried out with comparison parameters such as RH range, sensitivity, response time, sensor size, temperature dependence, key advantages and limitations of the sensor.

The main conclusions from the comparison of the sensors are:

- For wavelength interrogation, the sensor based on an Agarose coated photonic crystal fiber interferometer shows the highest sensitivity.

- For insertion loss or power based interrogation, the sensor based on Polyethylene oxide coated fiber bend has the highest sensitivity.

- The response times of all the sensors are less than a second and the temperature dependence is very low.

- The sensor based on an Agarose infiltrated photonic crystal fiber interferometer has the smallest size and good mechanical stability.

The selection of suitable devices for dew sensing and breathing monitoring is carried out based on the performance comparison of these sensors. The use of a reflection type

PCFI without any hygroscopic material is demonstrated for dew sensing and the application of an Agarose infiltrated PCFI with miniature size, good sensitivity and high mechanical stability is demonstrated for breathing monitoring.

The conclusions from these studies are:

- An open ended PCFI is suitable for dew sensing
- The dew sensor shows good dew point measurement accuracy (±0.1 ^{O}C).
- An Agarose infiltrated PCFI is suitable for breathing monitoring.
- The breathing sensor interrogation system can determine the breathing pattern in real time and can also predict the breathing rate and the breathing status during respiration.
- The sensor is suitable for monitoring patients during a magnetic resonance imaging scan where the use of sedatives and anaesthetics necessitates breathing monitoring; electronic sensors are not suitable in such an environment and a visual observation of the patient's respiratory efforts is often difficult.

7.2 Overall conclusions from the research

Several novel fiber optic humidity sensors with many advantages compared to the existing fiber optic RH sensors have been proposed and demonstrated in the Thesis. These sensors are either based on an optical fiber bend or on a photonic crystal fiber interferometer.

Two types of RH sensor based on a fiber bend have been developed: a polyethylene oxide coated fiber bend and an Agarose coated fiber bend. The former gives a high sensitivity for a short RH range while the latter type gives a wide linear response to RH.

Both these sensors offer the advantages of a simple fabrication procedure, low cost and potential disposability. These sensors also show a fast response to RH changes.

Three types of RH sensor based on a photonic crystal fiber interferometer have been developed. They are an open ended reflection type photonic crystal fiber interferometer, Agarose infiltrated PCFI and an Agarose coated PCFI. All these sensors showed good sensitivity and have a reversible, repeatable and fast response to RH variations. The RH sensor based on an open ended reflection type photonic crystal fiber interferometer has the advantage that no hygroscopic materials are required for the operation of the sensor. The developed miniature RH sensor based on an Agarose infiltrated PCFI offers improved sensitivity and operating range in comparison with the open ended PCFI. A novel fiber optic hybrid device for simultaneous measurement of RH and temperature is developed using an Agarose infiltrated PCFI and an in-line FBG. The effect of coating thickness on the sensitivity of an RH sensor based on a transmission type PCFI is experimentally demonstrated and using the results, a high sensitivity RH sensor is developed. A performance comparison of the RH sensors developed is carried out with the comparison parameters: RH range, sensitivity, response time, size, temperature dependence, the need for a hygroscopic material etc. A dew sensor and a breathing monitoring system are developed as a derived application of these RH sensors.

7.3 Future research

This thesis has described experimental investigation of several novel RH sensors based on optical fibers and their derived applications. There remain a number of unanswered research questions and challenges, such as:

A) Reducing the hysteresis of the sensors

Most of the humidity sensors demonstrated in this thesis display a hysteresis in their response. It is important to reduce this hysteresis in order to improve the measurement accuracy of the sensor. A suggested method to reduce the hysteresis effect is annealing the sensor head by heating it after the coating process. Further study on the methods to reduce the hysteris of the sensors will be carried out to improve the measurement accuracy.

B) Sensor packaging and protection

The operation of any fiber optic humidity sensor requires direct interaction with the environment, therefore its performance usually degrades over a period of time due to the different types of contamination, making any sensor unsuitable for long term humidity measurements without special protection. Possible contamination agents are dust particles, organic pollutants and chemical vapors. Thus further study of sensor head contamination in different process environments and the observation of the changes in its response are required in order to get a better understanding of the long term stability of such sensors in field applications.

Some suggested methods to mitigate the effects of sensor contamination are 1) recalibrate the sensor head after a certain period of time and subsequently reuse the sensor head, 2) replace the sensor head as the fabrication of such a sensor is simple and cost effective, 3) protection of the sensor head using anti-contaminant filters; 4) another method to overcome contamination is ultrasonic cleaning and subsequent heating (which will remove the contaminants such as dust particles without damaging the sensor head; it should be noted however that this method is not suitable for sensors with coatings).

For the PCFI sensor without coatings, applying protective coatings on the silica surface could prevent sensor contamination for example: the porous aerogel [1] is permeable to gases but protects the fiber from contamination by dust. Also it is possible to use self-cleaning coatings such as titanium dioxide (TiO_2) [2-3] on PCF which is expected to give good long term stability because TiO_2 coatings act as photo catalysts degrading air and water borne organic pollutants. The use of these sensors in the real field applications also requires secure packaging to avoid any change in the calibration of the sensor due to vibration or other repeated mechanical disturbances.

C) High temperature RH sensing

Conventional glass fiber relative humidity sensors require coatings and thus are always temperature dependent and, furthermore, since the majority of such sensors use polymer materials as coatings, they are not suitable for use in high-temperature applications. One significant advantage of the sensor discussed in chapter 3, an open ended reflection type PCFI, is that the sensor head is made of single material silica, making it suitable for high temperature operation. Also the study of cross sensitivity to temperature reveals that such a humidity sensor is almost temperature independent. This suggests that in addition to low and room temperature applications the open ended PCF interferometer based humidity sensor can also be used in harsh and high-temperature environments to monitor humidity.

High temperature RH monitoring has attracted a lot of interest for several field applications. For example, an autoclave is used for sterilising medical equipment, killing bacteria or other organic substances using saturated steam (absolute humidity = 1.67 Kg/m^3, pressure = 3 bar and temperature = 134 ^{O}C). It is important to monitor the steam quality of an autoclave to avoid the formation of superheated steam which

reduces the sterilisation performance. High temperature RH sensors are required for nuclear reactor steam quality monitoring and monitoring of RH in mines, steam injected ovens, fuel cells, cooking, clothing dryers, etc.

D) Development of portable breathing monitoring device and their clinical trials.

In this thesis a breathing monitoring device based on an Agarose infiltrated PCFI is demonstrated. Making the sensor system portable and the use of the device in a real clinical situation are some important future tasks. Because respiratory depression and upper airway obstruction are frequent complications associated with the use of sedatives and anaesthetics, monitoring the respiratory rate, hypoxemia, and the detection of airway obstruction are important during the administration of these drugs. This is particularly important in an MRI environment because visual observation of the patient's respiratory efforts is often difficult. Also since the anaesthetist cannot accompany the patient, it is essential that the patient is monitored remotely from the neighbouring control room. The strong magnetic fields associated with MRI can interfere with electrical equipment, meaning that conventional electronic sensors cannot be used during the MRI scan. The sensor head demonstrated in the thesis for breathing monitoring does not use any metallic parts; and a remote monitoring is possible with a single connecting fiber which makes this sensor a potential solution for the above applications. The tunable laser source used in the demonstration for in this thesis for interrogation could be replaced with a low cost fixed wavelength laser diode in order to reduce the cost of the system for real-world applications. Adequate packaging of the sensor is also required before using it in a clinical trial to prevent the failure of the sensor when a person coughs or contaminates the device with fluids (saliva, sputum, etc.). Appropriate embedding of the device in a nasal clip or an oxygen mask is required to avoid a possible failure mode such as signal level drift due to the variation of the

distance of the sensor from the nose. By applying an appropriate signal analysis and calibration it is possible to deduce breathing air volume from the sensor response. This could also be one of the future tasks because the value of the breathing volume can be used as an indicator of potential respiratory dysfunction and a patient's pulmonary health status.

Finally as expected, this research has generated several questions and some solutions. Nevertheless, new insights and know-how have been developed which hopefully it will initiate further research on fiber optic based humidity sensors and their applications.

7.4 References

1. L. Xiao, M. Grogan, R. England, W. Wadsworth, and T. Birks, Gas sensing with a sub-micron tapered fiber embedded in hydrophobic aerogel, in *Conference on Lasers and Electro-Optics*. Optical Society of America, (May 2010). http://ieeexplore.ieee.org/stamp/stamp.jsp?arnumber=05500640
2. M. B. Fisher, D. A. Keane, P. Fernández-Ibáñez, J. Colreavy, S. J. Hinder, K. G. McGuigan, S. C. Pillai, Nitrogen and copper doped solar light active TiO_2 photocatalysts for water decontamination, *Applied Catalysis B: Environmental*, 130-131(7), pp. 8-13, (2013).
3. M. Pelaez, N. T. Nolan, S. C. Pillai, M. K. Seery, P. Falaras, A. G. Kontos, P. S. M. Dunlop, J. W. J. Hamilton, J. A. Byrne, K. O'Shea, M. H. Entezari, D. D. Dionysiou, A review on the visible light active titanium dioxide photocatalysts for environmental applications, *Applied Catalysis B: Environmental*, 125, pp. 331-349, (2012).

APPENDIX A. FIBER-OPTIC SENSING TECHNIQUES FOR HUMIDITY DETECTION

Table A.1. Overview of the various fiber-optic sensing techniques for humidity detection (some data in this table are taken from ref. [7])

Refer-ence	Year	Authors	Sensing method	Sensing material	Range (%RH)	Respon se time
Direct spectroscopic						
[14]	1988	Zhou et al.	Direct in-line absorption	Etched borosilicate optical fiber segment doped with $CoCl_2$	20-50	<5 min
[20]	1988	Posch and Wolfbeis	Fluorescence quenching	Perylene dyes	0-100	-
[21]	1995	Raichur and Pederson	Fluorescence quenching	Aluminium/morin metal ion–organic complex doped polyvinyl pyrrolidone membrane	0-80	-
[16]	1997	Brook et al.	Absorption	Crystal violet doped Nafion film	40-82	
[17]	1998	Otsuki et al.	Direct in-line absorption (open air-gap configuration)	Rhodamine B doped hydroxypropyl cellulose (HPC) film	0-95	~2 min
[22]	2001	Glenn et al.	Fluorescence lifetime	Lithium-treated Nafion membrane	-	-
[15]	2004	Tao et al.	Direct in-line absorption	Porous sol–gel fiber segment doped with $CoCl_2$	2-10	
[23]	2006	Bedoya et al.	Fluorescence lifetime	Ruthenium-based complex doped Poly(tetrafluoroethylene) membrane	4-100	~2 min
[18]	2012	Mohd Noor et al.	Monitoring water vapor line absorption	Hollow core-photonic bandgap fiber	0-90	~118 s
[19]	2012	Mohd Noor et al.	wavelength scanning around the water vapor absorption peak	Air-guided photonic crystal fiber	0-90	-
Evanescent wave						
[24]	1985	Russell and Fletcher	Absorption measurement using straight and U-bent fiber	$CoCl_2$ doped gelatine film	50-80	<1 min
[25]	1988	Ogawa et al.	Attenuation measurement using Optical time-domain reflectometer (OTDR) technique	Porous SiO_2 optical fiber cladding	25-95	-
[26]	1995	Michie et al	OTDR Reflectometry	Chemically sensitive water swellable polymers	-	-

[27]	1995	Kharaz and Jones	Absorption measurement using OTDR technique	$CoCl_2$ doped gelatine film	20-80	1 s
[28]	1997	Bownass et al	Insertion loss measurement of a polished half-block single-mode fiber	Polyethylene oxide (PEO) overlay	-	<2 hr
[29]	1998	Bownass et al	Insertion loss measurement of a bent fiber	Gelatine/PEO film	-	-
[30]	1998	Otsuki et al.	Absorption measurement using U-bent fiber	Rhodamine B doped HPC film	0-95	~2 min
[31]	2000	Kharaz et al.	Absorption measurement using U-bent fiber	$CoCl_2$ doped hydroxy ethyl cellulose (HEC) and gelatine films	H:30-96 G:40-80	
[32]	2000	Bariain et al.	Attenuation measurement using tapered fiber	Agarose gel	30-80	<1 min
[33]	2001	Gupta and Ratnanjali	Absorption measurement using U-bent fiber	Phenol red doped polymethylmethacrylate (PMMA) film	20-80	-
[34]	2002	Jindal et al.	Absorption measurement using straight and U-bent fiber	$CoCl_2$ doped polyvinyl alcohol (PVA) film	S: >78	
[35]	2003	Muto et al.	Attenuation measurement using PMMA plastic optical fiber	HEC/Polyvinylidene fluoride (PVDF) film	20-80	<5 s
[36]	2003	Arregui et al.	Attenuation measurement	Hydrogels-Agarose gel, poly- hydroxyethyl methacrylate, poly- N-vinyl pyrrolidinone, poly-acrylamide	Agarose : 10-100	~90 s
[37]	2004	Gaston et al.	Attenuation measurement using side-polished fiber	PVA film	50-90	1 min
[49]	2004	Alvarez-Herrero et al.	Wavelength resonance shift using side-polished fiber	TiO_2 film	0-80	-
[38]	2004	Xu et al.	Attenuation measurement	Porous sol–gel cladding	3-90	<1 min
[39]	2006	Corres et al.	Attenuation measurement using tapered fiber	Poly(Diallylmethilammonium chloride) PDDA/Poly R-478 nanostructured sensing overlay using Electrostatic self-assembly (ESA) technique	75-100	-
[40]	2007	Mathew et	Attenuation	Agarose/Chitosan film	20-95	2 s

		al.	measurement using cladding removed plastic cladded silica fiber			
[41]	2008	Acikgoz et al	Attenuation measurement of a polished plastic optical fiber	Polyethylene glycol	10-95	-
[42]	2008	Zhang et al.	Attenuation measurement using tapered fiber	Gelatine film	9-94	70 ms
[43]	2008	Vijayan et al.	Measurement of intensity of a PMMA fiber bend	Co nanoparticles dispersed polyaniline	20-95	8 s
[50]	2010	Hernaez et al.	Measurement of electromagnetic resonance absorption peak of an indium tin oxide (ITO) coated etched fiber	Agarose	20-80	>1 s
[51]	2010	Zamarreno et al.	Measurement of resonance wavelength of an ITO coated optical fiber	Poly(allylamine hydrochloride) and poly (acrylic acid) using layer-by-layer (LbL) deposition technique	20-90	-
[44]	2010	Akita et al	Intensity measurement of a fiber hetero structure	Poly-glutamic acid/poly-lysine using LbL technique	50-92.9	400 ms
[45]	2011	Corres et al.	Attenuation measurement of a fiber hetero structure	Poly(Vynilidene fluoride) nanowebs using electro spinning technique	50-70	100 ms
[52]	2011	Sanchez et al.	Measurement of lossy mode resonance of a ITO or In_2O_3 coated fiber	polyallylamin hydrochloride / poly-acrylic acid polymeric coatings	20-80	-
[46]	2011	Zhao et al.	Attenuation measurement of a bend multi-mode fiber	Methylene blue doped sol-gel film	1.1-70	20s-3min
[47]	2012	Li et al.	Intensity measurement of a multimode fiber taper via an fiber Bragg grating (FBG) reflection	Polyvinyl alcohol	30-95	~2 s
[48]	2012	Aneesh et al.	Intensity measurement of a multimode cladding removed plastic cladded silica (PCS) fiber	TiO_2 doped Sol gel film	24-95	10 ms
[53]	2012	Rivero et al.	Wavelength measurement of lossy-mode resonance and	Ag nanoparticles doped Poly (allylamine hydrochloride)-poly	25-70	476 ms

			localized surface plasmon resonance of a PCS fiber	(acrylic acid) layer formed by LbL technique		
In-fiber grating						
[54]	2001	Giaccari et al.	Strain-induced Bragg wavelength measurement	Polyimide	10-90	-
[55]	2002	Kronenberg et al.	Strain-induced Bragg wavelength measurement	Polyimide	10-90	-
[62]	2002	Luo et al.	Long period grating (LPG) resonant band wavelength measurement	Carboxy methyl cellulose	0-95	-
[63]	2005	Tan et al.	LPG resonant band intensity measurement	Gelatine	90-99	-
[56]	2005	Yeo et al	Strain-induced Bragg wavelength measurement	Polyimide	22-97	25 min
[57]	2005	Yeo et al	Strain-induced Bragg wavelength measurement	Polyimide	23-97	18 min
[64]	2006	Konstantaki et al.	LPG resonant band intensity and wavelength measurement	$CoCl_2$ doped PEO film	I:70-80 W:40-80	<1 s
[58]	2007	Huang et al.	Intensity measurement using a coarse wavelength division multiplexing linear edge filter.	Polyimide	11-98	5 s
[65]	2008	Venugopalan et al.	LPG resonant band wavelength measurement	Polyvinyl alcohol	33-97	80 s
[66]	2008	Venugopalan et al.	LPG resonant band wavelength measurement	Polyvinyl alcohol	33-97	50 s
[67]	2009	Viegas et al.	LPG resonant band wavelength measurement	silica nanospheres film	20-80	100-200 ms
[68]	2009	Viegas et al.	LPG resonant band wavelength measurement	Silica nano spheres using ESA technique	20-80	-
[59]	2010	Zhang et al.	Bragg wavelength measurement	Bragg gratings recorded in silica and polymer fiber	50-95	~30 min
[69]	2011	Viegas et al.	Intensity measurement of an LPG in-line with FBG	Silica nanospheres film	20-80	30 ms
[70]	2011	Fu et al.	Resonant band wavelength measurement of a air	Calcium chloride film	55-95	-

			gap LPG			
[60]	2012	Correia et al.	Bragg wavelength measurement	Di-ureasil (formed of polyether chains covalently linked to a siliceous inorganic skeleton by urea bridges).	5-95	~8 min
[61]	2012	David et al.	Bragg wavelength measurement of an etched FBG	Pyralin	15-95	~3 s
Interferometric						
[71]	1989	Mitschke	Intensity measurement using Fabry–Perot configuration	SiO_2–TiO_2–SiO_2 cavity	0-80	1 min
[72]	1999	Arregui et al.	Intensity measurement using Fabry–Perot configuration	SiO_2–[Au:PDDA+ /poly (sodium 4-styrene-sulfonate) (PSS)-]-air cavity using ionic self-assembly monolayer (ISAM) technique	11-100	1.5 s
[79]	1999	Kronenberg et al.	Tandem Michelson interferometer configuration	Polyurethane urea - PEO/poly(propylene oxide) Hydrogel	-	-
[73]	2001	Yu et al.	Intensity measurement using Fabry–Perot configuration	SiO_2–[PDDA+ /Poly S119-]-air cavity using ISAM technique	0-97	3 s
[74]	2002	Arregui et al.	Intensity measurement using Fabry–Perot configuration	Poly R-478- PDDA using electrostatic self-assembled monolayer (ESAM) technique	11-97	<1.5 s
[75]	2008	Corres et al.	Intensity measurement of a Fabry–Perot configuration	Nanostructured Coatings of SiO_2 Nanoparticles	40-98	150 ms
[76]	2011	Consales et al.	Intensity measurement using Fabry–Perot configuration	micro-structured SnO_2 overlay using Electrostatic Spray Pyrolysis technique	2-40	-
[81]	2011	Wu et al.	Wavelength measurement of a fiber hetero-core structure	PEO film	40-95	-
[82]	2011	Gu et al.	Wavelength measurement of a FBG incorporated thin-core fiber modal interferometer	Poly (N-ethyl-4-vinylpyridinium chloride) (P4VP·HCl) and poly (vinylsulfonic acid, sodium salt) (PVS) using an LbL electrostatic self-assembly technique.	20-90	2 s
[83]	2011	Wang et al.	Wavelength	Polyacrylamide micro	5-71	120 ms

			measurement of fiber micro ring	fiber		
[84]	2011	Wu et al.	Wavelength measurement of fiber micro ring	Silica/polymer microfiber knot resonators	17-95	< 500 ms
[77]	2012	Chen et al.	Wavelength measurement using Fabry–Perot configuration	Chitosan film	20-95	380 ms
[78]	2012	Yao et al.	Wavelength and intensity (response time) measurement using Fabry–Perot configuration	Nanocomposite polyacrylamide	38-98	250 ms
[85]	2012	Chen et al.	Wavelength measurement of a Sagnac interferometer	Chitosan	20-95	-
[80]	2012	Wong et al.	Wavelength measurement of a Michelson interferometer	Polyvinyl alcohol	30-90	300 ms

APPENDIX B.

EQUIPMENT AND ACCESSORIES

This appendix covers the details of main instruments and accessories used in the experimental work presented in this thesis. Important specifications and operational characteristics of the fiber fusion splicer, broadband source, tunable laser source, optical spectrum analyzer, and optical power meter are highlighted in this section. A block diagram of the LabVIEW based breath analysis application programme is also shown.

Fusion Splicer

For splicing the fibers together, Sumitomo Type 36 Fusion Splicer is used, which is a portable, self contained fully automatic instrument for creating low-loss optical fiber splices. The splicer can handle different fiber types with a fiber cladding diameter of 125 microns. In the automatic mode of operation a precision CCD camera examines the fiber from the X and Y view and precisely aligns the fibers, before performing the arc splicing. After splicing, high resolution direct core monitoring image processing software incorporated into the splicer calculates the estimated splice loss. The manual mode option of the splicer is used for the fusion splicing of photonic crystal fiber (PCF) and SMF to fabricate the PCF interferometers. The X and Y CCD cameras can be used to align the fiber precisely before applying the electric arc for fusion splicing. The splicer allows to set required values of arc power, arc duration, prefusion time etc. in the manual mode.

Broadband Source

The broadband source used to interrogate the sensors is a super luminescent diode (SLD), SLD-1005 (SLD6593) from Covega Corporation. The SLD 1005 is a 1550 nm high power, broadband SLD with near Gaussian spectral profile and low ripple. It is housed in a standard 14-pin butterfly package with integrated thermoelectric cooler and thermistor. The output is coupled via isolator into a single mode fiber with an FC/APC connector. SLD-1005 was driven by a laser diode combi controller ITC-510 from Throlabs. The key specifications of the SLD are,

Operating current (I_{OP}): 600 mA; Operating temperature: 25 ^{O}C; Center wavelength (λ_C): 1544.5 nm; ASE Power @ $I_{OP:}$ 20.8 mW; Optical Bandwidth @ $I_{OP:}$ 54.5 nm

Tunable Laser

The laser source used to interrogate the sensors is a tunable external cavity laser from Anritsu, model Tunics plus CL/WB. The main specifications of the laser are listed below:

Wavelength range, with 0 dBm power output→ 1490-1640 nm and with 8 dBm power output→ 1540-1610 nm; Output Power range: 0.2 mW-10 mW; Wavelength setting resolution: 0.00l nm; Wavelength accuracy: ±0.04nm; Tuning speed: 100 nm/s; Power stability: ±0.01dB; Side mode suppression ratio: >45 dB; Optical interface: FC/APC connector; Output fiber: SMF 28.

Optical Spectrum Analyzer

For the experiments conducted in this thesis, the spectra are obtained using Advantest Q8384 optical spectrum analyzer (OSA). The key specifications of the OSA are given below:

Wavelength measurement range: 600-1700 nm, Highest wavelength resolution: 10 pm, Highest wavelength accuracy: ±20 pm, Power measurement range: -87 to +23 dBm, Power accuracy: ±0.4 dB (1550 nm), Optical input connector: FC/PC, Internal adapting fiber: 9.5/125 μm SM fiber

Optical Power Meter

The power meter is used to measure power in the experiments is PXIT2000-306, a dual channel fiber optic power meter from PX Instrument Technology, The PXIT2000-306 is a high performance dual channel power meter compatible with the PXI format. An InGaAs photo detector is used to convert optical signal in to electrical. The key specifications of the power meter are:

Wavelength range: 900-1700 nm, Minimum measurable power: -70 dBm, Maximum input power: +10 dBm, Power resolution: 0.01dB, Measurement speed: >5000 Measurements per second @ > -30 dBm, Fiber types supported: multimode and single mode fiber, Connector interface: FC/APC.

Breathing analysis application programme

The breathing analysis application programme (BAAP) is developed using the LabVIEW (Laboratory Virtual Instrument Engineering Workbench) 8.0. The drivers provided by the National Instruments for the optical power meter (PXIT2000-306) are used to initialise the device and acquire the power data from the device in the main programme. Required signal processing of the data is carried out in the main programme using the suitable tools of the software. The block diagram of the breathing analysis application programme developed is shown in Fig B.1.

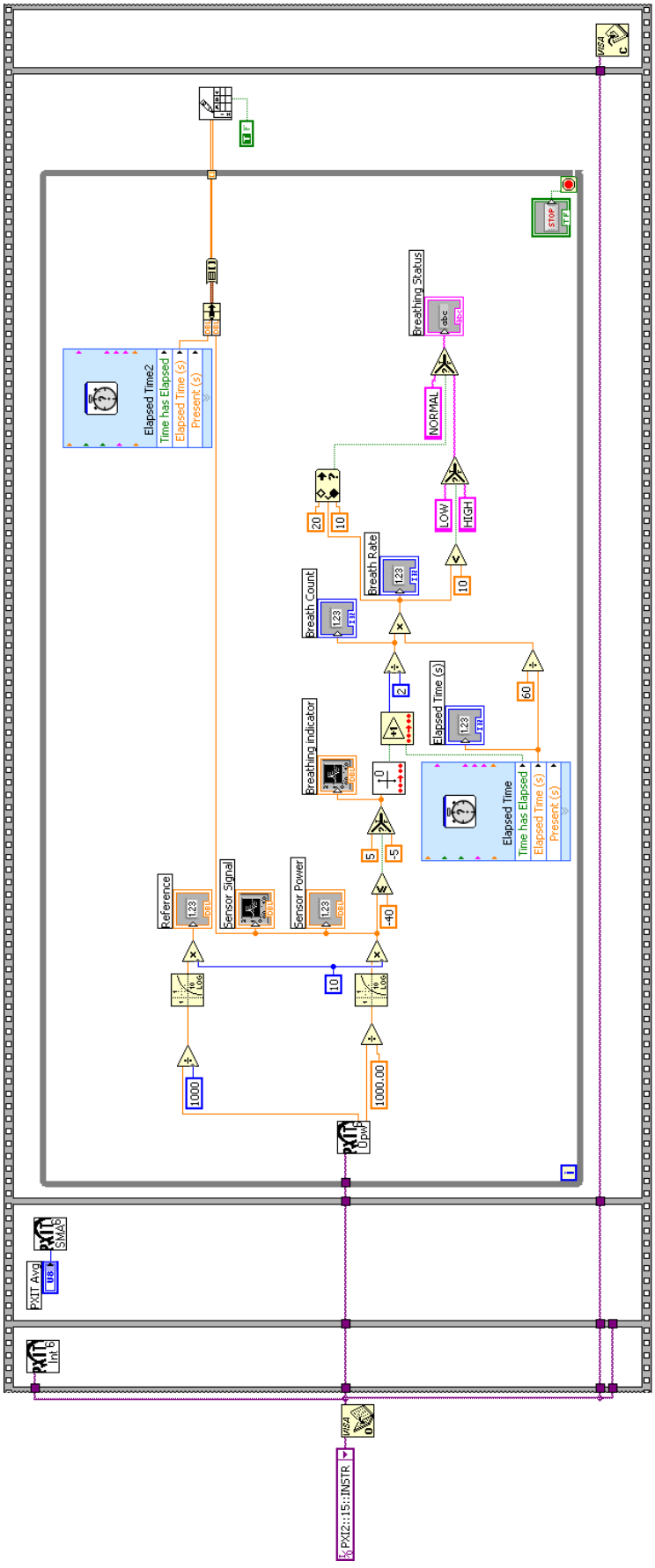

Fig B.1. Block diagram of the LabVIEW software based breathing analysis application programme.